

REGIONAL AND HISTORICAL GEOCRYOLOGY

DOI: 10.21782/EC2541-9994-2020-2(3-13)

SYNGENETIC ICE WEDGES AND AGE OF SLOPE YEDOMA DEPOSITS
IN THE FOOTHILLS OF THE KULAR RIDGE

Yu.K. Vasil'chuk, A.C. Vasil'chuk

*Lomonosov Moscow State University, Faculties of Geography and Geology,
1, Leninskie Gory, Moscow, 119991, Russia; vasilch_geo@mail.ru
Tyumen State University, 6, Volodarskogo str., Tyumen, 625003, Russia*

The structure and composition of Late Pleistocene ice wedges in the ice complex outcropping onto the gently sloping Kular ridge in the western Yana-Indigirka Lowland are considered. Ice wedges are dated 47–42 and 37–32 kyr BP. Over this time, relatively high temperatures of the growing season were recorded twice. Their rise appeared to be sufficient for the growth of trees, while a relatively warm summer season activated slope processes and accumulation of slope yedoma deposits.

Ice wedges, Late Pleistocene, permafrost, yedoma, radiocarbon dating, Kular ridge, Northern Yakutia

INTRODUCTION

This study sets out to investigate peculiar structural features of yedoma sequences containing ice wedges which are widespread in the Kular ridge area, along with radiocarbon dating of their sediments. In the Russian literature, the term “yedoma” has several meanings: in the geomorphic sense (“yedoma surface”) in the stratigraphic sense (yedoma suite); and in the geocryological sense, as a special type of frozen syngenetic ice-rich sediments penetrated by ice wedges [Sher, 1997]. The general concept of “yedoma” adopted in the foreign literature, refers specifically to ice-rich deposits with syngenetic ice wedges [Schirmer et al., 2013]. The term “yedoma” used herewith reflects the definition given by Yu. Vasil'chuk, as follows: “yedoma” is syngenetic extremely ice-rich (ice content: >50–90 %) frozen earth material commonly enriched in organic material (organic matter content: >1–2 %) and represented by clayey silts, silty sands, and fine sands of Late Pleistocene age hosting large syngenetic ice wedges (15–20 m and more in height, 1.0–3.5 m in width), often with multi-layered structure. In the intermountain basins and on slopes, yedoma sequences may be saturated with silty medium gravel and rubble material, while yedoma sequences in valleys and river deltas may contain gravel and pebbles [Vasil'chuk, 1992]. The age of yedoma sequences varies from 11.7 to 50 calibrated (cal) thousand years and older. One of the specific characteristics of these deposits is the pungent odor (“smell of horse stables”) given off by the decomposing organic matter.

ENVIRONMENTAL CONDITIONS
IN THE STUDY AREA

Geographical location

The studied cross-section of the yedoma ice-wedge polygon system is located in the foothills of the Kular ridge near the abandoned rural settlement of Kular (70°38'02" N, 134°19'57" E), on the south-facing slope of the Burguat River valley, which is part of the Omoloy River basin (Fig. 1). In terms of tectonic setting, the Kular gold-bearing region comprising the study area is subsumed into the continental zone of the rift system [Konstantinov et al., 2013]. Hence, rifting is implicated in to the slope processes intensity in this region.

Climate, terrain and surface waters

According to climate zoning pattern discussed in [Alisov, 1956], the study region is located in the on-shore area of the Arctic belt. The key temperature/precipitation data reported from the nearest Kazach'e weather station include: the mean January air temperature (t_j) over the past 20–30 years (from –36 to –39 °C), the mean July temperature (from +4 to +11 °C), and the mean annual air temperature (MAAT) (around –14 °C); the annual precipitation amounting to 200–250 mm/year and unevenly distributed between the winter (ca. 50 mm) and summer (from 50 to 200 mm) seasons in [http://ru. Climate-Data.org]. Note that the data obtained by the authors from the study of elementary ice wedges which formed during the last 100 years on the floodplain served as the basis for the paleotemperature in-

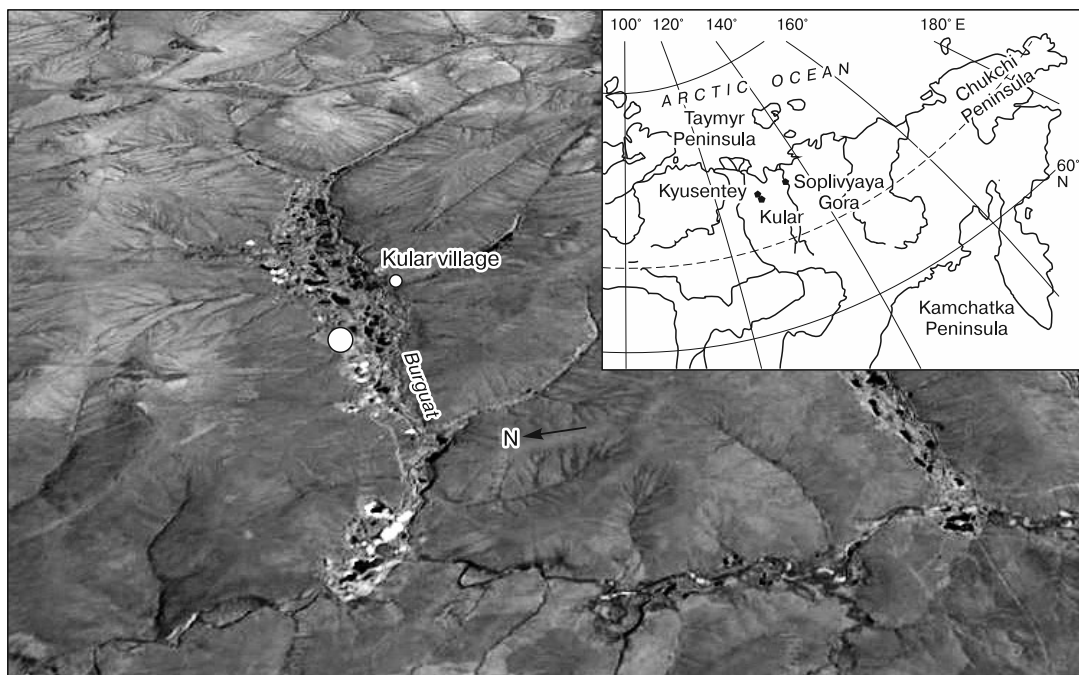


Fig. 1. Map showing location of the yedoma sequence cross-section near Kular village.

terpretation of the stable isotope composition of ice wedges [Vasil'chuk, 1991]; it is therefore critical to additionally provide the available data from the Kazach'e weather station for earlier period spanning from 1930 to 1966, where t_j varied from -39 to -37.4 °C [Reference Books, 1966].

Accumulation landforms are represented mainly by surfaces of slope accumulation encircling watersheds and superimposed on river terraces. The Burguat River and Kuchuguy-Kuegyulyur River valleys, whose width reaches 1.5 km in man-made extensions, are characterized by a box-shaped asymmetric cross-section exposing steep slopes, which becomes V-shaped in the upper reaches. A detailed study of the region's terrain by Gravis [1969] allowed to distinguish three major elements in the asymmetric valleys: 1) the bottom, which includes the riverbed, floodplain and (locally) one above-floodplain terrace; 2) terrace-ridge, which is a flat area, most often located at the foot of south- or west-facing slope; 3) the valley slopes composed of bedrock, overlain by thin layers of loose deposits. In the upper reaches of small rivers, where neither the floodplain nor permanent riverbed are developed, the slopes' asymmetry is not pronounced. Lower down the river, they gradually pass into shallow, but fairly wide gullies with matted walls and bottom. A narrow riverbed is characterized by developing small meandering bends which favor the formation of disparate small segments of the floodplain. These gradually coalesce to form a single terrace reaching 100 m and more in width. Its surface

is generally swampy and is occasionally interspersed with oxbow landforms like small ox bow lakes. This type of terrain has been studied fairly thoroughly in the vicinity of Kular village. The terrace-ridges are often cross-cut by tributaries of the main river. Extensive, flat alluvial fans which commonly develop on the floodplain (opposite to the mouths of the tributaries) completely block the riverbed, thereby diverting the main river towards the opposite slope.

The beginning of the Late Pleistocene saw a decrease in the local erosion basis (Yana and Omoloy Rivers), against the backdrop of general uplift of the Kular arch, which largely governed the ongoing relief-forming processes [Soloviev *et al.*, 2003]. This indicates that slope processes had played a significant role in sediment distribution and accumulation.

Geocryological conditions

According to the data obtained at the Russian Research Institute for Hydrogeology and Engineering Geology, permafrost thickness in the Kular village area varies from 90 m (Burguat River valley) to ~300 m (summit surfaces). The mean annual temperature of permafrost averages between -6 and -8 °C, with the frost cracking, cryogenic weathering, as well as curum formation and thermokarst being widespread phenomena. Deposits containing ice wedges, are encountered both on slopes (more frequently, in the cross-sections of terrace-ridges) and in river valleys. Slope deposits are represented by brownish-grey silty sands and clayey silts with inclusions of rubble

material, slate, which are often iron-rich, and abound in organic remains. The sediment thickness in the middle and lower parts of hillslopes can reach 10–15 m or more.

HISTORY OF RESEARCH

The cryostructure of deposits in the Kular ridge has been studied fairly thoroughly from cross-sections of mine shafts, boreholes, pits and open-cut mines over recent decades [Kuznetsova, 1967; Gravis,

1969; Ventskevich et al., 1969; Konishchev, 1981; Vasil'chuk, 1990; Kanevskiy, 2004]. The area provides intriguing features, unequaled elsewhere in permafrost areas. The structure of ice wedges and pseudomorphs in the pebble-blocky-rubble horizon is studied in detail, which in itself is an infrequent phenomenon. Thus, Kuznetsova [1967] described the structure of sediments containing thick ice wedges exposed in the inclined ca. 50 m long mine shaft in the Burguat River valley. Results of the study of ice wedges occurring in the layer of pebble admixed with rubble material in the Kular mines revealed [Ventskevich et al., 1969] that ice wedges often dissect the gold-bearing deposits to the bedrock (Fig. 2, *a, b*). While they may not reach the bedrock base (Fig. 2, *b*), most of them have an unusual configuration.

Gravis [1969], who studied the cryolithological structure of the Kular foothills in mines next to numerous pits dug during winter for four years, revealed evidences of ice wedge formation in slopes, and signs suggesting solifluction origin for the sediments. He found that, depending on the rate of the soil mass movement, elementary wedges can be arranged either in the form of a fan (high displacement rate) (Fig. 3, *a*) or become asymmetric, without being separated (low displacement rate) (Fig. 3, *b*).

In the Kyusenty River valley, 40 km northeast from Kular village, Gravis described five layers (tiers) of ice wedges (Fig. 4). At this, their number varied even within a single slope, which strongly reflects the slope-specific variability of sediment accumulation conditions. At the slopes base, Gravis identified the riverbed and floodplain alluvium facies. Analysis of the cross-sections allowed him to infer that the sediments accumulated the most thickly in the ancient Kyusenty River valley in parallel to accumulation of

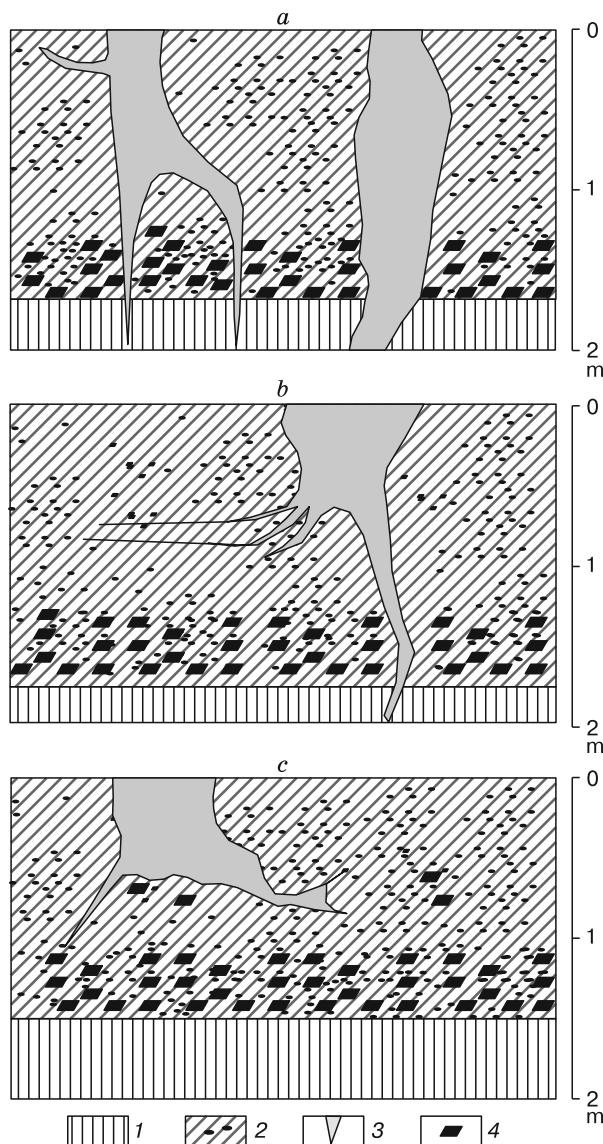


Fig. 2. Field sketches of the shape of "tails" (tips) of ice wedges observed in a mine shaft in the Kular yedoma sequence, intersected by the cross-section across the strike (after: [Ventskevich et al., 1969], simplified).

1 – bedrock eluvium; 2 – pebbles with silty sands and clayey silt infill; 3 – ice wedge; 4 – rubble material.

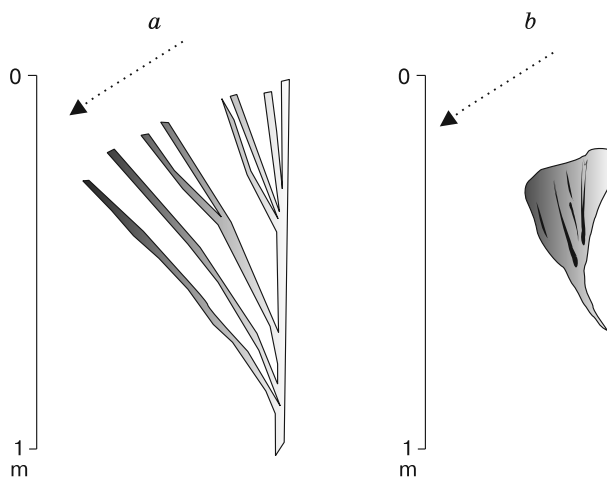


Fig. 3. Ice wedges formed in the slope deposits (after: [Gravis, 1969], amended):

a – fan-shaped, *b* – asymmetric. The arrow indicates the direction of the material displacement.

riverbed and floodplain deposits, and of the lowermost part of silty sands and clayey silts. After the incision had taken place, further sedimentation was dominantly controlled by the steep hillslopes.

The cryolithological structure of deluvial-solifluction slope deposits of the Burguat River valley was studied by Kanevskiy [2004]. A total of about 40 boreholes were drilled into the slope (Fig. 5, A). At least two generations of ice wedges were identified in this sequence. The thickness of slope deposits var-

ies from 3 to 20 m. A major part of the slope sediment sequence is composed by grey silty sands with micro- and inner-thinly-lenticular cryostructure, with their layers locally growing extremely ice-rich (thickness: 0.1–3 m) with ataxitic(suspended)/reticulate cryostructure, encountered at different depths (Fig. 5, B, C). Their total moisture content is 150–200 %. According to Kanevskiy, these deposits are generally extremely ice-rich, have relatively low thickness, and lack a distinct rhythmicity in their

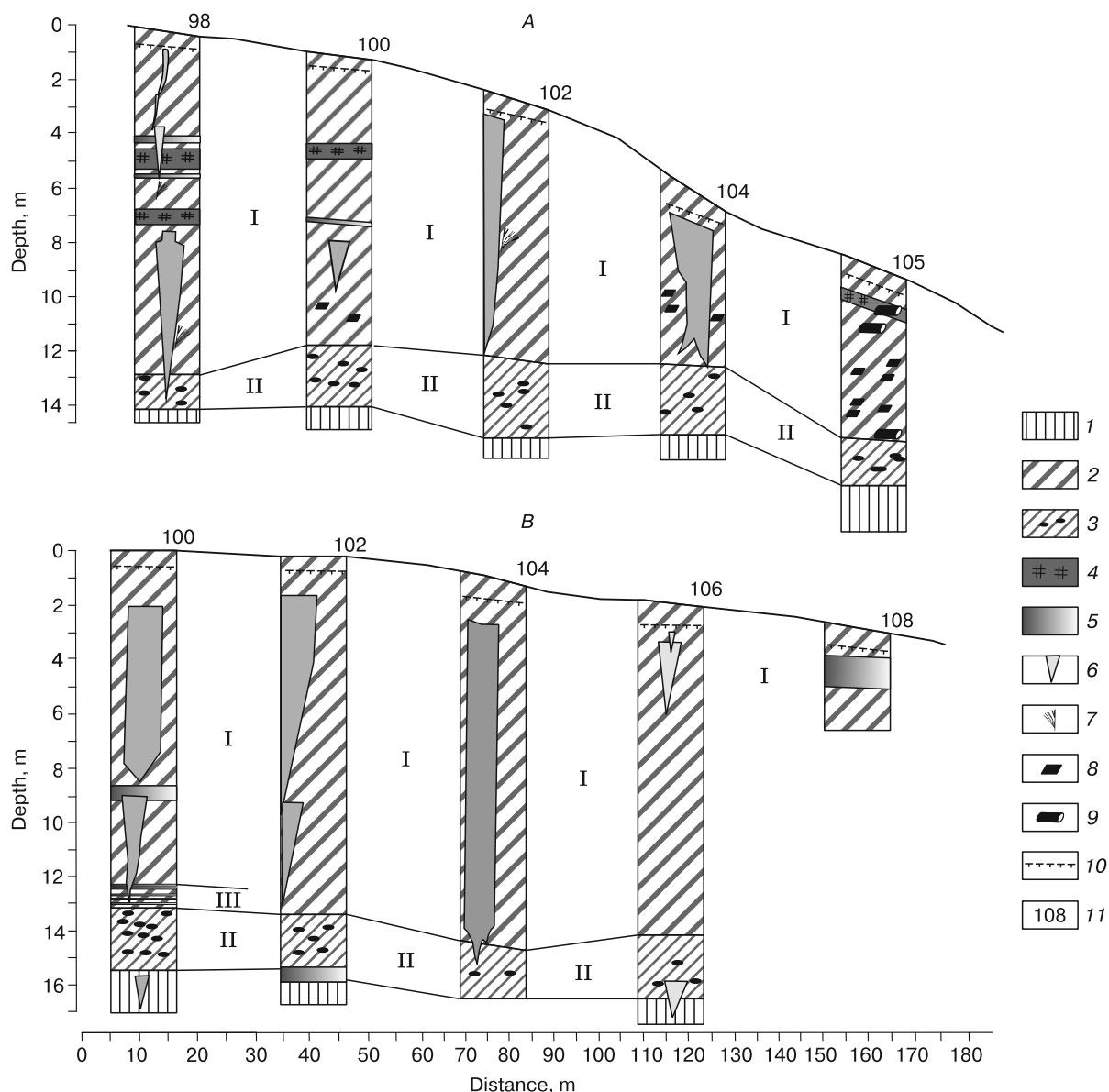


Fig. 4. Cryostructure of slope deposits in the Kyusentey River valley (40 km NE from Kular village) (after: [Gravis, 1969], simplified).

A – cross-sections of pits along line 138; B – cross-sections of pits along line 157. I – deluvial solifluction sediments; II – riverbed alluvium; III – floodplain alluvium; 1 – bedrock eluvium; 2 – silty clay, frozen, with fine-lens-like, cross-bedded and horizontally-layered cryostructure; 3 – pebble-bed with silty sands and clayey silts, frozen, with dominantly crust-like cryostructure; 4 – peat, frozen with discontinuous layered reticulate cryostructure; 5 – ice-lens; 6 – ice wedge; 7 – fan-shaped ice wedges; 8 – rubble material; 9 – buried branches of large shrubs; 10 – lower limit of the active layer; 11 – numbering of pits.

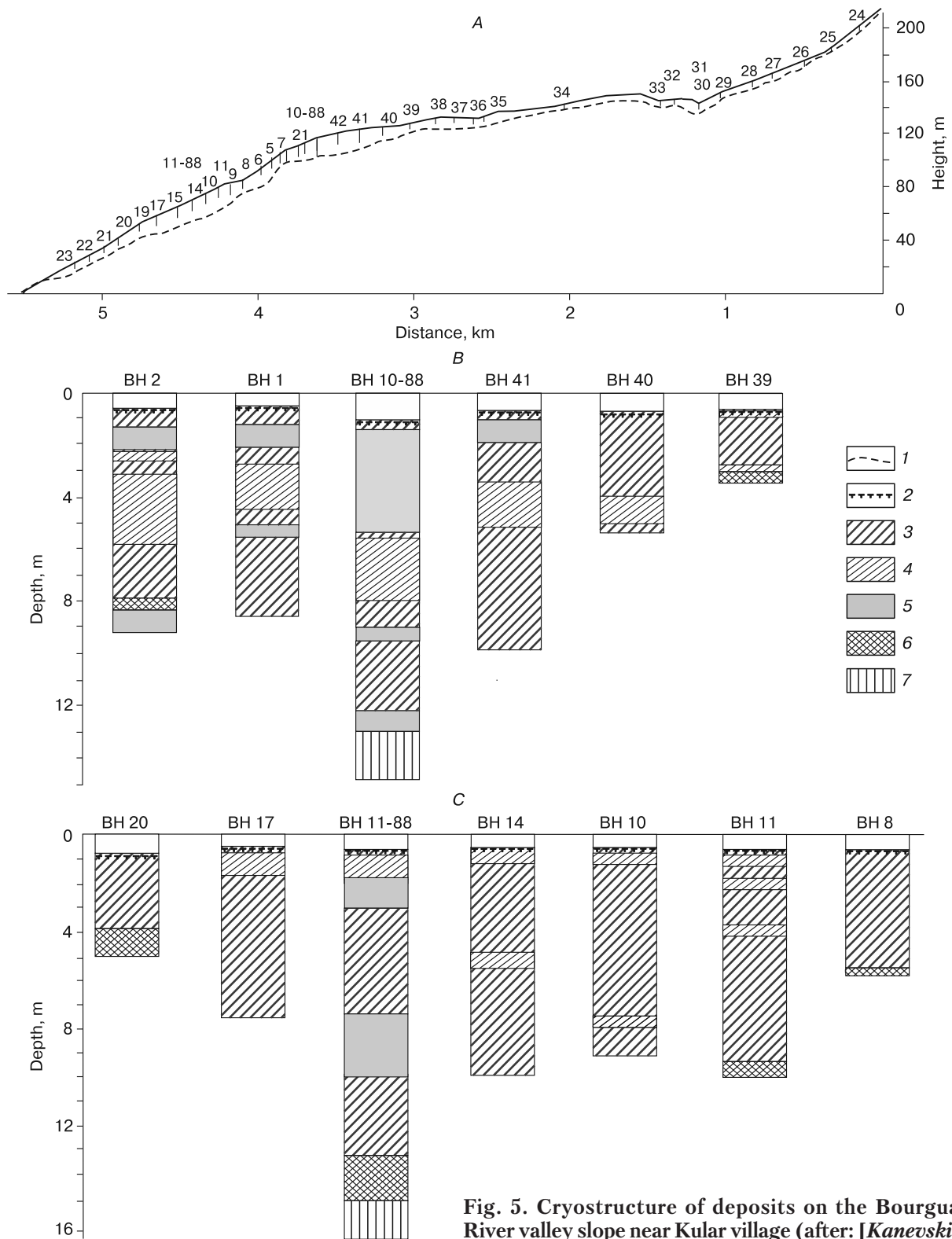


Fig. 5. Cryostructure of deposits on the Bourguat River valley slope near Kular village (after: [Kanevskiy, 2004], simplified).

A – boreholes location plan; B – borehole sections in the mid-slope part; C – cross-sections of boreholes in the lower part of the slope. 1 – slope base deposits; 2 – lower limit of the active layer; 3 – silty sand, grey, frozen with micro- and thin ice lenses, lenticular cryostructure; 4 – silty sand, grey, frozen with ataxitic and reticulate cryostructure; 5 – ice wedge; 6 – medium to fine gravel; 7 – bedrock eluvium.

structure. This author described subhorizontally occurring syngenetic ice wedges oriented perpendicular to the slope dip [Kanevskiy, 2003]. Kanevskiy [2004] showed that differentiation by composition between Ice Complex deposits and slope deluvial solifluction deposits is almost indiscernible in the Kular area. Ice Complex deposits basically make up terrace-ridges and watershed slopes, while terrace-ridges tend to develop in their pediment areas (deluvial solifluction deposits). Ice wedges inherent in this area are accentuated by their multilayer occurrence and diversity of shapes, while yedoma sequences display a complex structure.

RESEARCH RESULTS OBTAINED FOR ICE WEDGES AND THE SURROUNDING KULAR YEDOMA SEDIMENTS

The structure and composition of yedoma sequence

In the outcrop fragment studied in detail by the authors on the gentle sloping, south-facing Burguat River valley slope (0.5 km west of the mouth of the Emis Creek), the ice wedge-bearing sequence occurs in the form of a terrace-ridge stretching for more than 1 km along the slope, with surface slope angle of 4–5°.

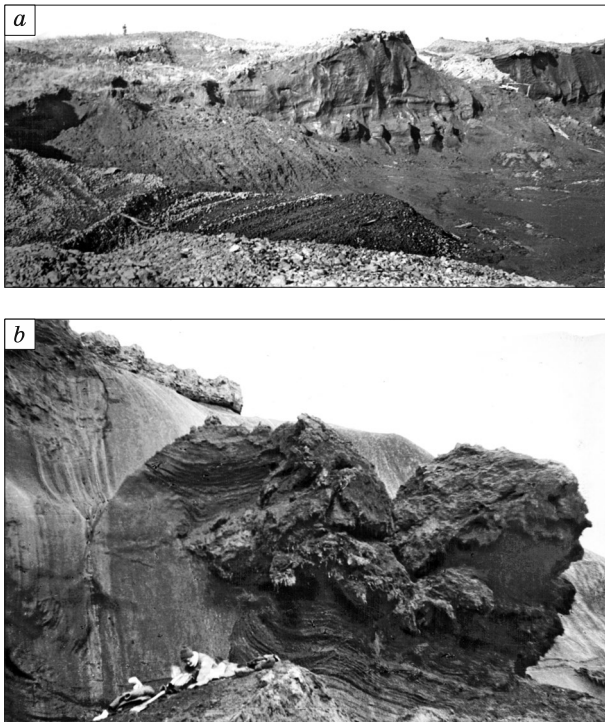


Fig. 6. Ice wedges in the yedoma exposure near Kular village.

a – general view of the open-cut mine (ice wedges are shown in the background against a vertical wall); *b* – vertically-banded syngenetic ice wedge (on the left) and a thick peat layer. Photograph by Yu.K. Vasil'chuk.

Absolute elevation marks of yedoma vary from 95 m (near the stream) to 110–120 m (in the upper part of the slope), and from 105 to 140 m (in the topmost layer).

The yedoma sequence in the described outcrop fragment averages ca. 22 m in thickness, which may reach 28 m. The structure of one of the most representative terrace-ridge portion was studied by the authors in abandoned open-cut mine within a mid-slope segment (Fig. 6, *a*, 7). The bedrock exposed at the base of the terrace-ridge, is overlain by up to 1 m thick gravelly eluvium bed. The layer of fine black sand (thickness: from 0.5 to 2–3 m) atop it is cross-stratified, with inclusions of gravel and subrounded pebbles. By all appearances, the sand is of alluvial origin and is attributed to the riverbed sediment facies. At the interface between sands and overlying grey silty sands, the authors observed a layer of bluish-grey segregated ice (up to 1.5 m thick) with inclusions of minute pebbles. The yedoma sequence is composed of grey silty sand and clayey silt with thick lenses of peat and discrete interlayers of organic material. Layers of peat are usually contorted and disrupted, which is typical of solifluction deposits. The fuzzy, intermittent ice inclusions and asymmetric ice wedges identified in the section, according to Gravis [1969], are also indicative of solifluction origin of the sequence.

Both thick syngenetic ice wedges and multi-tier ice wedge identified in the section, are abundant across the entire sequence (Fig. 6). The heads of multi-tier ice wedges occur at different depths (0.7–1.0, 4–5, 8.5–10, 15–17 m), and at least three or four tiers of ice wedges are observed. Ice wedges reach 3.5 m in width and exhibit brownish-grey ice, with admixture of peat and silty sands. The distance between ice wedges is 13–15 m. The “tails” (tips) of wedges occur at different depths, and either cross-cut the eluvium, or occur at a height of 3–5 m from the yedoma sequence base. Ice wedges are contorted (deviation of the wedges' axes from vertical position is usually 1.0–1.2 m). Ice wedges oriented along and across the slope tend to differentiate.

Ice wedges located along the slope are symmetric and occur subvertically, reaching 3.0–3.5 m in width, while those located perpendicular to the slope dip are generally asymmetric, much narrower, with a width of 1.5–2.0 m in the upper part and their bedding varies from inclined to subhorizontal. The enclosing sediments at the contact with ice wedges are deformed, with the deformations traced as upwards curved schlieren of segregated ice. Segregated ice is characterized by medium-bedded medium- and fine lens- or belt-like cryostructures. In places where silty sands are overlapped by peat lenses, the thickness of ice schlieren in silty sands declines from 2–3 to 0.05 cm, while the peat material is characterized by densely layered micro-schlieren cryostructure. The cross-section is generally represented by three-fold

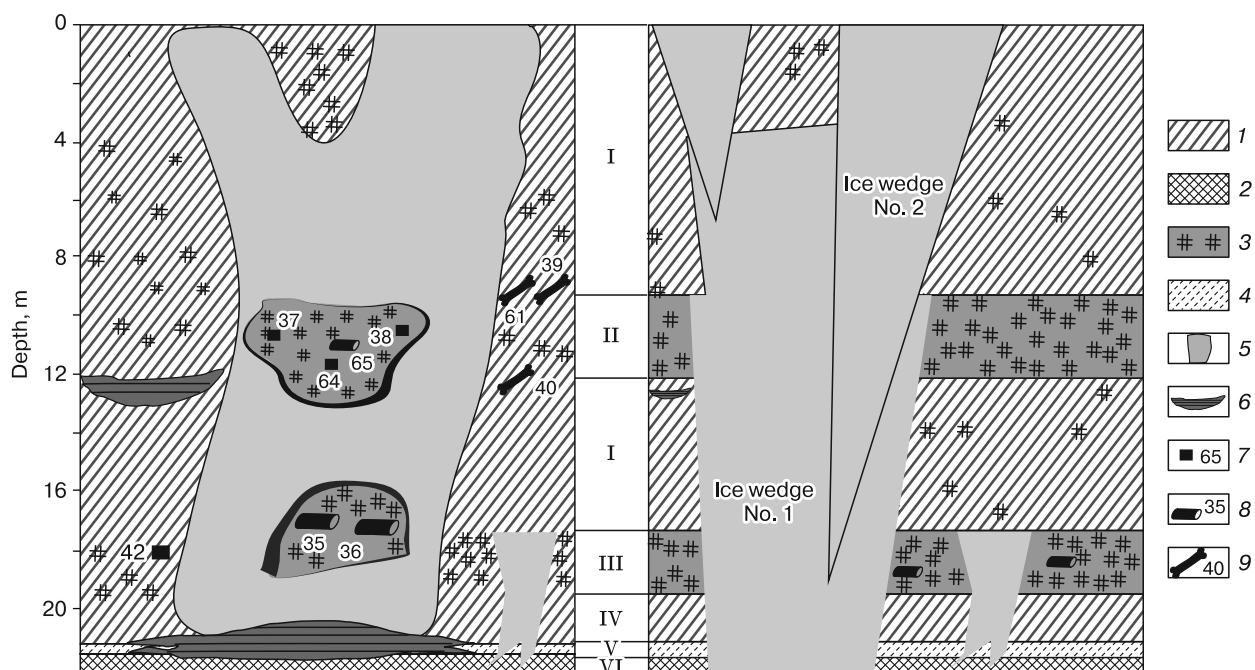


Fig. 7. Sampling points schematic and the structure of yedoma cross-section near Kular village.

I – solifluction-deluvial sediments; II – lacustrine-boggy sediments; III – alluvial-deluvial sediments; IV – deluvial sediments; V – alluvium; VI – eluvium. 1 – grey silty sand, frozen, peatified, with medium-to fine ice lenses lenticular cryostructure; 2 – medium to fine gravel with rubble; 3 – peat, frozen, with irregular reticulate and regular reticulate cryostructures; 4 – sand, black, fine, frozen; 5 – ice wedge; 6 – massive segregated ice. Sampling points (see Table 1) for: 7 – peat for ^{14}C -dating; 8 – wood for ^{14}C -dating; 9 – bones for ^{14}C -dating.

layering of silty sand units and peat lenses. The total moisture content of deposits averages 70–100 %.

The cryogenic structure of silty sands varies across different depth intervals, as follows: 17–12 m: lenticular layered (lenses up to 3 cm thick), complicated by 0.1 cm vertical ice lenses; 10.0–4.5 m: lenticular (ice lenses thickness: 2 cm); 4.5–0 m: grey silty sand, ice-poor, sparsely bedded, lenticular cryostructure with medium and fine ice lenses.

One of the ice wedges at the yedoma base has intruded into the bedrock eluvium composed by rubble, and, because of being thereby contorted, the direction of its growth changes. As such, the unusual shape of ice wedge, in our opinion, was caused by the eluvium debris acting as obstacles for frost cracks propagation. Given that this largely affected the orientation of frost cracks, ice wedges in the gravelly eluvium have a peculiar curved shape. Noteworthy is that syngenetic ice wedges of usual shape were reported from the intermountain basins of the upper Kolyma River [Vasil'chuk, Vasil'chuk, 1998]. In this case, they were completely buried in gravelly sediments slightly admixed with silty sand infill.

A lens of pure autochthonous peat occurring in the 10–12 m depth interval (this peat bog is probably the best descriptive of all Siberian yedoma sequences

that the authors have come across) is accentuated by incompletely decomposed twigs of shrubs, roots, stems of grass and mosses in the primary occurrence, which bears evidence of autochthonous origin of peat. The peat lens is characterized irregular reticulate cryostructure, which indicates parasynogenesis (according to Katasonov), when all-out freezing (from side, from bottom up and from top down) takes place immediately after sedimentation. Fossil bones (fauna remains of horse, mammoth, and bison) were found in the peripheral part of the peat lens. It stands to reason that because of its huge thickness, the layer of peat could have accumulated in the conditions of lake-bog landscapes.

In the lower part of the section (the 19–17 m depth interval), fragments of birch and larch trunks were encountered in silty sands exposed to significant peatification. There are no signs of autochthonous origin, while heterogeneous plant remains are characterized by rather chaotic distribution.

Affected by slope processes, the axes of ice wedges were displaced during aggradation of the yedoma sequence, hence, the ice wedges were found to be displaced relative to each other by 1.2–1.5 m (Fig. 7), i.e. similarly to those described by Gravis [1969] in the Kyusentey River valley (Fig. 4).

Table 1. Radiocarbon dating of organic material from yedoma sediments in the Kular cross-section

Sample ID	Depth, m	Type of the dated material	^{14}C -age, years BP	Lab. ID	Calibrated age, cal yr BP
340-YuV/39	9.0	Bone	37 700 \pm 600	GIN-4981	43 457–40 570
340-YuV/61	9.0	Horse bone	38 700 \pm 1000	GIN-4965	45 896–40 660
340-YuV/38	11.0	hII, peat	Over 36 900	GIN-4980	–
340-YuV/38	11.0	Peat	Over 23 800	GIN-4980	–
340-YuV/64	11.2	hII, peat	33 300 \pm 1100	GIN-4987	41 799–34 597
340-YuV/65	11.2	Twigs	42 400 \pm 1000	GIN-4982	49 630–43 435
340-YuV/37	11.5	Peat	35 700 \pm 1500	GIN-4979	45 935–35 911
340-YuV/40	12.0	Bone, skull	40 500 \pm 1200	GIN-4964	48 864–41 890
340-YuV/35	17.6	Wood	41 100 \pm 800	GIN-4977	47 244–42 769
340-YuV/36	17.8	Wood	Over 43 700	GIN-4978	–
340-YuV/42	18.0	Peat	Over 40 000	GIN-4983	–

Note. hII is hot alkaline extract.

Radiocarbon dating

Radiocarbon dating was performed at the Radiocarbon Laboratory of the Geological Institute of the Russian Academy of Sciences, with participation of L. Sulerzhitsky. Statistical parameters were derived from the data processing with the use of STATISTICA 10 software package. A series of dates were obtained for pure peat (with only few mineral inclusions), for wood from twigs, as well as for bone remains (Table 1; Fig. 7). All radiocarbon (^{14}C) dates were calibrated using the OxCal calibration and analyst software, v. 4.3 [Bronk Ramsey, 2009], based on the IntCal13 calibration data set [Reimer et al., 2013].

Because of the limitations of the radiocarbon method, dating of wood and peat in the lower peat lens, at a depth of 17.8–18.0 m is all but impossible, however, at a depth of 17.6 m, the estimated age of larch trunk varied between 47,244 and 42,769 cal yr BP (Fig. 8). Thus, reliable ^{14}C ages were obtained only for the lowermost part of the yedoma cross-section (the lowest 10 meters), which abounds with diverse organic material. Considering the slope deposi-

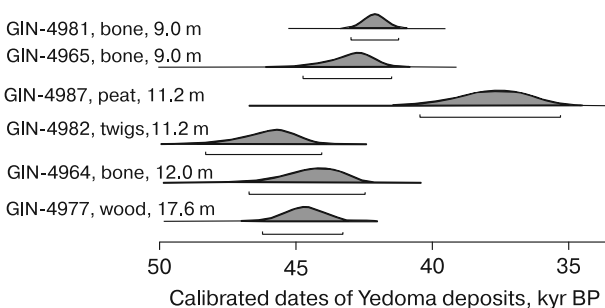


Fig. 8. Time intervals of yedoma deposits accumulation near Kular village according to ^{14}C -dating of bones, peat and wood.

Calibrated according to: [Bronk Ramsey, 2009; Reimer et al., 2013].

tional pattern, the dates obtained for wood, bone material and pure peat are generally consistent, i.e. the sediments accumulated synchronously in slope depositional environments may be localized in different parts of the slope.

History of the yedoma sequence accumulation

Results of the ^{14}C dating (Fig. 7, 8) demonstrated that the initiation of yedoma formation in the analyzed cross-section correspond to ca. 47(50),000 cal yr BP.

Wood recovered from a depth of 17.6 m was dated to ca. 47,000 cal yr BP, while peat from a depth of 11.2 m – to about 37,000 cal yr BP, i.e., yedoma deposits aggraded at a rate of about 0.7 m per 1 thousand years (this estimate is largely tentative, inasmuch as sedimentation regime changed significantly throughout the time of the sequence accumulation). Such a rate of vertical growth of ice wedges and enclosing sediments was interpreted by the authors to be constant for the Kular yedoma. It can be assumed that the uppermost 11 meters of the enclosing sediments accumulated during a time period spanning at least 10,000–17,000 yr BP. Proceeding from the fact that large syngenetic wedges inception as accumulation of peat and then silty sands and clayey silts, the period of their formation can be attributed to the interval straddling ca. 37,000–25,000 cal yr BP. Hence, accumulation of yedoma deposits had ceased not earlier than 25(22),000 cal yr BP, and probably later, inasmuch as the topmost unit has not been dated.

Most likely, intensive accumulation of peat which began about 47,000 cal yr BP, caused active synchronous growth of wedge ice which often intruded into the underlying eluvium. Intensive inundation probably occurred either within the polygonal ice wedge systems or in topographic lows. The erosion basis lowering ca. 42,000–40,000 cal yr BP entailed accumulation of solifluction silty sands that overlaps

the low-level peat bog in the cross-section. Ice wedges appear to have ceased to grow at that time, despite the harsh geocryological conditions that marked the period of formation of silty sands. About 37,000 cal yr BP, the erosion basis elevated again, which prompted accumulation of a thick peat layer and re-activation of the growth of ice wedges. The parameters characterizing the upper layer of peat bog include: its thickness in excess of 2 m; clear peat showing no mineral inclusions; *in situ* distribution of plant remains; peat material of probably autochthonous origin. To the authors' knowledge, there are no such thick autochthonous peat mantles of Late Pleistocene age in the northernmost permafrost regions. The accumulation of peat remarkably involves a combination of favorable factors, such as sufficiently high temperatures during the growing season and optimal moisture content. The phenomenon of frost cracking, whose episodes may have been quite common, resulted in extensive and deep fissuring, thereby promoting penetration of the middle-tier wedges to a depth 6–8 m and more. The tips of many newly formed mid-tier wedges reached the surface of the buried lower-tier wedges, to coalesce into a unified ice wedge. Given different penetration depth of the tips of newly formed wedges, some of them did not reach the earlier buried wedges. This process became recurrent concomitantly with silty sands accumulation 33,000–27,000 cal yr BP, which translated to intensive growth of ice wedges in width beginning ca. 27,000 cal yr BP. The largest wedges that formed during this period also intruded and merged with the previously formed ice-wedge complex, whereas the smaller ones or those standing somewhat apart formed independently.

The research results describing the structure of the studied yedoma cross-section near Kular village, as well as its comparison with region-specific yedoma structures, suggest a remarkable activity of deluvial solifluction processes involved in the formation of yedoma sequences next to alluvial and lacustrine-boggy sediments. Ice wedges aggraded on par with deposits accumulation. Initially, deposition of sediments hosting ice wedges occurred across the riverbed and floodplain facies, while involvement of slope processes was characteristic of the entire region at later stages. Structural analysis of the cross-sections revealed numerous similarities between the Kyusyuntey River valley slope [Gravis, 1969] and the Kular River slope sediments. Thus, a black fine-sand interlayer corresponds to the Burguat River alluvium, while formation of the overlying layer of peaty silty sands with tree trunks probably involved floodplain alluvium and deluvial solifluction sediments. This strongly suggests that the lens formed as a result of slope deposits slumping and their superimposition over alluvial sediments. The presence of woody vegetation in the interval spanning 47,244–42,769 cal yr BP re-

flects depositional environments affected by fairly high temperatures of the growing season (sufficient for the growth of trees), which activated the slope processes, although in places where woody vegetation was present, conversely, the slope processes may have been slowed down. Thus, accumulation of the yedoma slope tended to be more intense during warm summer seasons. During this period, besides the Kular ridge area, woody vegetation became also seen in the north, on Kotelny island [Galanin *et al.*, 2015; van Geel *et al.*, 2017; Vasil'chuk *et al.*, 2019] and Bolshoy Lyakhovsky Island [Wetterich *et al.*, 2014]. Twigs of shrubs were dated to 49,630–43,435 cal yr BP, lying approximately within the same interval [van Geel *et al.*, 2017]. Note that such mild climate (“climatic optimum”) conditions of early MIS 3 were defined by Wetterich and colleagues [2014] within the 48,000–38,000 cal yr BP interval for Bolshoy Lyakhovsky, and within 40,000–32,000 cal yr for the Lena River delta.

In addition to slope sediments, aggradation of wedge ice deposits in the Kular region was accompanied by syngenetic accumulation of yedoma deposits in river valleys. In the cross-section of Soplivaya Gora (195 km to the Yana River mouth), Basilyan and coauthors [2015] identified a total of 10 sedimentation cycles. The yedoma complex shapes the 40-meter surface area of the Soplivaya Gora cross-section and, in itself, represents a sequence of deposits exhibiting different facies types and containing syngenetic ice wedges that may reach 3–5 m or more in width. The sequence of sedimentation is highlighted by determinate up-section change in the lithological composition. The sedimentation cycles established by Basilyan and coauthors [2015] culminate in horizons with abundant organic matter, and are derived from the change in cryogenic structures associated with: i) corresponding levels of the cessation of ice wedge growth; ii) truncation of belt-like ice schlieren as a result of the ancient active layer base lowering or erosion which accompanies the formation of the overlying sediments. Alluvium of the second river terrace (16–18 m a.s.l.) composing a high, 40-meter surface, has cut into the sediments comprising the cultural layer of the Yana Palaeolithic site which dates to 28.5–27.0 ka BP [Pitulko *et al.*, 2004]. Deposits of the second terrace in the lower reaches of the Yana River [Pavlova *et al.*, 2015] are represented by syncryogenic sediments represented by the alluvium from the riverbed and floodplain facies with the polygonal ice wedge system divided into upper and lower ice-wedge generations and totaling 14–16 m in thickness. Initiation of both the intrusion [Basilyan *et al.*, 2015] and accumulation of the yedoma deposits is attributed to ca. 40 ka BP. Ice wedges occur on level with the cultural layer of the Yana site at elevation of 7.5–8.0 m above the river's water line.

The most favorable conditions in the vegetation period according to palynological data were reported from ca. 42 and 40–32 ka BP [Wetterich *et al.*, 2008] on Kurungnakh island in the Lena River delta, which corresponds to age of larch wood in the Kular yedoma cross-section 41 100 ± 800 years (47,244–42,769 cal yr BP). Noteworthy is that favorable conditions of the growing season were likely responsible for the intensified solifluction and deluvial processes, which caused both an increase in thickness of slope deposits related to this period, and peat bogs expansion in the region.

The descriptions discussed here, confirm an intensive formation of the yedoma complex throughout the Late Pleistocene cryochron in the foothills as well, rather than on the plains alone. A marriage of ice wedge complexes and organic material in the sequences is indicative of both a possible increase in winter severity, and some improvement in vegetation conditions during individual periods of the Late Pleistocene cryochron.

CONCLUSIONS

- The presence of Late Pleistocene multi-tier ice wedges in yedoma sequences whose accumulation involved inputs of slope material, is remarkable on hillslopes of the Kular ridge area (most often, in the cross-sections of terrace-ridges).
- At least two records of relatively high temperatures of the growing season during the Late Pleistocene have proven to be sufficient for existence of tree species.
- High rate of the solifluction material accumulation probably due to increased oversummer temperatures provided for considerable thicknesses of hillslope yedoma.
- Syngenetic ice wedges formed mainly during the two periods of the Late Pleistocene: 47–42 and 37–32 ka BP.
- An unusual shape of ice wedges in the lowermost part of the cross-section is associated with a change in the orientation of frost cracks diverted due to amassed debris inclusions.
- The hillslope ice wedges in the Kular ridge area are characterized by the ice wedges' axes displacement relative to the vertical position.

The authors express their most sincere gratitude to L.D. Sulerzhitsky for his help in radiocarbon dating and to Dr. M.O. Leibman for her participation in the field works.

The cryolithological and radiocarbon data analyses were financially supported by the Russian Science Foundation (grant no. 19-17-00126), and the summary of the research results and findings – by the Russian Foundation for Basic Research (project no. 18-05-60272).

References

- Alisov, B.P., 1956. Climate of the USSR. Moscow, Moscow University Press, 547 pp.
- Basilyan, A.E., Anisimov, M.A., Dorozhkina, M.V., 2015. Quaternary sedimentations cycles as a result of climate fluctuations in the Yana-Indigirka Lowland (reference section Soplivaya Gora/Yana–195 km). In: Fundamental Problems of the Quaternary: Results and Main Trends of Future Studies. Proc. IX Conf. on the Quaternary. Izd-vo Institute of Geography SB RAS, Irkutsk, pp. 43–45 (in Russian).
- Bronk Ramsey, C., 2009. Bayesian analysis of radiocarbon dates. Radiocarbon 51 (1), 337–360.
- Galanin, A.A., Dyachkovskiy, A.P., Lytkin, V.M., 2015. Results of absolute age dating of samples at the Radiocarbon Laboratory of Permafrost Institute SB RAS. Nauka i Obrazovanie (Science and Education), No. 4, 45–49.
- Gravis, G.F., 1969. Slope sediments in Yakutia: Depositional and freezing environment and cryogenic structure. Nauka, Moscow, 128 pp. (in Russian).
- Kanevskiy, M., 2003. Cryogenic structure of mountain slope deposits, northeast Russia. In: Proc. of the Eight Intern. Conf. on Permafrost (Zurich, Switzerland, 21–25 July, 2003). A.A. Balkema Publishers, Lisse, vol. 1, pp. 513–518.
- Kanevskiy, M.Z., 2004. Specific characteristics of the formation of cryogenic structure of Quaternary deposits in Northern Yakutia: Summary of PhD (geol.-min. sciences) thesis. Moscow, 23 pp. (in Russian).
- Konishchev, V.N., 1981. Formation of the Dispersed Rock Composition in the Cryolithosphere. Nauka, Novosibirsk, 198 pp. (in Russian).
- Konstantinov, M.M., Konstantinovskiy, A.A., Natalenko, M.V., 2013. Typification of gold-bearing regions in the terrigenous-black-shale belts of Russia. Regionalnaya Geologiya i Metallogeniya (Regional Geology and Metallogeny), No. 54, 75–88.
- Kuznetsova, T.P., 1967. Observations of ice-wedge polygons in the foothills of the Kular ridge. In: Ground Ice / A.I. Popov (Ed.). Moscow University Press, Moscow, iss. 3, pp. 94–101 (in Russian).
- Pavlova, E.Yu., Ivanova, V.V., Meyer, H., Pitulko, V.V., 2015. Stable isotopes of ground ice as an indicator of paleoclimate changes in the north of New Siberian Islands and in western Yana-Indigirka Lowland. In: Fundamental Problems of the Quaternary: Results and Main Trends of Future Studies. Proc. IX Conf. on the Quaternary (Irkutsk, 15–20 Sept., 2015). Izd-vo Institute of Geography, Irkutsk, pp. 349–351 (in Russian).
- Pitulko, V.V., Nikolsky, P.A., Giryay, E.Y., 2004. The Yana RHS site: humans in the Arctic before the Last Glaciation. Science 303, 52–56.
- Reference Books of the USSR Climate. 1966. Issue 24. Yakutia. Part 2. Air and Soil Temperature. Gidrometeoizdat, Leningrad, 403 pp. (in Russian).
- Reimer, P.J., Bard, E., Bayliss, A., et al., 2013. IntCal13 and marine13 radiocarbon age calibration curves 0–50 000 years cal BP. Radiocarbon 55, 1869–1887.
- Schirrmeister, L., Froese, D., Tumskey, V., Grosse, G., Wetterich, S., 2013. Yedoma: Late Pleistocene ice-rich syngenetic permafrost of Beringia. In: Encyclopedia of Quaternary Science: 2nd ed. / S.A. Elias, C.J. Mock (Eds.). Elsevier, Amsterdam, vol. 2, pp. 542–552.
- Sher, A.V., 1997. Yedoma as a store of paleoenvironmental records in Beringia. In: S. Elias, J. Brigham-Grette (Eds.). Beringia Paleoenvironments. Workshop, pp. 92–94.

- Soloviev, M.N., Fedyanin, A.N., Sorokina, K.M., 2003. State Geological Map of the Russian Federation. Scale 1:200,000 (2nd ed.). Verkhoyanskaya series. Sheet R-53-XV, XVI–Kular. Explanatory note. State Unitary Enterprise “Yangeology”, Batagay, 177 pp. (in Russian).
- van Geel, B., Protopopov, A., Protopopova, V., et al., 2017. Larix during the Mid-Pleniglacial (Greenland Interstadial 8) on Kotelny Island, Northern Siberia. *Boreas* 46, 338–345.
- Vasil’chuk, Yu.K., 1990. Isotope geochemical characteristics of Late Pleistocene ice-wedge complex of Kular depression. *Doklady AN SSSR* 310 (1), 154–157.
- Vasil’chuk, Yu.K., 1991. Reconstruction of the paleoclimate of the Late Pleistocene and Holocene on the basis of isotope studies of subsurface ice and waters of the permafrost zone. In: *Water Resources*. Publ. by Consultants Bureau. New York, vol. 17 (6), pp. 640–647.
- Vasil’chuk, Yu.K., 1992. Oxygen Isotope Composition of Ground Ice (Application to Paleogeocryological Reconstructions). *Theor. Probl. Dept. RAS, Moscow University, Research Institute of Engineering for Construction (PNIIS)*, Moscow, Book 1, 420 pp., Book 2, 264 pp. (in Russian).
- Vasil’chuk, Yu.K., Vasil’chuk, A.C., 1998. Oxygen-isotope and ^{14}C data associated with Late Pleistocene syngenetic ice-wedges in mountains of Magadan Region, Siberia. *Permafrost and Periglacial Processes* 9 (2), 177–183.
- Vasil’chuk, Yu.K., Makeev, V.M., Maslakov, A.A., Budantseva, N.A., Vasil’chuk, A.C., 2019. Late Pleistocene and Early Holocene winter air temperatures in Kotelny Island: reconstructions using stable isotope of ice wedges. *Earth’s Cryosphere XXIII* (2), 12–24.
- Ventskevich, S.D., Konishchev, V.N., Solomatin, V.I., 1969. Cryogenic effects on distribution of placer gold (with particular reference to the Kular region). In: *Problems of Cryolithology / A.I. Popov (Ed.)*. Moscow University Press, Moscow, vol. 1, pp. 50–62 (in Russian).
- Wetterich, S., Kuzmina, S., Andreev, A.A., 2008. Palaeoenvironmental dynamics inferred from Late Quaternary permafrost deposits on Kurungnakh Island, Lena Delta, Northeast Siberia, Russia. *Quatern. Science Rev.* 27 (15–16), 1523–1540.
- Wetterich, S., Tumskey, V., Rudaya, N., et al., 2014. Ice Complex formation in arctic East Siberia during the MIS3 Interstadial. *Quatern. Science Rev.* 84, 39–55.
- URL: <http://ru.climate-data.org/азия/российская-федерация/республика-саха-якутия/Казачье/> (last visited: 13.02.2019).

Received April 4, 2019

Revised version received September 2, 2019

Accepted September 14, 2019

GEOCRYOLOGICAL MONITORING AND FORECAST

DOI: 10.21782/EC2541-9994-2020-2(14-26)

PERMAFROST DEGRADATION: RESULTS OF THE LONG-TERM GEOCRYOLOGICAL MONITORING IN THE WESTERN SECTOR OF RUSSIAN ARCTIC

A.A. Vasiliev^{1,2}, A.G. Gravis¹, A.A. Gubarkov³, D.S. Drozdov^{1,2,5}, Yu.V. Korostelev¹, G.V. Malkova¹, G.E. Oblogov^{1,2}, O.E. Ponomareva^{1,5}, M.R. Sadurtdinov¹, I.D. Streletskaia⁴, D.A. Streletskiy^{1,6}, E.V. Ustinova^{1–3}, R.S. Shirokov¹

¹ Earth's Cryosphere Institute, Tyumen Scientific Center SB RAS, P/O box 1230, Tyumen, 625000, Russia; al.a.vasiliev@gmail.com

² Tyumen State University, 6, Volodarskogo str., Tyumen, 625003, Russia

³ Tyumen Industrial University, 38, Volodarskogo str., Tyumen, 625000, Russia

⁴ Lomonosov Moscow State University, Faculty of Geography, 1, Leninskie Gory, Moscow, 119991, Russia

⁵ Ordzhonikidze Russian State Geological Prospecting University – MGRI, 23, Miklukho-Maklai str., Moscow, 117997, Russia

⁶ George Washington University, Department of Geography, Washington, DC 20052, USA

The results of a long-term permafrost monitoring, which have been obtained at eight permafrost stations in the western sector of Russian Arctic, are presented. Increase in mean annual air temperatures in this area has reached approximately 2.8 °C (1970–2018). The data on mean annual ground temperature dynamics have been obtained for the active layer and upper permafrost for dominant landscapes of various bioclimatic zones: typical tundra, southern tundra, forest tundra, and northern taiga. Three stages of permafrost stability under the warming climate were determined: stable permafrost, unstable permafrost, and actively degrading permafrost. It was shown that permafrost degradation leads to active development of vegetation and migration of the boundaries of bioclimatic zones 30 to 40 km towards the north (1975–2018).

Permafrost, ground temperatures, long-term monitoring, permafrost stations, permafrost degradation, intermediate layer

INTRODUCTION

In recent decades, the problem of permafrost degradation due to climate warming in the Arctic has become a priority. Permafrost plays an important role in global climate change, the balance of greenhouse gases, changes in Arctic ecosystems, and land management in the Arctic regions [Nelson *et al.*, 2001; Hinzman *et al.*, 2005; Romanovsky *et al.*, 2010; AMAP, 2011; IPCC, 2013]. Climate warming in the western sector of the Russian Arctic has been recorded since 1970. In this area, an increase in air temperature, duration of the warm period, a change in the amount of precipitation, and an increase in the thickness of the snow cover have been observed [Pavlov, Malkova, 2005].

As a result of the complex effect of climatic factors on the permafrost in the last 40–50 years, the temperature of permafrost has increased, and the thickness of the active layer has increased as well [Pavlov, 1997; Osterkamp, Romanovsky, 1999; Romanovsky, 2006; Oberman, 2008; Vasiliev *et al.*, 2008; Smith *et al.*, 2010; Vasil'chuk, Vasil'chuk, 2015a,b; Streletskiy *et al.*, 2015a; Kaverin *et al.*, 2017; Boike *et al.*,

2018; Biskaborn *et al.*, 2019]. Near the southern boundary of the permafrost, the area underlain by permafrost is likely to decrease, and lowering of the permafrost table currently occurs [Streletskiy *et al.*, 2015b].

Prediction of changes in the permafrost characteristics has been recently improved due to elaboration of new methods of climate modeling and development of global and regional climate models. Climate models describe the dynamics and spatial distribution of climatic characteristics over the coming decades relatively well. Based on existing climate models, global and regional estimates of changes in permafrost characteristics have been made [Anisimov *et al.*, 2003; Nicolsky, Romanovsky, 2018]. Romanovsky and his coauthors presented small-scale maps of the predicted changes in the mean annual temperature of the active layer that are expected by 2050 and 2100 [Romanovsky *et al.*, 2008]. These maps show a wide band along the southern boundary of permafrost where permafrost thawing from above is expected.

The English text is published as edited by the authors.

Copyright © 2020 A.A. Vasiliev, A.G. Gravis, A.A. Gubarkov, D.S. Drozdov, Yu.V. Korostelev, G.V. Malkova, G.E. Oblogov, O.E. Ponomareva, M.R. Sadurtdinov, I.D. Streletskaia, D.A. Streletskiy, E.V. Ustinova, R.S. Shirokov, All rights reserved.

Shur and Jorgenson [2007] considered possible ways of permafrost degradation due to climate warming and human-induced surface disturbances. They noted that vertical and lateral degradation of permafrost is possible as a result of its reaction on both climatic and non-climatic impacts.

Thus, we can conclude that permafrost response to climatic changes is described in the scientific literature mainly based on estimates and calculations, while there is a significant lack of real observations of permafrost degradation in various bioclimatic zones.

Until now, there is no scientific consent on what changes in permafrost can be attributed to its degradation: only its transition from frozen state to unfrozen caused by increase in the mean annual temperature of permafrost [Paffengolz *et al.*, 1973], or reduction in cold resources in permafrost caused by natural and anthropogenic impacts that lead to decrease in the area of permafrost distribution, increase in temperature, and decrease in the thickness of permafrost, which may eventually lead to its disappearance [Baulin, Murzaeva, 2003].

Following Burn [2004], we consider that permafrost is degrading if at least within some part of permafrost sequence (usually the upper one) mean annual ground temperatures have become positive. In this work, we focus on the most critical case of permafrost degradation, when continuing thawing of the upper horizon of permafrost and lowering of the permafrost table are observed.

STUDY AREA

The dynamics of permafrost under changing climate have been monitored at eight permafrost stations located within all major bioclimatic zones of the western sector of the Russian Arctic – from typical tundra to northern taiga (Fig. 1).

The boundaries of bioclimatic zones were determined when in a circumpolar map of vegetation [Walker *et al.*, 2009]. Studies of the permafrost thermal regime have been performed in boreholes located in all dominant landscapes characterizing the territory adjacent to the station area in undisturbed conditions, except two boreholes of the South Urengoy station. In 2003–2006, observations of the permafrost temperature in boreholes were included in the GTN-P program (Global Terrestrial Network for Permafrost) [Biskaborn *et al.*, 2015]. At all permafrost monitoring stations, observations of the active layer thickness have been performed at previously established grids according to the CALM protocol (Circumpolar Active Layer Monitoring) [Brown *et al.*, 2000].

Marre-Sale Station. The permafrost monitoring station is located in the typical tundra zone on the west coast of the Yamal Peninsula, near the weather station of the same name. The vegetation cover consists mainly of shrubs, mosses, and lichens. The region

belongs to the continuous permafrost zone. Observations of the thermal regime of permafrost were performed in five 10-m-deep boreholes located in dominant landscapes on the surface of the third marine terrace (1978–2018) and in one borehole on the tidal flats (1978–2001). The elevations of the surface of the third marine terrace are 20 to 30 m a.s.l., and of the tidal flats are 2.5 m a.s.l. In 1995, the CALM grid was established, where the active layer thickness have been measured annually, and the thermal regime of permafrost has been studied to a depth of 2.0 m. Climate data were obtained from the Marre-Sale weather station.

Cape Bolvanskiy Station. The permafrost station is located on the Barents Sea coast close to the Pechora River delta in the southern tundra zone. The vegetation cover consists mainly of shrubs, mosses, and lichens. This area belongs to the continuous permafrost zone. The CALM grid was established here in 1999. Observations of the thermal regime have been performed in six boreholes 10 to 12 m deep, located nearby on the surface of the third marine terrace with elevations of 24 to 30 m a.s.l., as well as in the active layer at the CALM grid. Observations covered all dominant landscapes. To analyze climatic fluctuations, we used the data obtained from the Cape Konstantinovskiy weather station, located at a distance of about 50 km northeast of the station.

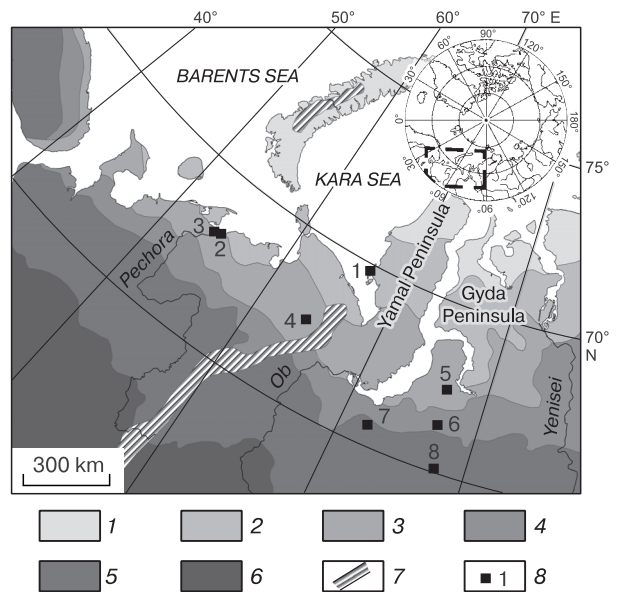


Fig. 1. Location of permafrost monitoring stations in different bioclimatic zones of the western sector of Russian Arctic.

1 – northern (arctic) tundra; 2 – typical tundra; 3 – southern tundra; 4 – forest tundra; 5 – northern taiga; 6 – typical taiga; 7 – mountain permafrost; 8 – numbers of stations: 1 – Marre-Sale, 2 – Cape Bolvanskiy, 3 – Kumzha, 4 – Vorkuta, 5 – Severniy (North) Urengoy, 6 – Yuzhniy (South) Urengoy, 7 – Nadym, 8 – Tarko-Sale.

Table 1. Metadata for borehole monitoring in the western sector of Russian Arctic

Monitoring station, coordinates	Bioclimatic zone	Permafrost extent	Boreholes, observation period (years)	B-hole depth, m	Landscape, surface conditions	Vegetation cover	Soil texture
Marre-Sale (Western Yamal), 69°43' N, 66°49' E	Typical tundra	Continuous	1 (1978–2018)	10	Damp tundra	Shrub-Moss-Lichen	Silt
			3 (1978–2018)	10	Wet tundra	Shrub-Lichen-Moss	Silt, sand
			6 (1978–2018)	10	Well-drained tundra	Shrub-Moss-Lichen	Silt, sand
			17 (1979–2018)	10	Peatland	Shrub-Lichen-Moss	Peat up to 1.6 m, silt
			36 (1978–2001)	10	Tidal flat, bog	Sedge-Moss	Peat up to 0.3 m, sand
43a (1978–2018)	10	Sandy blowout	No vegetation	Sand			
Cape Bolvanskiy, 68°17' N, 54°30' E	Southern tundra	Continuous	54 (1983–1993, 1999–2018)	12	Moist tundra	Moss-Lichen	Sand, silt, and silty clay interbedding
			55 (1983–1993, 1999–2018)	10	Polygonal peatland	Moss-Lichen	Peat up to 4 m, underlain by silty clay
			56 (1983–1993, 1999–2018)	10	Peatland	Moss-Lichen	Peat up to 2 m, underlain by silty clay
			59 (1983–1993, 1999–2016)	12	Well-drained tundra	Lichen-Moss with frost boils	Silty clay with gravel
			65 (1983–1993, 1999–2018)	12	Moist tundra	Moss-Lichen	Sand and silty clay interbedding
			83 (1983–1993, 1999–2016)	10	Well-drained tundra	Lichen-Moss	Silt and silty clay interbedding
Kumzha, 68°11' N, 53°47' E	Southern shrub tundra	Sporadic	3 Ku (2016–2018)	6	Well-drained shrub tundra	Shrub-Lichen-Moss	Sand with gravel
Vorkuta, 67°35' N, 64°10' E	Southern tundra	Discontinuous	CALM R2 (1999–2017)	0.5	Damp tundra	Moss-Shrub	Silty clay
Severnii (Northern) Urengoy, 67°28' N, 76°42' E	Southern tundra	Continuous	15-03 (1975–2018)	10	Damp flat river valley bottom	Shrub-Moss with sporadic peatlands and bogs	Silty clay
			15-06 (1975–2018)	10	Drained erosion-talus slope	Willow and alder up to 2.5 m high with grass	Silt, silty clay
			15-08 (1975–2018)	10	Drained hilltop	Shrub-Moss	Silty clay
			15-20 (1975–2018)	10	Drained hilltop	Shrub-Moss	Silty clay
Yuzhniy (Southern) Urengoy, 66°19' N, 76°54' E	Forest tundra	Discontinuous	5-01 (1975–2018)	10	Drained slope	Clear-cut larch forest with shrubs up to 1.5 m	Silt, silty clay
			5-03 (1975–2018)	10	Top of palsa	Sporadic undergrowth of birch and larch	Silt, silty clay
			5-07 (1975–2018)	10	Boggy water track	Shrubby mounds and tussocks divided by small grassy bogs	Peat up to 1 m, silty clay
			5-08 (1977–2010)	10	Well-drained slope	Larch forest	Sand
			5-09 (1975–2018)	10	Disturbed surface	Burnt birch forest with undergrowth of shrub and birch	Sand
5-10 (1977–2018)	10	Drained slope	Larch forest	Sand, silt			
Nadym, 65°18' N, 72°51' E	Northern taiga	Sporadic	11-75 (1975–2018)	10	Large-mound peatland	Grass-Shrub-Moss-Lichen	Peat up to 1 m, sand
			14-72 (1972–2018)	10	Flat-mound peatland	Grass-Shrub-Moss-Lichen	Peat up to 0.5 m, sand
			23-75 (1975–2018)	10	Bog	Shrub-Grass-Moss	Peat up to 0.5 m, sand, silty clay
			1-71 (1971–2018)	10	Lithalsa	Grass-Shrub-Moss-Lichen	Peat up to 0.3 m, sand
Tarko-Sale, 65°02' N, 77°30' E	Northern taiga	Isolated	1 T-S (2006–2019)	30	Flat-mound peatland	Shrub-Moss-Lichen	Peat, sand, silt, clay
			2 T-S (2006–2019)	30	Drained ridge	Coniferous undergrowth with shrubs	Peat, sand, silty clay, clay

Kumzha Station. The permafrost station is located in the Pechora River delta in the southern tundra zone, 32 km south-west of Bolvanskiy station. The vegetation cover is represented by moss-lichen communities; shrubs are common in depressions. The site is located within the remnant of the first alluvial terrace with elevations of 5 to 8 m, surrounded by the channels of the Pechora River. This area belongs to the sporadic permafrost zone. Permafrost table is dome shaped and lies at a depth from the surface ranged from 2.6 m (in the center of the remnant) to 7.1 m (in its marginal parts). The CALM grid was established in 2016 in the central part of the remnant. To monitor dynamics of the depth to the permafrost table at this site, in addition to directly measuring with the permafrost probe along the established profiles, seismic and ground-penetrating radar (GPR) surveys have been performed annually [Sadurtdinov *et al.*, 2018]. To study permafrost structure and thermal regime, three boreholes were drilled in 2016; temperature of the active layer has been monitored in two boreholes, and a third borehole (No. 3 Ku) has been used to monitor the thermal regime of permafrost.

Vorkuta Station. Data on permafrost dynamics at this station are presented here based on the study by Kaverin *et al.* [2017]. The CALM grid in this area was established in 1999, about 13 km to the north-west of the city of Vorkuta. At this grid, a full cycle of observations of thaw depths and thermal regime of the active layer has been performed annually. This area belongs to the discontinuous permafrost zone. The site is represented by shrub-moss tundra with numerous frost boils at various stages of vegetation development. Dwarf birch and willow up to 50 cm high are observed in this area [Mazhitova *et al.*, 2004]. Climatic data were obtained from the Vorkuta weather station.

Severniy (North) Urengoy Station. The permafrost station is located about 180 km north of the city of Noviy Urengoy in the southern tundra zone. The vegetation cover is represented mainly by shrub-grass-moss communities within gentle hills and grass-moss communities in hasyreys (thaw-lake basins) and depressions. The area is located within the continuous permafrost zone. Observations of the thermal regime of permafrost have been performed since 1975 in four boreholes located in dominant landscapes on the third marine terrace with elevations 30 to 35 m a.s.l. The CALM grid was established in 2008, but the thermal regime of the active layer has not been studied. To analyze climatic fluctuations, we used the data obtained from the Noviy Urengoy weather station.

Yuzhniy (South) Urengoy Station. The permafrost station is located about 30 km north of the city of Noviy Urengoy in the forest-tundra zone, on the surface of the fourth lacustrine-alluvial plain with elevation of 60 to 70 m a.s.l. The vegetation is repre-

sented by poorly developed woodlands with larch-birch-lichen communities. Shrub-moss communities are common within peat bogs and tundra areas, and shrubs are common in gullies and depressions. Frost mounds are covered with sparse forests. The region belongs to the discontinuous permafrost zone. Observations of the thermal regime of permafrost started in 1975 in five boreholes. Boreholes 5-01 and 5-09 are located within landscapes with disturbed vegetation cover. In 2008, the CALM grid was established; however, observations of the thermal regime of the active layer have not been performed. Climatic characteristics were obtained from the data of the Noviy Urengoy weather station.

Nadym Station. The permafrost station is located 30 km from the city of Nadym in the northern taiga zone on the surface of the third lacustrine-alluvial terrace with elevations of 30 to 40 m a.s.l. The vegetation is represented by larch and birch sparse forest with grass-moss-lichen cover in combination with peat plateaus and flat bogs with shrub-moss-lichen cover. Peat and peat-mineral mounds are abundant. The area belongs to the sporadic permafrost zone. Permafrost occurs mainly within bogs, peatlands, and peat and peat-mineral frost mounds (palsas and lithalsas). Observations of the thermal regime of permafrost have been performed in four boreholes located on mounds and in a frozen bog. The CALM grid was established in 1995; active-layer thickness and temperature measurements have been performed here annually. Climate data were obtained from the Nadym weather station.

Tarko-Sale Station. The study of the thermal regime of the permafrost at this station has been performed since 2006 by employees of the Tyumen Industrial University. The station is located in the northern taiga, within the third lacustrine-alluvial terrace with elevations of about 34 m a.s.l. The vegetation is represented by larch and birch sparse forests with shrub-moss-lichen cover. The area belongs to the sporadic permafrost zone. Temperature measurements have been performed in three boreholes, two of which were drilled on a frost mound and a drained ridge. Observations under the CALM program started in 2018. Temperature measurements in the active layer have been performed to a depth of 1.0 m. Climate data were obtained from the Tarko-Sale weather station, located about 30 km from the station.

The characteristics of all boreholes, which provided the data that were used in this paper, are presented in Table 1.

OBSERVATION METHODS

At each permafrost monitoring station in all dominant landscapes, observations of the thermal regime of permafrost have been performed in boreholes with a depth of 10 to 12 m, which approximately corresponds to the depth of zero annual amplitude. At

the Tarko-Sale station, the boreholes have a depth of 30 m.

All boreholes were drilled in various years (from 1975 to 2016) using the M-10 manual drill equipped with a small gasoline-powered engine with continuous collection of frozen cores. A detailed description of soil texture and cryostratigraphy of frozen deposits was made, along with sampling of frozen cores every 0.5 m to determine physical and chemical properties. The boreholes were equipped for long-term measurements of ground temperatures in accordance with the generally accepted methodology [Grechishchev, Melnikov, 1989].

Until 2003, temperature measurements in boreholes were performed using high-inertia thermometers. The standard installation depths for thermometers were 0.5, 1.0 m, and then every meter throughout the depth of boreholes. Measurements were taken every 10 days, and after 1990 once a year at the end of warm season. The accuracy of temperature measurements was ± 0.1 °C. Thermometers located at the bottom of boreholes with a depth of 10 to 12 m showed the permafrost temperatures, which we considered to be the mean annual ground temperature even for a single measurement, because at this depth the ground temperatures practically do not experience seasonal fluctuations during the year. After 2003, 4-channel HOBO U12 loggers were installed in the boreholes. According to the GTN-P protocol [Biskaborn *et al.*, 2015], the required sensor installation depths were 2, 3, 5, and 10 or 12 m. In some boreholes, two loggers were installed; in these cases, ground temperatures were measured at depths of 0.5, 1, 2, 3, 4, 5, 7, and 10 or 12 m. Measurements have been taken every 6 hours. HOBO U12 loggers provide accuracy of ± 0.1 °C in measuring ground temperatures.

To measure soil temperature in the active layer, 2-channel HOBO Pro v2 loggers with measurement accuracy of ± 0.1 °C were used. Depending on the thickness of the active layer, one or two loggers with sensors installed every 0.5 m were used.

A position of the permafrost table up to a depth of 2.0 m was detected using a steel permafrost probe. For depths of 2.0 to 3.5 m, manual drilling was used every 2 to 3 years. For greater depths of the permafrost table, seismic methods were used [Melnikov *et al.*, 2010]. In sand sediments, GPR survey proved itself to be efficient for determining the permafrost table for depths of up to 10 m [Sadurtdinov *et al.*, 2018]. GPR surveys have been used annually at the Kumzha site, and in 2018 they were also performed at the Nadyim station. The determination of the permafrost table position with seismic methods in the areas of Yuzhniy (Southern) Urengoy, Severniy (Northern) Urengoy, and Nadyim has been performed every 2 to 3 years. The accuracy of estimation of the permafrost table position is 0.3 m for seismic methods, and approximately 0.2 m for GPR surveys.

CLIMATIC CONDITIONS

According to climatic zoning of the Arctic [Prik, 1971], the western sector of the Russian Arctic belongs to the Atlantic sector of the Arctic Ocean. This area is heavily influenced by mid-latitude circulation processes, especially the Iceland Depression. Based on climatic features, this area is divided into three zones. The northern tundra of the Yamal Peninsula and the Gydan Peninsula is characterized by marine Arctic climate. The typical and southern tundra of the European North, the central and southern parts of Yamal, and the Gydan and Taz Peninsulas belong to the zone with marine subarctic climate. The southern part of this area (forest-tundra and northern taiga) are characterized by temperate continental climate.

Main characteristic feature of the climate of the western sector of the Russian Arctic is an increase in the severity of the climate from west to east. According to the data of the Arkhangelsk weather station (64°30' N, 40°44' E), the mean annual air temperature in the western part of the region is 0.8 °C, while in the eastern part, according to the Dikson weather station (73°30' N, 80°24' E), it drops to -11.8 °C.

The current stage of climate warming in the western sector of the Russian Arctic began in the 1970s and has occurred synchronously throughout the entire region.

Monthly average climate characteristics were obtained from the websites [www.meteo.ru/data] and [www.rp5.ru]. Daily average characteristics were obtained from archives directly at the weather stations.

The change in the mean annual air temperature over time recorded at weather stations adjacent to permafrost monitoring station is shown in Fig. 2.

In general, an increase in mean annual temperature occurs synchronously with minor local fluctuations. From 1970 to 2018, the region's mean annual air temperature rose by approximately 2.8 °C, which is close to the "harsh" scenario of climate change [IPCC, 2013]. The minimum warming trend was 0.052 °C/year (Noviy Urengoy), the maximum 0.072 °C/year (Tarko-Sale). An analysis of spatial changes showed that from 1970 to 2018 a shift in the contours of the mean annual air temperature of approximately 80 to 100 km to the northeast has occurred [Malkova *et al.*, 2018].

Analysis of data on annual precipitation shows that in the western sector of the Russian Arctic a slight increase of 1–3 mm/year occurred in 1970–2018. This value approximately corresponds to the projected estimates based on the use of the ensemble of 12 CMIP5 climate models [Linderholm *et al.*, 2018]. Moreover, in the areas of Nadyim and Urengoy with a temperate continental climate, the increase in the annual amount of precipitation is slightly larger than in areas with a temperate marine climate.

The formation of the thermal regime of permafrost is greatly affected by snow cover. Snow cover in

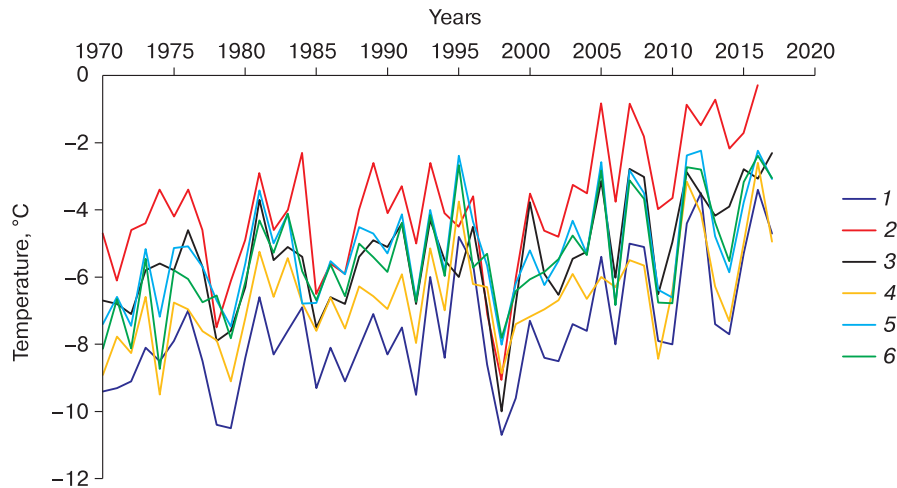


Fig. 2. Changes in mean annual air temperatures over time in the western sector of Russian Arctic.

1 – Marre-Sale; 2 – Cape Konstantinovskiy; 3 – Vorkuta; 4 – Noviy (New) Urengoy; 5 – Nadym; 6 – Tarko-Sale.

the study area begins to form in the first 10 days of October, reaches its maximum in April, and completely disappears by the end of May.

The greatest thickness of the snow cover is observed in the bioclimatic zones of forest-tundra and northern taiga. In Urengoy, its average value is approximately 114 cm, in Nadym – 85 cm, and in Tarko-Sale – about 90 cm. In the zones of typical and southern tundra, a thickness of the snow cover is much smaller: at Cape Bolvanskiy, average long-term thickness of the snow cover is about 58 cm, in Vorkuta – 44 cm, and in Marre-Sale – 33 cm. At all weather stations, an increase in the maximum thickness of the snow cover with time has been observed. Its greatest increase has occurred in the tundra zone, where the rate of increase in the maximum thickness of the snow cover reaches 1.8 cm/year (1998–2018), while in the zone of the forest-tundra and northern taiga this rate is 0.6 cm/year (2003–2018).

Discussion on the permafrost monitoring results

The results of long-term monitoring of the mean annual ground temperature at a depth of zero annual amplitudes are shown in Fig. 3. According to this figure, in all bioclimatic zones and dominant landscapes an increase in the mean annual ground temperature with warming climate has been observed. At the same time, the rate of increase in the mean annual ground temperature in various bioclimatic zones is not equal with an approximately equal increase in the mean annual air temperature of 2.8 °C, which corresponds to the average long-term climate warming trend of 0.06 °C/year (1970–2018).

The largest changes in the mean annual ground temperature have been observed in the zone of typical tundra. The average increase in ground temperature

have reached 0.056 °C/year. Moreover, all landscapes are characterized by approximately the same reaction to climate warming. Despite a significant increase in the mean annual ground temperature, permafrost these days is characterized by low temperatures ranging from -3.5 to -5.0 °C, and its condition is still stable.

In the zone of southern tundra in the Northern (Severnii) Urengoy region, the rate of average increase in the mean annual ground temperature for various landscape conditions has been approximately 0.05 °C/year. This region includes landscapes with relatively high and low mean annual temperatures of permafrost. In “cold” landscapes with shrub-moss vegetation, the highest increase in mean annual temperature from -5.5 °C (1975) to -3.5 °C (2018) has been observed in well-drained areas (boreholes 15-03, 15-08, and 15-20). At the same time, within the well-drained “warm” areas with a high shrub vegetation (borehole 15-06), mean annual ground temperature has increased only by 1.0 °C: from -1.8 °C (1978) to -0.8 °C (2018).

The slow reaction of high-temperature permafrost to climate change is also typical of the southern tundra landscapes of the European North. Due to sectoral differences in climatic characteristics within the same landscape conditions, permafrost conditions observed in the European North of Russia have been warmer than in Western Siberia [Drozdoz *et al.*, 2012]. At the Bolvanskiy station, an average increase in mean annual ground temperatures for various landscapes was 0.04 °C/year. In 1980s, mean annual ground temperature at a depth of 10 m varied from -0.8 to -2.5 °C, and during the monitoring period it increased by 0.2 to 1.2 °C, while the range of variations in mean annual ground temperature in various landscapes has decreased almost threefold and tem-

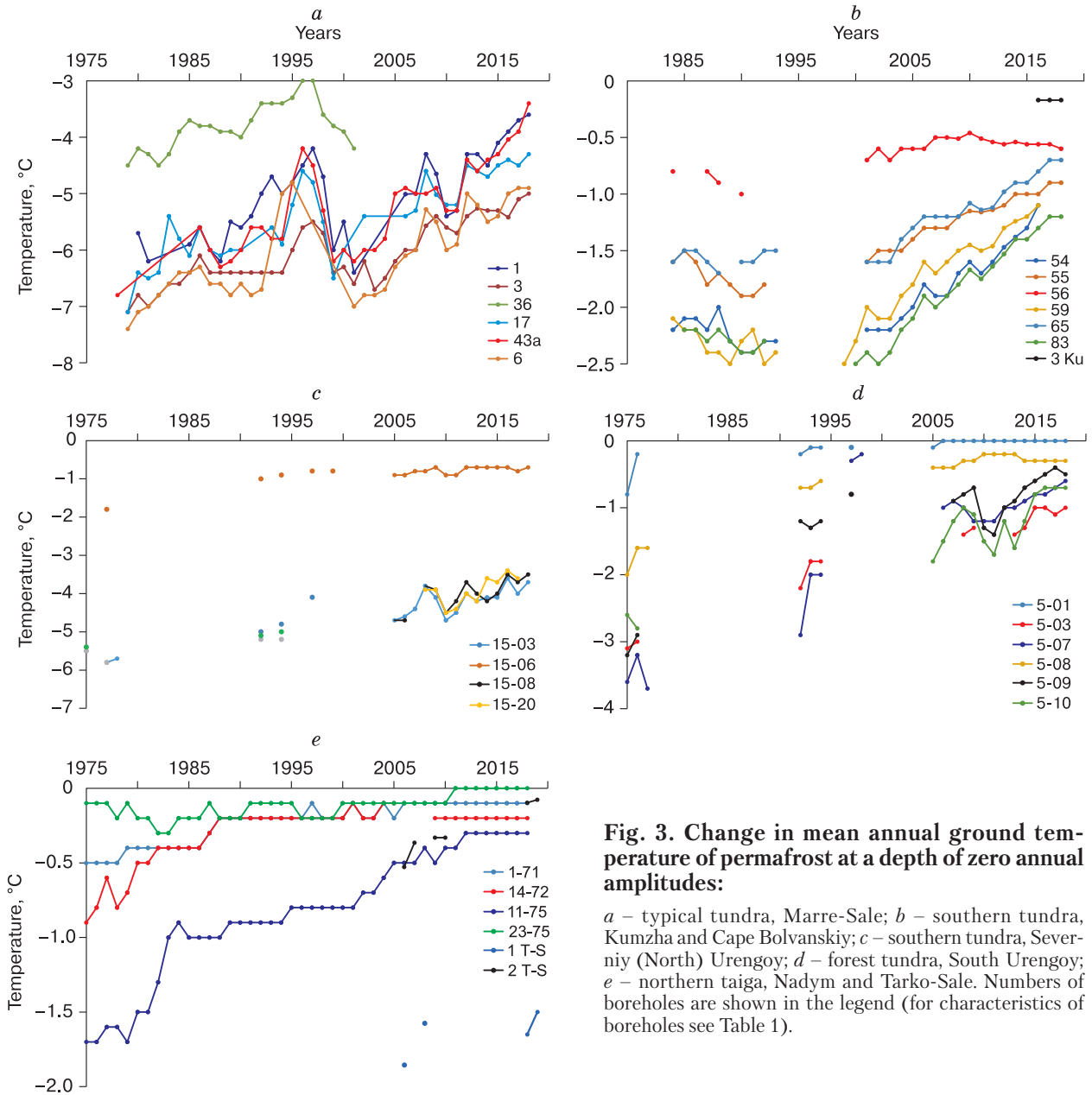


Fig. 3. Change in mean annual ground temperature of permafrost at a depth of zero annual amplitudes:

a – typical tundra, Marre-Sale; *b* – southern tundra, Kumzha and Cape Bolvanskiy; *c* – southern tundra, Severniy (North) Urengoy; *d* – forest tundra, South Urengoy; *e* – northern taiga, Nadym and Tarko-Sale. Numbers of boreholes are shown in the legend (for characteristics of boreholes see Table 1).

temperatures currently vary from -0.6 to -1.2 °C [Malikova et al., 2018].

In the forest-tundra zone, in the area of Southern (Yuzhniy) Urengoy station, the rate of increase in the mean annual ground temperature in relatively “cold” sparsely forested landscapes (boreholes 5-03, 5-07, 5-08, and 5-09) was about 0.045 °C/year. In borehole 5-01, mean annual ground temperature, measured at a depth of 10 m, increased from -0.8 to 0 °C and by 2012 permafrost in the borehole area had completely thawed to a depth of 10 m. At the end of 1970s, after a forest was cut down here, the conditions of heat exchange changed abruptly, and progressive thawing of the permafrost from above began. A similar situation

occurred in the area of borehole 5-08 located on a well-drained slope. Although deforestation did not occur here, permafrost began to thaw gradually from mid-1970s and thawed to a depth of 7 m by 2010. At the same time, mean annual ground temperature in borehole 5-08 at a depth of 10 m remained negative and fluctuated between -0.2 and -0.35 °C during the entire observation period.

In the northern taiga zone, at the Nadym station, mean annual ground temperature in peat mounds has increased from -1.7 to -0.3 °C, while within other landscapes it raised close to the thawing point and reached -0.2 to 0 °C by 2018. In this area, permafrost thawing has been observed in bogs where the depth of

the permafrost table has reached approximately 4.0 m. At the Tarko-Sale station, mean annual ground temperature on the frost mound has increased from -1.9 to -1.6 °C (2006–2019), and on the drained ridge – from -0.6 to -0.1 °C, while the permafrost table has lowered to a depth of 6 m.

Thus, during the climate warming that has resulted in temperature increase of 2.8 °C (1970–2018), mean annual ground temperature still remains negative almost everywhere, except borehole 5-01 (South Urengoy), where the temperature has become positive but still close to 0 °C. In the areas of boreholes 23-75 (Nadym) and 2 T-S (Tarko-Sale), where mean annual ground temperature at a depth of 10 m has increased up to -0.1 °C, thawing of permafrost from above has been already observed. It means that mean annual ground temperature, measured at a depth of zero annual amplitudes, cannot characterize the physical state of the upper permafrost, whose uppermost horizons can be both frozen and unfrozen. This problem is related not to measurement errors but to the nature of distribution of mean annual ground temperatures with depth. Figure 4 shows the values of maximum, minimum, and mean annual ground temperatures in 2017 for two bioclimatic zones. In both cases, the distribution curves of mean annual ground temperature with depth show higher temperatures in the upper part of the section and indicate a tendency to warming that follows changes in temperature during the previous year.

In the typical tundra zone, mean annual ground temperature at a depth of 1.0 m was -3.14 °C, and at a depth of 10 m it was -3.7 °C. In the northern taiga zone it was $+0.16$ and -0.1 °C, correspondingly. In the

first case, permafrost was overlain directly beneath the active layer. In the second case, mean annual ground temperature had positive values to a depth of 4.0 m, and, therefore, the permafrost table was lowered to this depth.

Thus, in conditions of climate warming, negative mean annual ground temperature, measured at a depth of zero annual amplitudes, does not guarantee the frozen state of the overlying deposits. We should also emphasize that within the same bioclimatic zone there may be landscapes with varying levels of resistance to climate change [Vasiliev *et al.*, 2008; Drozdov *et al.*, 2012; Malkova *et al.*, 2018].

Permafrost thawing starts when mean annual ground temperature changes to positive values within any part of the permafrost sequence. With climate warming, such a transition is expected primarily in the upper horizons of permafrost [Burn, 2004]. Analysis of changes in mean annual ground temperatures in the active layer showed that in some cases such a transition has already occurred in the western sector of the Russian Arctic (Fig. 5). According to this figure, mean annual ground temperatures of the active layer since 2007 have had positive values at almost all permafrost monitoring stations except Marre-Sale (typical tundra). This means that soils of the active layer have already transformed from seasonally thawed to seasonally frozen state, i.e. permafrost degradation and transition of mean annual ground temperatures of the active layer to the positive values have already occurred. We should emphasize that this transition of the active layer from seasonally thawed to seasonally frozen state at the Cape Bolvanskiy station already occurred in 2010 while mean annual

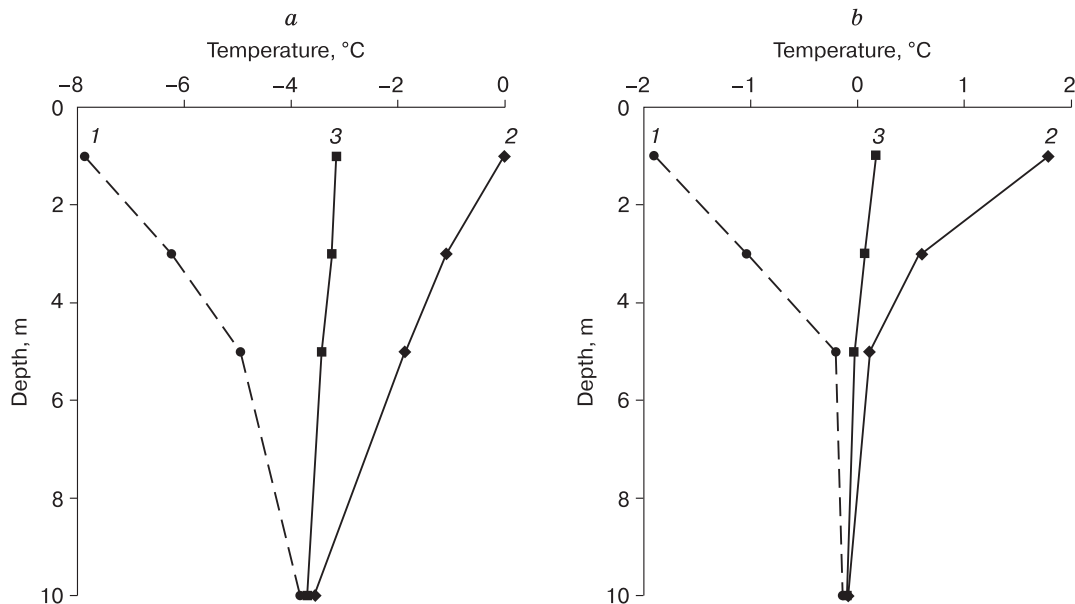


Fig. 4. Distribution of minimum (1), maximum (2), and mean annual ground (3) temperature with depth: *a* – typical tundra, Marre-Sale; *b* – northern taiga, Nadym.

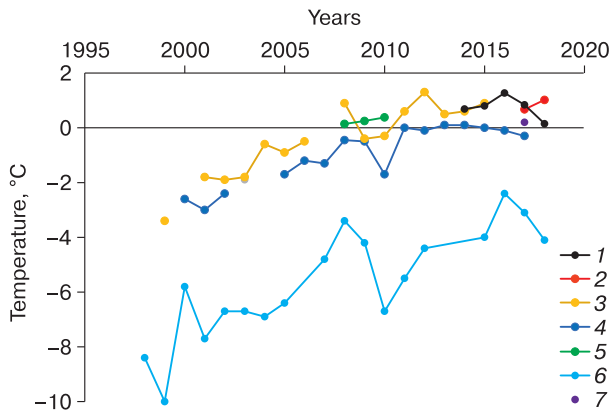


Fig. 5. Changes mean annual ground temperature of the active layer with time.

1 – Cape Bolvanskiy; 2 – Kumzha; 3 – Vorkuta; 4 – Nadym (measured at a depth of 0.85 m); 5 – Nadym (measured at a depth of 1.3 m); 6 – Marre-Sale; 7 – Tarko-Sale.

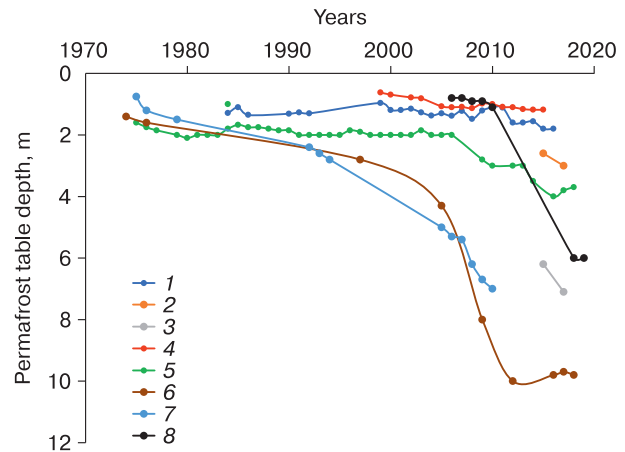


Fig. 6. Change in position of the permafrost table with time.

1 – Cape Bolvanskiy, borehole 59; 2 – Kumzha, borehole 3 Ku, the central part of the site; 3 – Kumzha, the marginal part of the site; 4 – Vorkuta; 5 – Nadym, borehole 23-75; 6 – Yuzhniy (South) Urengoy, borehole 5-01; 7 – Yuzhniy (South) Urengoy, borehole 5-08; 8 – Tarko-Sale, borehole 2 T-S.

ground temperature at a depth of 10 m was still -1.4°C . At the Yuzhniy (South) Urengoy station, permafrost degradation and positive mean annual ground temperatures of the active layer were recorded in the early 1990s, while mean annual ground temperature of permafrost at a depth of 10 m was approximately -0.7°C . Thus, degradation of the upper horizons of permafrost can start when mean annual ground temperatures at a depth of zero annual amplitudes are still relatively low.

Permafrost degradation is accompanied by lowering of its table. The results of observations are shown in Fig. 6. In the typical tundra zone, only an increase in seasonal thawing has been observed, but there is still no detachment of the permafrost table from the base of the active layer.

In the southern tundra zone, at the CALM grid of the Bolvanskiy monitoring station, the thickness of the seasonally thawed layer has increased from 1.2 m (2000) to 1.8 m (2016), which exceeds the depth of potential freezing for this area; thus, subsidence of the permafrost table has already begun. In the Kumzha area, with a thickness of the active layer of 2 to 2.5 m, the permafrost table in the central part of the grid lowered from 2.6 m (2015) to 3.0 m (2016), and in the marginal part with shrubs up to 1.5 m high – from 6.2 to 7.1 m, respectively.

In the southern tundra zone in the Vorkuta region, taking into account thaw subsidence, the permafrost table lowered by 0.6 m from 1999 to 2015 [Kaverin et al., 2017].

The greatest lowering of the permafrost table has been recorded in the forest-tundra zone in well-drained areas with high shrubs favorable for snow ac-

cumulation. In the area of borehole 5-01, the lowering of the permafrost table began in the early 1990s, accelerated in the 2000s, and reached a depth of 10 m by 2014. After 2014, the position of the permafrost table has fluctuated around a depth of approximately 10 m. At borehole 5-08, the permafrost table lowered by approximately 7 m by 2010. At the end of 2010, this borehole collapsed, and observations were terminated.

In the northern taiga zone, only bogs, linear ridges, and peat mounds are frozen. Lowering of the permafrost table in the Nadym region was observed only in bogs and by 2018 it reached about 4 m. Frozen palsas and lithalsas remain relatively stable, and no permafrost degradation has been observed here. In the Tarko-Sale monitoring station, palsas and linear peat ridges are still frozen. The permafrost table in palsas remains stable, while within ridges composed of mineral soils it has dropped to a depth of 6 m.

To determine properly the stages and mechanisms of permafrost degradation, it is very important to take into account the structure of the upper soil horizons. In the structure of the upper permafrost, the following layers are distinguished from top to bottom [Shur, 1988]: a) active layer, b) transient layer, c) intermediate layer, and d) original permafrost. A transient layer is a soil layer that belongs to the permafrost for several years and may thaw only under favorable climatic conditions [Shur, 1988]. Its thickness is small and reaches up to 10–15 % of the average thickness of the active layer in mineral soils and up to 40 % in peat. Such a layer was distinguished in 1933 by Yanovskiy, who noted its high silt content and a

slight increase in moisture content in comparison with the active layer. At present time, when significant climate warming has led to increase in the active layer thickness, we can assume that the entire former transient layer has already joined the active layer, i.e. it thaws and freezes annually.

The intermediate layer is a typical horizon in the upper part of the permafrost, which was identified and described in detail by Shur in the mid-1980s [Shur, 1988]. One of his hypotheses of formation of this layer is the re-freezing of a part of the permafrost that had thawed from the surface during the period of the climatic optimum. A characteristic feature of the intermediate layer is its extremely high ice content. The thickness of the intermediate layer can reach 2–3 m. The intermediate layer plays a protective role during climate warming that leads to increase in the depth of seasonal thawing. Thawing of the intermediate layer requires significantly greater heat input due to its high ice content and therefore its occurrence prevents thawing of the underlying permafrost. With a long-term increase in mean annual and summer air temperatures, the intermediate layer may completely thaw, and in this case accelerated degradation of underlying permafrost will begin.

A combined analysis of the data on mean annual ground temperature at the base of the active layer and in the permafrost at different depths (up to the depth of zero annual amplitudes), and the rate of lowering of the permafrost table allowed us to develop a conceptual model and distinguish three stages of permafrost degradation during climate warming (Fig. 7).

At the first stage, the depth of seasonal thawing increases, and in some especially warm years the transient layer becomes a part of the active layer. Mean annual ground temperature is still negative, and at this stage permafrost can be considered stable.

At the second stage, with the further warming of the climate, mean annual ground temperature of the active layer becomes positive, thawing of the intermediate layer begins, and after its complete thawing it loses its protective function. Soils of the active layer transform from seasonally thawed to seasonally frozen state. This stage can be considered transitional, and state of permafrost can be considered unstable.

Finally, at the third stage, the thawing of permafrost from above continues along with relatively fast lowering of the permafrost table and formation of closed talik. Positive mean annual ground temperature is observed not only in the active layer, but also in the developing closed talik. This stage is characterized by progressive permafrost degradation.

An analysis of the spatial distribution of permafrost degradation in the western sector of the Russian Arctic reveals that in the typical tundra zone mean annual ground temperatures of the permafrost and active layer remain negative, and permafrost is in a stable state.

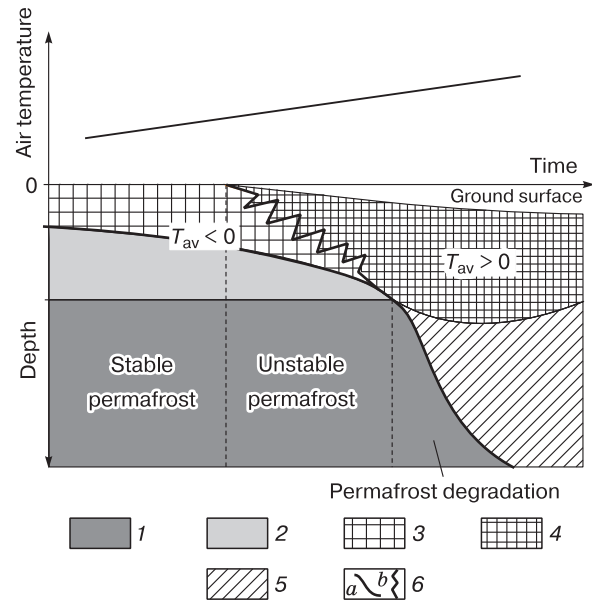


Fig. 7. Stages of permafrost reaction to climate warming:

1 – permafrost; 2 – intermediate layer; 3 – seasonally thawed layer; 4 – seasonally frozen layer; 5 – unfrozen soils area; 6 – position of the permafrost table over time (a) and the conditional boundaries of the transition from seasonal thawing to seasonal freezing (b). Line it is a linear trend in air temperature; T_{av} it is the average annual ground temperature.

In the southern tundra, mean annual ground temperature of the permafrost remains negative, but mean annual ground temperature of the active layer has become positive. Thawing of the intermediate layer has begun. Permafrost is in transitional, unstable state. In this bioclimatic zone in landscapes with high shrubs, progressive permafrost degradation may begin in the coming years.

In the zones of forest-tundra and northern taiga, mean annual ground temperature of the active layer is positive, and mean annual ground temperature of the underlying permafrost is approaching 0°C , and progressive permafrost degradation and rapid lowering of the permafrost table have been observed.

It should be mentioned that these observations can be applied only to landscapes with the greatest vulnerability to climate change. In landscapes with high resistance to climate warming, permafrost can remain in a stable or transitional state even within southern bioclimatic zones.

Observations showed that climate warming leads to increase in mean annual ground temperature of the active layer up to positive values and increase in depth of seasonal thawing, and subsequently more favorable conditions develop for growth of vegetation cover and shift of the boundaries of bioclimatic zones to the north (Fig. 8).

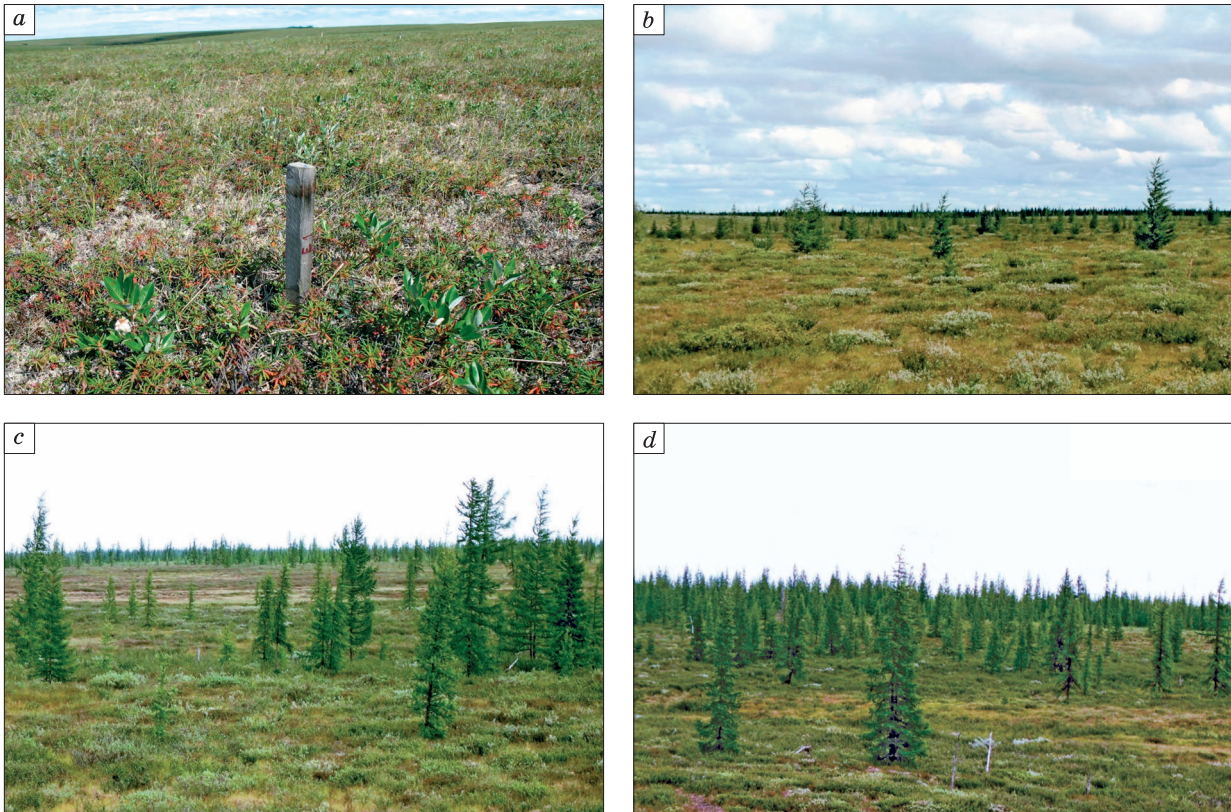


Fig. 8. Changes in vegetation in the Yuzhniy (South) Urengoy study area during climate warming.

a – 1970s; *b* – 1990s; *c* – 2000s; *d* – 2010s. Photo by D.S. Drozdov.

Migration of the tree line to the north that occurred in the area of Yuzhniy (South) Urengoy from 1975 to 2018 is estimated to reach approximately 30–40 km. Moreover, climate warming leads not only to growth of forest vegetation, but also to increase in the projective cover of shrubs and, in general, to decrease in diversity of landscape mosaic.

CONCLUSIONS

Analysis of the results of long-term monitoring of permafrost conditions at stations in the western sector of the Russian Arctic allows us to make the following conclusions:

From 1970 to 2018, mean annual air temperature in the region increased by approximately 2.8 °C, which is close to the worst-case scenario of climate change. Climate warming is accompanied by 5–10 % increase in annual precipitation and increase in snow cover thickness in the tundra zone at a rate of 1.8 cm/year (1998–2018), and in the forest tundra and northern taiga zone at a rate of 0.6 cm/year (2003–2018).

In all bioclimatic zones and in all dominant landscapes an increase in mean annual ground temperature of permafrost has been observed along with

warming climate. The greatest changes in mean annual ground temperature have been observed in the typical tundra zone. The average temperature increase here has reached 0.056 °C/year. In the southern tundra and forest-tundra zones, the rate of increase in mean annual ground temperature of permafrost has varied from 0.04 to 0.05 °C/year, and in the zone of the northern taiga it has reached 0.035 °C/year.

Since 2007, in all bioclimatic zones, except for the typical tundra, mean annual ground temperature of the active layer has reached positive values, and thawing of permafrost from above has begun (i.e., permafrost degradation). At the same time, degradation processes have not developed in all landscapes, but only within landscapes that are most sensitive to climatic changes.

Thawing of permafrost from above is accompanied by lowering of the permafrost table. In the forest-tundra zone, it already started in the mid-1990s and in well-drained areas it has reached a depth of 7 to 10 m. In the southern tundra zone, the maximum lowering of the permafrost table has reached 7 m in well-drained ice-poor sandy soils with a well-developed shrub vegetation. In other cases, lowering of the

permafrost table has not exceeded 2 m. In the northern taiga zone, permafrost table has lowered by 4 to 6 m.

We propose to distinguish three stages of permafrost degradation caused by climate warming. At the first stage, the depth of seasonal thawing increases, and mean annual ground temperature rises. At this stage, mean annual ground temperature is still negative, and permafrost can be considered stable. At the second stage, the depth of seasonal thawing exceeds the thickness of the transient layer and affects the intermediate layer. Values of mean annual ground temperature in the upper horizons become positive. Thawing of the intermediate layer and lowering of the permafrost table begins. This stage is characterized by unstable state of permafrost. If mean annual ground temperature in the upper horizons becomes positive, and a thickness of the thawed layer becomes greater than a combined thickness of the active and intermediate layers, the stage of active permafrost degradation, which is accompanied by fast lowering of the permafrost table, begins.

Permafrost degradation, along with climate warming, is favorable for the active growth of vegetation and a shift of boundaries of bioclimatic zones to the north.

Monitoring of the thermal regime of permafrost has been performed within the framework of the state task, according to the Research Plan of the Tyumen Scientific Center of the SB RAS for 2018–2020, protocol No. 2 of 08.12.2017. Analysis and interpretation of conditions and rates of permafrost degradation have been performed with the support of the Russian Foundation for Basic Research (RFBR) grant 18-05-60004; studies of the impact of climate change on vegetation have been supported by the RFBR grant 18-55-11005. Field work at monitoring sites in the European North and West Siberia in 2016–2019 were performed with the financial support of the grant of the Russian Science Foundation 16-17-00102.

References

- AMAP, 2011. Snow, Water, Ice and Permafrost in the Arctic (SWIPA). Arctic Monitoring and Assessment Programme (AMAP), Oslo, Norway, 15 pp.
- Anisimov, O.A., Belolutskaia, M.A., Lobanov, V.A., 2003. Contemporary changes of climate and environment in the high latitudes of North Hemisphere. *Meteorologiya i Gidrologiya (Meteorology and Hydrology)*, No. 1, 18–30 (in Russian).
- Baulin, V.V., Murzaeva, V.E. (Eds.), 2003. *Geocryological Glossary*. GEOS, Moscow, 140 pp. (in Russian).
- Biskaborn, B.K., Lanckman, J.-P., Lantuit, H., et al., 2015. The new database of the Global Terrestrial Network for Permafrost (GTN-P). *Earth Syst. Sci. Data*, No. 67, 245–259, DOI:10.5194/essd-7-245-2015.
- Biskaborn, B.K., Smith, S.L., Noetz, L.J., et al., 2019. Permafrost is warming at aglobal scale. *Nature Communications*, No. 10, p. 264, DOI: 10.1038/s41467-018-08240-4.
- Boike, J., Nitzbon, J., Anders, K., et al., 2018. A 16-year record (2002–2017) of permafrost, active layer, and meteorological conditions at the Samoylov Island Arctic permafrost research site, Lena River Delta, northern Siberia: an opportunity to validate remote sensing data and land surface, snow, and permafrost models. *Earth Syst. Sci. Data Discuss.*, No. 11, 261–299, DOI: 10.5194/essd-2018-82.
- Brown, J., Hinkel, K.M., Nelson, F.E., 2000. The Circumpolar Active Layer Monitoring (CALM) program: research designs and initial results. *Polar Geogr.* 24 (3), 166–258.
- Burn, C.R., 2004. The thermal regime of cryosols. In: J. Kimble (Ed.). *Cryosols (Permafrost-Affected Soils)*. Springer-Verlag, Berlin, Heidelberg, New York, pp. 391–414.
- Drozdo, D.S., Malkova, G.V., Ukraintseva, N.G., Korostele, Yu.V., 2012. Permafrost monitoring of southern tundra landscapes in the Russian European North and West Siberia. In: Tenth International Conference on Permafrost. The Northern Publisher, Salekhard, vol. 2, pp. 65–70.
- Grechishchev, S.E., Melnikov, E.S., 1989. Methodical Recommendations on Hydrogeological and Geocryological Study of the Upper Horizons of Grounds under Regional and Prospecting Works for Oil and Gas in the Cryolithozone. VSEGINGEO, Moscow, 108 pp. (in Russian).
- Hinzman, L.D., Bettez, N.D., Bolton, W.R., et al., 2005. Evidence and implications of recent climate change in northern Alaska and other arctic regions. *Climatic Change* 72 (3), 251–298.
- IPCC, 2013. *Climate Change 2013. The Physical Science Basis*. In: Contribution of Working Group I to the Fifth Assessment Report of the Intergovernmental Panel on Climate Change. T.F. Stocker et al. (Eds.). Cambridge University Press, Cambridge, 1535 pp.
- Kaverin, D.A., Pastukhov, A.V., Novakovskiy, A.B., 2017. Active layer thickness dynamics in the tundra permafrost-affected soils: a calm site study, the European North of Russia. *Earth's Cryosphere XXI* (6), 30–38.
- Linderholm, H.W., Nicolle, M., Francus, M., et al., 2018. Arctic hydroclimate variability during the last 2000 years: current understanding and research challenges. *Clim. Past*, vol. 14, 473–514, DOI: 10.5194/cp-14-473-2018.
- Malkova, G.V., Korostele, Yu.V., Sadurtdinov, M.R., et al., 2018. Contemporary climate change and thermal regime of permafrost at European North. In: Reports of the Scientific Council session on Cryology of the Earth, Russian Academy of Sciences, “Actual problems of Geocryology” (Moscow, 15–16 May, 2018). Moscow University Press, Moscow, vol. 1, pp. 98–104 (in Russian).
- Mazhitova, G., Ananjeva-Malkova, G., Chestnykh, O., Zamolodchikov, D., 2004. Active layer spatial and temporal variability at European Russian Circumpolar Active Layer Monitoring (CALM) sites. *Permafrost and Periglacial Processes* 15 (2), 123–139.
- Melnikov, V.P., Skvortsov, A.G., Malkova, G.V., et al., 2010. Seismic studies of frozen ground in Arctic areas. *Russian Geology and Geophysics* 51 (1), 136–142, DOI: 10.1016/j.rgg.2009.12.011.
- Nelson, F.E., Anisimov, O.A., Shiklomanov, N.I., 2001. Subsidence risk from thawing permafrost. *Nature* 410, 889–890.
- Nicolsky, D.J., Romanovsky, V.E., 2018. Modeling long-term permafrost degradation. *J. Geophys. Res.: Earth Surface*, vol. 123, DOI: 10.1029/2018JF004655.
- Oberman, N.G., 2008. Contemporary permafrost degradation of the European north of Russia. In: Proc. of the Ninth International Conference on Permafrost (Fairbanks, Alaska, June 29–July 3, 2008). Fairbanks, 2008, vol. 2, pp. 1305–1310.

- Osterkamp, T.E., Romanovsky, V.E., 1999. Evidence for warming and thawing of discontinuous permafrost in Alaska. *Permafrost and Periglacial Processes* 10 (1), 17–37.
- Paffengolz, K.N., Borovikov, L.I., Jamoyda, A.I., et al. (Eds.), 1973. *Geological Glossary*. Nedra, Moscow, vol. 1: A–M, 487 pp. (in Russian).
- Pavlov, A.V., 1997. Permafrost-climate monitoring of Russia: methodology, results, prediction. *Kriosfera Zemli (Earth's Cryosphere)* II (1), 47–58.
- Pavlov, A.V., Malkova, G.V., 2005. Contemporary Climate Changes on the North of Russia. Academic Publishing House “Geo”, Novosibirsk, 80 pp. (in Russian).
- Prik, Z.M., 1971. Climatic zoning of Arctic. In: *Bulletin of Arctic and Antarctic Research Institute*. Leningrad, vol. 304, pp. 72–84 (in Russian).
- Romanovsky, V.E., 2006. Thermal regime of permafrost in Alaska during the last 20 years. In: *Proc. of the International Conference “Theory and practice of assessment of the Earth Cryosphere and forecast of its changes”*. Tyumen State University, Tyumen, vol. 1, pp. 96–101 (in Russian).
- Romanovsky, V., Drozdov, D., Oberman, N., et al., 2010. Thermal state of permafrost in Russia. *Permafrost Periglacial Processes* 21 (2), 136–155.
- Romanovsky, V.E., Kholodov, A.L., Marchenko, S.S., et al., 2008. Thermal state and fate of permafrost in Russia: first results of IPY. In: *Proc. of the Ninth International Conference on Permafrost* (Fairbanks, Alaska, June 29–July 3, 2008). Fairbanks, 2008, vol. 2, pp. 1511–1518.
- Sadurtdinov, M.R., Skvortsov, A.G., Tsarev, A.M., et al., 2018. Experience in the application of wave methods of Geophysics in the Permafrost Area. In: *Proc. of the International Geological and Geophysical Conference “Geo Europe. Modern methods of exploration and development of mineral resources in Eurasia”*. LLC “PolyPress”, Tver, pp. 675–679 (in Russian).
- Shur, Yu.L., 1988. Upper Horizon of Permafrost and Thermokarst. Nauka, Novosibirsk, 213 pp. (in Russian).
- Shur, Yu.L., Jorgenson, M.T., 2007. Patterns of permafrost formation and degradation in relation to climate and ecosystems. *Permafrost and Periglacial Processes* 18 (1), 7–19.
- Smith, S., Romanovsky, V., Lewkowicz, A., et al., 2010. Thermal state of permafrost in North America: a contribution to the International Polar Year. *Permafrost and Periglacial Processes* 21 (2), 117–135.
- Streletskiy, D., Anisimov, O., Vasiliev, A., 2015a. Permafrost degradation. In: *Snow and Ice-Related Hazards, Risks and Disasters*. Elsevier, New York, pp. 303–344, DOI: 10.1016/B978-0-12-394849-6.00010-X.
- Streletskiy, D.A., Sherstiukov, A.B., Frauenfeld, O.W., Nelson, F.E., 2015b. Changes in the 1963–2013 shallow ground thermal regime in Russian permafrost regions. *Environ. Res. Lett.*, vol. 10, 125005.
- Vasiliev, A.A., Drozdov, D.S., Moskalenko, N.G., 2008. Permafrost temperature dynamics of Western Siberia in context of climate change. *Kriosfera Zemli (Earth's Cryosphere)* XII (2), 10–18.
- Vasil'chuk, A.C., Vasil'chuk, Yu.K., 2015a. Engineering-geological and geochemical conditions of Belyi Island (Kara Sea). *Inzhenernaya Geologiya (Engineering Geology)*, No. 1, 50–65.
- Vasil'chuk, A.C., Vasil'chuk, Yu.K., 2015b. Engineering-geological and geochemical conditions of the Tambey river mouth (North of the Yamal peninsula). *Inzhenernaya Geologiya (Engineering Geology)*, No. 4, 36–54.
- Walker, D.A., Raynolds, M.K., Daniëls, F.J.A., et al., 2009. The Circumpolar Arctic Vegetation Map. *J. Veget. Sci.* 16 (3), 267–282.
- URL: <https://www.rp5.ru/> (last visited: 01.09.2019).
- URL: <http://www.meteo.ru/data> (last visited: 01.09.2019).

Received May 21, 2019

Revised version received October 7, 2019

Accepted October 15, 2019

CRYOGENIC PHENOMENA IN SEAS AND OCEANS

DOI: 10.21782/EC2541-9994-2020-2(27-33)

ON THE RELATIONSHIP BETWEEN SEA ICE EXTENT DYNAMICS
IN THE NORTHERN HEMISPHERE AND TOTAL ATMOSPHERIC OZONE

V.M. Fedorov, D.M. Frolov

*Lomonosov Moscow State University, Faculty of Geography,
1, Leninskie Gory, Moscow, 119991, Russia; fedorov.msu@mail.ru*

The sea ice extent dynamics in the Northern Hemisphere and variations of solar irradiance at different altitudes of polar regions are considered as possible controls of total ozone variations in the atmosphere. It has been determined that annual variation of total ozone content (TOC) closely correlates with the annual course and multiyear variations of sea ice extent in the Northern Hemisphere. We used a regression model for forecasting total ozone content up to 2050. It has been revealed that the model concept of total column ozone (TCO) should take into account the Earth's cryosphere effect (cryospheric factor) on variations in total atmospheric ozone. The cryospheric factor includes changes in sea ice extent in the Northern Hemisphere and insolation variations at different altitudes in the polar regions.

Total ozone, sea ice extent, planetary albedo, insolation, insolation contrast, correlation, regression model, forecasting

INTRODUCTION

Due to significance of the ozone layer (acting as a shield to protect Earth's surface from excessive ultraviolet (UV) radiation) to ensure life on Earth (including human), the total atmospheric ozone content (TOC) and its controls is one of the issues of major importance in the Earth Sciences. This provides a substantiation of the topicality of the research into total atmospheric ozone, its spatial and temporal variability.

The TOC studies include two main research directions. The first one is the analysis and advancement of ideas about photochemical reactions leading to production and destruction of ozone (photochemical theory). This research direction is heavily underlain by Chapman's fundamental model (a schematic for photochemical reactions) [Chapman, 1930], which principally explains the existence of high-concentration layers of ozone and atomic oxygen in the atmosphere. The second direction focuses on the dynamic aspect [Perov, Khrgian, 1980] and includes ideas about atmospheric circulation processes (vortices) and vertical air flows, providing vertical and horizontal transport of ozone between source and sink regions. Our research views the Earth's cryosphere as another element (the third research direction) in the concept of TOC model aiming at studying the seasonal and interannual sea ice extent dynamics largely governed by the change in planetary albedo and water vapor content in polar regions, with particular focus on changes in solar radiation inci-

dence with elevation in polar regions. This paper aims to study the relationships between insolation-affected sea ice extent and TOC at different time scales (annual dynamics, multiyear variability). Variations in albedo correlate with changes in the amount of solar radiation reflected by sea ice into the atmosphere (specifically, 60–90 % by the snow-ice surface and less than 10 % by water surface). Water vapor contents are affected by variations in scattered radiation and concentrations of HO₂ and OH radicals, which contribute to ozone breakup [Hunt, 1966]. In addition, changes in sea ice extent may be associated with a good solubility of ozone in water and are thereby involved in the TOC dynamics. As such, this "ice element" is shown to be one of major players in the generalized TOC model because of the maximum TOC values localized in polar regions of the Earth, where the maximum TOC variability (i.e. annual and multiyear variations) is accordingly observed [Perov, Khrgian, 1980]. This potential TOC predictor has thus far been totally ignored, though.

Traditionally, ozone is believed to be produced mainly in the equatorial region as a result of photochemical reactions and transported to the polar regions by air masses [Perov, Khrgian, 1980]. However, principal features of the solar radiation (insolation) reaching polar regions and production capacity of atmospheric and stratospheric ozone over the poles still remain understudied. Given that during the summer season, polar regions receive more solar radiation

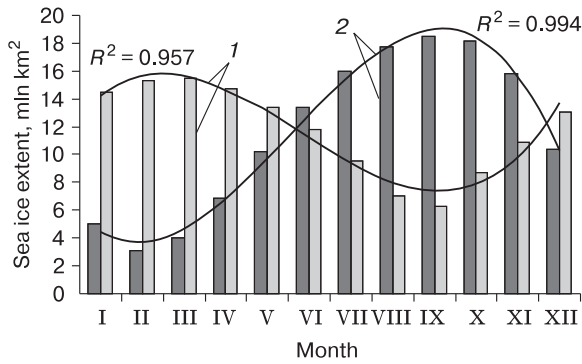


Fig. 1. Seasonal variations in sea ice extent in the Northern (1) and Southern (2) Hemispheres.

than tropical region (because of the polar day) this period provides at least equal opportunities for ozone production in equatorial region and in polar regions.

The authors' calculations of insolation in different altitude levels [Fedorov, Kostin, 2019] show that, e.g. at an altitude of 25 km (an ellipsoid with each point located 25 km above the normal relative to a reference ellipsoid that best approximates the Earth's

overall shape) the polar night lasts four months (8–11th astronomical months) in the 84.5–90° latitude range. While in the 84.5–79.5° latitudinal range it lasts two months (9–10th astronomical months), this phenomenon does not occur south of latitude 74.5°. This suggests solar radiation incident for the full year round there and, therefore, a possibility for ozone production. As such, these latitudinal boundaries delimit the surface at 30 km altitude. At an altitude of 35 km, the latitude range of permanent illumination increases by 1° of latitude (75.5°). From a 40 km altitude, the latitude limit of the two-month polar night rises to 84.5° (at an altitude of 25 km, it is located at latitude 79.5°). At altitudes of 45 and 50 km, the latitudinal limit of permanent illumination “builds up” another 1° of latitude (76.5°). As such, the altitude-dependent increase in the latitudinal range of illumination should be taken into account when evaluating a possibility of ozone production in polar regions.

Ice covers about 6 % (ca. 30 million km²) of the Earth's surface, which is for the most part localized in the Arctic and Antarctic. In the Northern Hemisphere, land ice accounts for only 20 % of the total area of Arctic glaciation, while sea ice for the rest of 80 % [Koryakin, 1988]. Seasonal variations in land

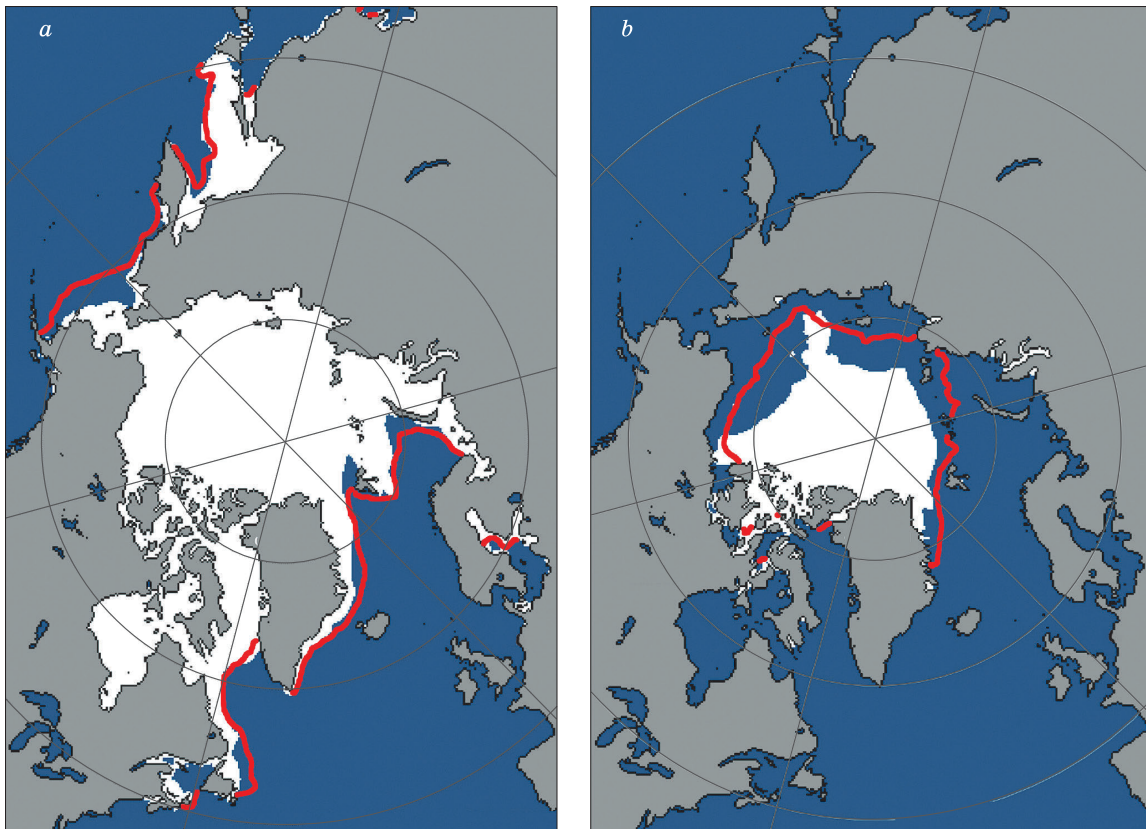


Fig. 2. Changes in sea ice extent in the Northern Hemisphere:

a – March (maximum); *b* – September (minimum). The red line shows the average boundary of sea ice extent in March and November in the period 1981–2010 [Fetterer et al., 2012; http://nsidc.org/data/seaice_index/].

and sea glaciation affect the area of 6.3–15.4 million km² in the Arctic ocean (Fig. 1) and from 3.0 to 18.5 million km² in Antarctica. The amplitude of average seasonal cycle of sea ice area is 9.15 million km² in the Northern Hemisphere, and 15.46 million km² in the Southern Hemisphere [Fetterer *et al.*, 2017; <http://nsidc.org>]. Seasonal variations in sea ice extent from maximum to minimum (i.e. the amplitude of average seasonal cycle) were estimated (in percentage) for the Northern (59.2 %) and Southern (81.4 %) Hemispheres.

Sea ice cover is a product of interactions between the ocean and the atmosphere under certain temperature conditions [Frolov, Gavrilov, 1997; Zubakin, 2006]. The most important parameter is its extent, or the area it occupies. Among the changes this area is subjected to over time, the most pronounced are interpreted as seasonal, interannual and multi-year variations. In the Northern Hemisphere, summer minimum of the sea ice area is chronologically distinctly localized in the annual cycle and falls on September (the autumnal equinox, the end of summer half-year in the Northern Hemisphere) (Fig. 2).

The maximum area is more extended in time and is observed from February through April (the period around vernal equinox, the end of winter and beginning of summer half year in the Northern Hemisphere) [Frolov, Gavrilov, 1997]. Accordingly, ultimate sea ice extent values are characterized by ca. 90° phase lag (of three months) in the annual solar irradiance cycle relative to ultimate values of arriving solar radiation.

RESULTS AND DISCUSSION

The relationships between TOC values and sea ice extent (SIE) in the Northern hemisphere were analyzed with respect to annual variation cycles and time-series of multiyear variability. The input data for

seasonal TOC variations were combined with the SBUV satellite database (Version 8.6) Merged Ozone Data Set (MOD) 1970–2017 Profile and Total Column Ozone from the SBUV Instrument Series [https://acd-ext.gsfc.nasa.gov/Data_services/merged/]. These data include TOC values with a monthly resolution and in 5° increments of latitude spanning the period since 1970 to the present.

The applied herewith measures of TOC are related to the concept of the total column ozone (TCO) and use units of length (centimeters, millimeters, and micrometers). The total column ozone implies total ozone content in a vertical air column conceptualized by suggesting that all of the overhead ozone molecules (spread over the stratosphere thickness) could be brought down to form a “layer” at standard conditions (pressure $p = 1013$ mbar, temperature $T = 273.16$ K). Thus, the units used as measures of the ozone column base (“thickness”) are as follows: atmosphere-centimeters (atm-cm) and milliatmospheric centimeters (matm-cm), which alternatively are termed Dobson Units (DU) [Perov, Khrgian, 1980]. According to the Mid-Latitude Ozone Model [Krueger, Minzner, 1976], the “thickness “ of TCO layer is 0.345 atm-cm (or 345 DU). This value is equivalent to ozone concentration in $7.39 \cdot 10^{-3}$ kg, or $9.27 \cdot 10^{22}$ molecules contained in a column of air with a 1 m² cross-sectional area (i.e. for every square meter of area at the base of the column) [Perov, Khrgian, 1980]. In this work, we use Dobson Units (DU) for the atmospheric TOC analysis. The initial data on the sea ice extent were derived from satellite observations available on the US National data center website [<http://nsidc.org>].

Annual TOC variation cycle

The annual TOC variations cycle (“annual course”) is characterized by the antiphase change in the hemispheres (Fig. 3).

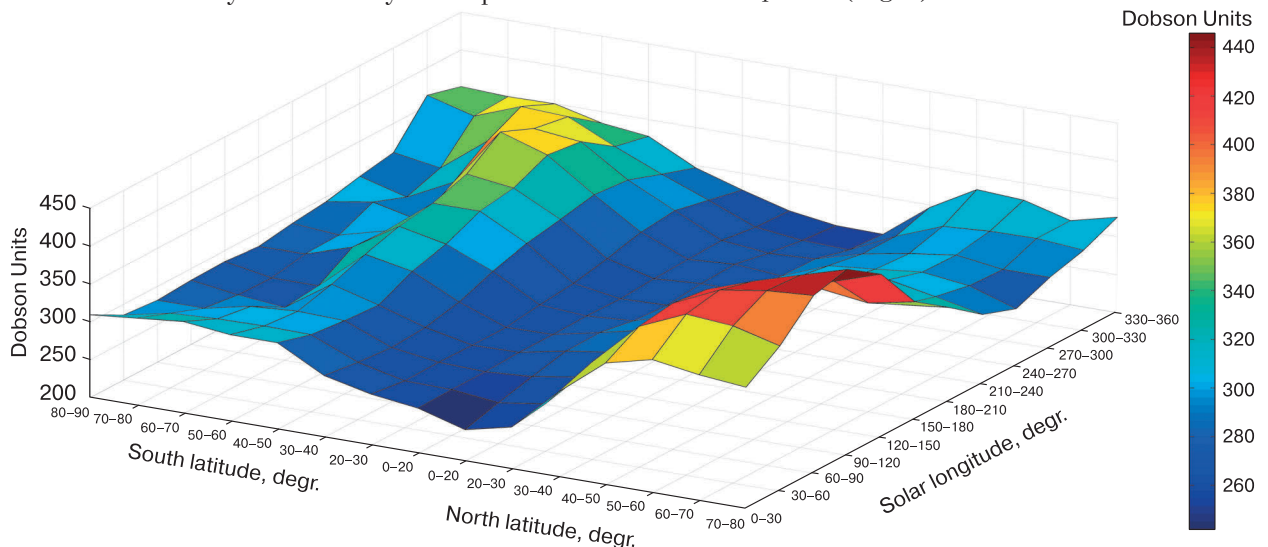


Fig. 3. Planetary total ozone distribution and its changes with seasons and latitudes.

In the Northern Hemisphere, the maximum TOC values are reported in April, and minimum in October, whereas in the Southern Hemisphere, vice versa, the minima in TOC values are attributable to April, and maxima to October. That same antiphase dynamics is observed in the annual SIE retreat/advance cycles in the hemispheres. In the Northern Hemisphere, SIE values peak in March, and are the lowest in September (in the Southern Hemisphere, contrarywise). Thus, the TOC maxima and minima are immediately followed by SIE maxima and minima. The effect is offset by lag of about a month. The shift by a month ahead in annual TOC variations (if its annual variation cycle is synchronized with the SIE annual dynamics) the coefficient of correlation between the time-series equals 0.974 (with probability of 0.99) (Fig. 4). The statistical significance of the linear correlation coefficient was evaluated from the correlation analysis according to the existing evaluation criteria and methods [Tsybalenko *et al.*, 2007].

The annual TOC variation cycle for the Earth is determined by annual cycle of TOC variations in the Northern Hemisphere (and its anti-phase in the Southern Hemisphere, accordingly). This owes to greater TOC values for the Northern Hemisphere against the Southern Hemisphere. The mean monthly TOC values are 325.26 DU for the Northern Hemisphere and 302.95 DU for the Southern Hemisphere [Perov, Khrgian, 1980]. If compared, these are expressed as percentage showing that mean monthly TOC values the Northern Hemisphere are ca. 7 % less than those for Northern Hemisphere. Interestingly, during winter half year in the two hemispheres, the Northern Hemisphere receives about 7 % more solar radiation than the Southern Hemisphere [Fedorov, 2018]. This phenomenon accounts for the fact that during winter half year in the Northern Hemisphere, the Earth reaches perihelion, while it reaches aphelion in winter half year in the Southern Hemisphere. In summer half year, the effect is therefore seen to be

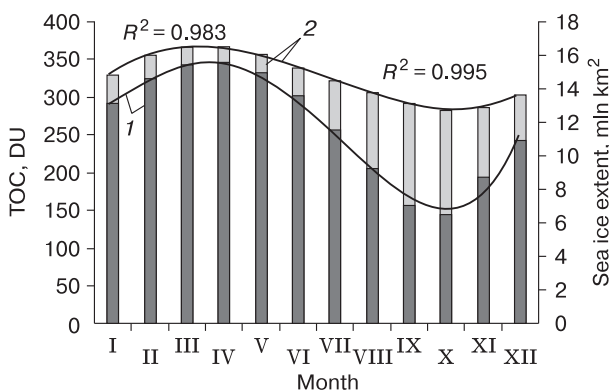


Fig. 4. Seasonal variation cycle of sea ice extent in the Northern Hemisphere (1) and TOC (2).

TOC time-series is one month phase-shifted (advanced).

opposite (i.e. roughly 6 months apart). Given that during the winter half year in the two hemispheres, Northern Hemisphere receives more solar radiation versus Southern Hemisphere, the former sees more reflected and scattered radiation due to the maximum sea ice extent at this time of year. This may also be one of the reasons for asymmetry in the TOC distributions across the hemispheres.

Hemispheric asymmetry in total ozone distribution can be dealt with by the dynamic approach, which constitutes the dynamic element of the TOC model, to study the global atmospheric circulation pattern in the hemispheres and specific characteristics of the insolation because of elliptical orbit of the Earth and ozone production in winter months at high altitudes in the polar regions. The TOC models are a whole family of models, and each presents parameterization of dynamic factors and photochemical processes in a different way. Meridional ozone transport in the Northern Hemisphere occurs both by regular transport in the global atmospheric circulation (GAC) with its constituent wind cells – Hadley Cells, Ferrell Cells, Polar Cells, and vortexes (tropical and extratropical cyclones) [Perov, Khrgian, 1980; Fedorov, 2018]. Due to the greater heterogeneity of the underlying surface in the Northern Hemisphere, meridional ozone transport is carried out there by tropical and extratropical cyclones (to a far greater extent than in the relatively homogeneous Southern Hemisphere). In addition, as it was shown previously [Fedorov, 2018], an increase in the meridional transport intensity (meridional insolation gradient) is observed in winter half year in the Polar Cells, while it decreases in summer half year. An increase in the annual meridional insolation gradient (heat transfer) is observed in the areas of localization of the Hadley and Ferrell circulation cells. The ratio of land to ocean area is important as descriptor of the heterogeneity of the underlying surface in the hemispheres. The proportions of land/ocean areas are: 39.3 % and 60.7 % in the Northern Hemisphere and 19.1 % and 80.9 % in the Southern Hemisphere, respectively [Istoshin, 1956]. Thus, the annual number of tropical cyclones in the Northern Hemisphere (North Atlantic and North-Western Pacific) totals to about 60 on average, and considerably less (6–8) in the Southern Hemisphere [http://meteoinfo.ru]. In the Southern Hemisphere, the meridional ozone transport is blocked due to the strong Roaring Forties west-east transport, whose existence is associated with the uniformity of the hemisphere and a high meridional temperature gradient (much higher than the meridional temperature gradient in the Northern Hemisphere). Specifically, these natural controls, which weaken the meridional ozone transport effect in the Southern Hemisphere, are likely to determine the TOC values asymmetry for the two hemispheres.

The physical mechanism of the maximum and minimum TOC distribution can be qualitatively represented as follows. Since the beginning of the vernal equinox (March–April), the illuminated area in the Northern Hemisphere extends north of the Arctic circle (66.6°). While the solar declination is small, and is associated with large amount of the scattered radiation. At this, sea ice extent approaches its maximum, thereby increasing the reflected radiation. These components of the incoming radiation are likely to determine both production and peaks in TOC in the Northern Hemisphere (which also occurs in the Southern Hemisphere after the onset of autumnal equinox in the Northern Hemisphere). The time of approaching autumnal equinox is marked by a small solar declination in the Northern Hemisphere; lowest the sea ice spread; and minimal reflected radiation, which probably determines the minimum TOC values (the Southern Hemisphere sees the same situation with the onset of spring in the Northern Hemisphere). In addition, the atmospheric circulation polar cells show an increase in intensity in winter half year [Fedorov, 2018], which means that the maximum observed after the vernal equinox may also be associated with this dynamic factor.

Mutiyear variations in TOC

The authors compared the multiyear changes in the average annual TOC values obtained from the observations over the period 1936–2016 at Arosa station (Switzerland) [https://www.woudc.org/], with the SIE values derived from the reconstructions for the period from 1936 to 2006 [Walsh, Chapman, 2001] and using a regression model from 2007 to 2016 [Fedorov, 2015a; Fedorov, Grebennikov, 2018]. This time-series of TOC measurements is the longest [Bronnimann et al., 2000; Visheratin, 2007; Staehelin et al., 2018].

Implementation of the cryosphere modulus (sea ice extent in the Northern Hemisphere) in our studies of multiyear variations in the atmospheric TOC is determined by the reasons discussed above. Firstly, the annual TOC variation cycle in the atmosphere is determined by the annual TOC variations in the atmosphere of the Northern Hemisphere. Secondly, there are no long series of observations of sea ice area in the Southern Hemisphere (except relatively short satellite observation series since 1978). Results of the comparison showed a close correlation between the series of multiyear TOC variations and multiyear SIE dynamics in the Northern Hemisphere. The correlation coefficient (R) for multiyear TOC variations and multiyear average annual SIE in the Northern Hemisphere is 0.671. A relationship between multiyear TOC variations with the minimum sea ice extent is characterized by the value $R = 0.642$. The ties with the maximum values for sea ice extent dynamics are slightly weaker ($R = 0.558$). All R values are statistically significant with a probability (p -value) of 0.99.

When smoothing the TOC and SIE time-series and using the method of five-year smoothed moving averages, the R values accordingly become equal to 0.899, 0.859, and 0.857 (Fig. 5).

Previously, the authors calculated the solar radiation that arrives at the top (upper boundary) of the atmosphere with a large spatial and temporal resolution [Fedorov, 2015b, 2019; Fedorov, Frolov, 2019]. The calculations of the incoming solar radiation were performed using the data obtained from high-precision astronomical ephemerides [Giorgini et al., 1996; http://ssd.jpl.nasa.gov] for the entire Earth's surface (no atmosphere) within the interval from 3000 BC to 2999 AD. The input astronomical data for calculating insolation were the declination and ecliptic longitude of the Sun, the distance from the Earth to the Sun, and difference between the course of uniformly running (coordinate time, CT) and the universal corrected time (universal time, UT). The surface of the Earth was approximated by ellipsoid (GRS80–Geodetic Reference System 1980) with semi-axis lengths 6,378,137 m (big one) and 6,356,752 m (small one). The calculation algorithm can be generally represented by the expression

$$I_{nm}(\varphi_1, \varphi_2) = \int_{t_1}^{t_2} \left(\int_{\varphi_1}^{\varphi_2} \sigma(H, \varphi) \left(\int_{-\pi}^{\pi} \Lambda(H, t, \varphi, \alpha) d\alpha \right) d\varphi \right) dt,$$

where I is the incoming solar radiation for the elementary n -th fragment of the m -th of the tropical year, J ; σ is the square multiplier, m^2 , which enables calculation of the square differential $\sigma(H, \varphi)$; $d\alpha d\varphi$ is the square of infinitely small trapezoid ellipsoid cells; α is horary angle, rad unit; φ is geographical latitude, rad unit; H is the height of the ellipsoid surface relative to Earth surface, m; $\Lambda(H, t, \varphi, \alpha)$ is insolation at the stated moment at the stated ellipsoid surface point, W/m^2 ; t is time, s. The integration steps were: longitude 1° , latitude 1° , defined as one three hundred sixtieth ($1/360$) of the length of tropical year [Fedorov, 2013]. The value of solar constant (average multiyear TSI value (total solar irradiance)) was taken to be $1361 W/m^2$ [Kopp, Lean, 2011]. Changes in the solar activity were not taken into consideration [Fedorov, 2015b, 2019; Fedorov, Kostin, 2019; Fedorov, Frolov, 2019].

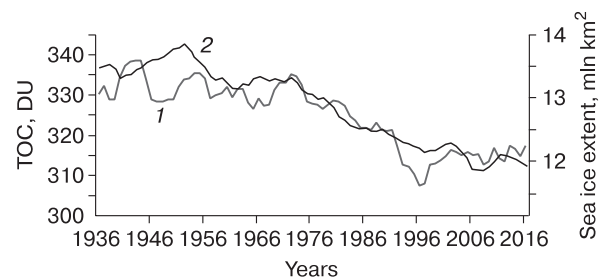


Fig. 5. The five-year-period smoothed moving averages of TOC time-series (1) and average annual sea ice extent in the Northern Hemisphere (2).

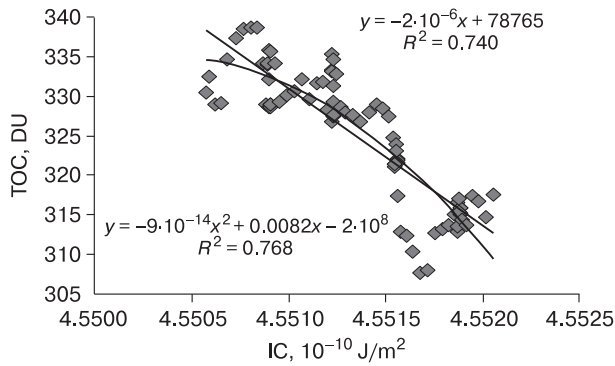


Fig. 6. Graphs of linear and polynomial (second-degree) regressions for IC and TOC and equations.

A close relationship was revealed between multiyear changes in the insolation (irradiance) contrast (IC) and multiyear variations in sea ice extent in the Northern hemisphere [Fedorov, 2015a; Fedorov, Grebennikov, 2018]. The authors interpret IC as the difference between annual insolation of the heat source area (0–45° latitude) and heat sink area (45–90° latitude) in the two hemispheres. IC (for heat source and sink areas) generally reflects changes in the meridional gradient of insolation, which controls meridional heat transfer in the ocean–atmosphere system [Fedorov, 2018, 2019]. In the regression equations, multiyear changes in IC explain 76 % of the multiyear variability of the average annual and minimum SIE in the Northern Hemisphere [Fedorov, Grebennikov, 2018]. A relationship between TOC and IC time-series is characterized by the value $R = -0.657$ (with a probability of 0.99), while the smoothed (for five-year moving averages) TOC time-series – by the value $R = -0.860$. The IC is extrapolated by the authors onto the future, allow to perform an estimated forecast of smoothed TOC values (trends) based on a regression model. Graphs of the linear and polynomial (second-degree polynomial) regression equation are shown in Fig. 6. The coefficient of determination (R^2) shows the proportion of multiyear variability of TOC, which is taken into account by the regression model (IC).

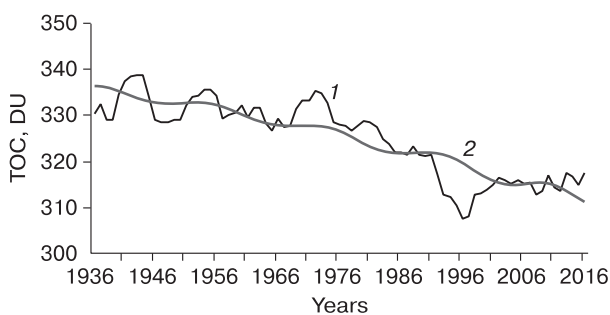


Fig. 7. Measured (1) and calculated from ensemble (2) TOC values.

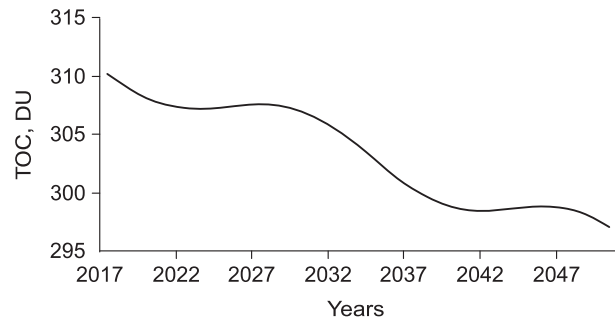


Fig. 8. Forecast estimations of TOC variations calculated based on the ensemble of linear and polynomial (second-degree) regression model.

TOC calculations were performed using linear and polynomial regression equations. In these equations, a 74.0 % and 76.8 % change in TOC is determined by a variation in IC. The average regression model based on an ensemble of linear and polynomial solutions revealed that as much as 76.1 % of the multiyear variability of TOC is determined by multiyear changes in the IC (or the average annual and minimum SIE) (Fig. 7).

The estimated forecast is calculated for the TOC values smoothed over a five-year moving averages (TOC trends). According to the calculations, the TOC in 2050 will be 297 DU (Fig. 8). The reduction in total ozone will be 14 DU, against the values as of 2016. Thus, the TOC reduction in 2050 relative to 2016 will be 4.5 %. The probable reasons for atmospheric ozone reduction are: reduction in the sea ice extent (primarily in the Northern Hemisphere) and affiliated decrease in the planetary albedo; and a marked decrease in the amount of solar radiation reaching the polar regions [Fedorov, 2015b, 2018].

CONCLUSION

The sea ice extent dynamics and insolation interpreted to be as factors of seasonal and multiyear TOC variations are considered. Characteristic features of spatial and temporal sea ice extent dynamics, insolation and TOC variations are revealed. It was determined that the annual and multiyear TOC variations are closely related to annual and multiyear variations in sea ice extent in the Northern Hemisphere (correlation coefficient is 0.974 for the annual variation cycle and from 0.857 to 0.899 for multiyear variations). The annual sea ice extent dynamics is strongly correlated with the annual dynamics of insolation, while multiyear sea ice extent variations – with multiyear IC variations [Fedorov, 2015a]. Based on the calculated IC values, smoothed TOC values enabled estimation of the forecast values for the period up to 2050. It is shown that in the model conceptualization

of TOC, next to the photochemical reactions and dynamic (variations) modules, the Earth's cryosphere should be considered as a factor affecting TOC variations, which also implicated in the sea ice extent dynamics in the Northern Hemisphere and altitude-specific changes in insolation in the polar regions.

The work was carried out within the state-commissioned budget theme "Geoecological analysis and forecast of the permafrost dynamics in the Russian Arctic" (AAAA-A16-116032810055-0) and "Mapping, modeling and risk evaluation of natural hazards" (AAAA-A16-116032810093-2).

References

- Bronnimann, S., Luterbacher, J., Schmutz, C., Wanner, H., 2000. Variability of total ozone Arosa, Switzerland, since 1931 related to atmospheric circulation indices. *Geophys. Res. Lett.* 27 (15), 2213–2216.
- Chapman, S., 1930. On ozone and atomic oxygen in the upper atmosphere. *Phil. Mag. Ser. 7*, vol. 10 (64), 369–385.
- Fedorov, V.M., 2013. Interannual variations in the duration of the tropical year. *Doklady Earth Sciences* 451, pt. 1, 750–753, DOI: 10.1134/S1028334X13070015.
- Fedorov, V.M., 2015a. Trends of the changes in sea ice extent in the Northern Hemisphere and their causes. *Earth's Cryosphere XIX* (3), 46–57.
- Fedorov, V.M., 2015b. Spatial and temporal variation in solar climate of the Earth in the present epoch. *Geophys. Processes and Biosphere* 14 (1), 5–22.
- Fedorov, V.M., 2018. The Earth's Insolation and Current Climate Changes. *Fizmatlit, Moscow*, 232 pp. (in Russian).
- Fedorov, V.M., 2019. Earth insolation variation and its incorporation into physical and mathematical climate models. *Physics Uspekhi* 62 (1), 32–45, DOI: 10.3367/UFNe.2017.12.038267.
- Fedorov, V.M., Frolov, D.M., 2019. Spatial and temporal variability of solar radiation arriving at the top the atmosphere. *Cosmic Research (English translation of kosmicheskie issledovaniya)*, Maik Nauka/Interperiodica Publishing (Russian Federation), vol. 57 (3), 156–162, DOI: 10.1134/S0010952519030043.
- Fedorov, V.M., Grebennikov, P.B., 2018. Insolation contrast of the Earth and changes in the sea ice extent in the Northern Hemisphere. *The Arctic: Ecology and Economy*, No. 4 (32), 86–94.
- Fedorov, V.M., Kostin, A.A., 2019. Insolation calculations for the period from 3000 BC to 2999 AD. *Protsessy v geosredakh (Processes in Geoenvironments)*, No. 2, 254–262.
- Fetterer, F., Knowles, K., Meier, W., et al., 2017. Updated daily sea ice index, version 3. Boulder, Colorado USA. NSIDC: National Snow and Ice Data Center, DOI: 10.7265/N5K072F8.
- Frolov, I.E., Gavrilov, V.P. (Eds.), 1997. *Sea Ice. Gidrometeoizdat, St. Petersburg*, 402 pp. (in Russian).
- Giorgini, J.D., Yeomans, D.K., Chamberlin, A.B., et al., 1996. JPL's On-Line Solar System Data Service. *Bull. Amer. Astronomical Soc.* 28 (3), 1158.
- Hunt, B.G., 1966. The need for a modified photochemical theory of the ozonosphere. *J. Atmos. Sci.* 23 (1), 88–95.
- Istoshin, Yu.V., 1956. *The Oceanography. Gidrometeoizdat, Leningrad*, 304 pp. (in Russian).
- Kopp, G., Lean, J., 2011. A new lower value of total solar irradiance: Evidence and climate significance. *Geophys. Res. Lett.* 37, p. L01706, DOI: 10.1029/2010GL045777.
- Koryakin, V.S., 1988. *Arctic Glaciers. Nauka, Moscow*, 160 pp. (in Russian).
- Krueger, A.J., Minzner, R.A., 1976. A mid-latitude ozone model for the 1976 U.S. Standard Atmosphere. *J. Geophys. Res.* 81 (24), 4477–4481.
- Perov, S.P., Khrgian, F.Kh., 1980. *Modern Atmospheric Ozone Problems. Gidrometeoizdat, Leningrad*, 288 pp. (in Russian)
- Staehelin, J., Renaud, A., Bader, J., et al., 1998. Total ozone series at Arosa (Switzerland): Homogenization and data comparison. *J. Geophys. Res.* 103, No. DS, 5827–5841, DOI: 10.1029/97JD02402.
- Staehelin, J., Viatte, P., Stubi, R., et al., 2018. Stratospheric ozone measurements at Arosa (Switzerland): history and scientific relevance. *Atmos. Chem. Phys.* 18, 6567–6584, DOI: 10.5194/acp-18-6567-2018.
- Tsymbalenko, T.T., Baydakov, A.N., Tsimbalenko, O.S., Gladilin, A.V., 2007. *Methods of Mathematical Statistics in the Processing of Economic Information. Finansy i Statistika, Moscow*, 200 pp. (in Russian).
- Visheratin, K.N., 2007. Interannual variations and trends in zonal mean series of total ozone, temperature and zonal wind. *Izv. RAS. FAO*, 43 (4), 67–85.
- Walsh, J.T., Chapman, W.L., 2001. 20th century sea-ice variations from observational data. *Ann. Glaciol.* 33, 444–448.
- Zubakin, G.K. (Ed.), 2006. *Ice Formations in the Western Arctic Seas. AANII, St. Petersburg*, 272 pp. (in Russian).
URL: <http://nsidc.org/> (last visited: 25.08.2019).
URL: https://acd-ext.gsfc.nasa.gov/Data_services/merged/ (last visited: 25.08.2019).
URL: <http://meteoinfo.ru/> (last visited: 25.08.2019).
URL: <https://www.woudc.org/> (last visited: 25.08.2019).
URL: <http://ssd.jpl.nasa.gov/> – NASA, Jet Propulsion Laboratory California Institute of Technology (JPL Solar System Dynamics) (last visited: 25.08.2019).

Received August 30, 2019

Revised version received November 6, 2019

Accepted December 3, 2019

GASES AND GAS HYDRATES IN THE EARTH'S CRYOSPHERE

DOI: 10.21782/EC2541-9994-2020-2(34-40)

INFLUENCE OF HYDRATE FORMATION
ON GAS PERMEABILITY VARIATIONS IN FROZEN SANDSE.M. Chuvilin¹, S.I. Grebenkin¹, D.A. Davletshina^{1,2}, M.V. Jmaev²¹ Skolkovo Institute of Science and Technology, Skolkovo Innovation Center,
build. 3, Nobil str., Moscow, 143026, Russia; e.chuvilin@skoltech.ru² Lomonosov Moscow State University, Faculty of Geology, 1, Leninskie Gory, Moscow, 119991, Russia

The study of gas permeability variations in frozen sand samples exposed to subfreezing temperatures during hydrate formation included experimental modeling with the experiments run on a specially designed system, which enabled determination of gas permeability of dispersed soils in a context of freezing and hydrate saturation. The experimentally obtained data on gas permeability variations in frozen sand samples artificially saturated with methane or carbon dioxide during hydrate formation at a temperature of -5°C has revealed that a decrease in gas permeability occurring during hydrate formation in frozen sand samples is controlled primarily by the initial ice content. A reduction in gas permeability depending on the fraction of pore ice converted to hydrate has been calculated. At this, the behavior of reduced gas permeability in frozen sand samples is found to be largely influenced by the type of hydrate-forming agent.

Frozen sands, hydrate formation, gas permeability, ice saturation, gas hydrates, methane, carbon dioxide

INTRODUCTION

Naturally occurring gas hydrates are known to exist under specific pressure and temperature conditions in deep marine environments (ocean-bottom sediments) and in areas with thick permafrost or in the underlying unfrozen sediments (sub-permafrost horizons) [Istomin, Yakushev, 1992]. In permafrost settings, a prerequisite for existence of gas hydrates is associated with accumulation of natural gas (primarily, methane) in large amounts in the conditions appropriate for hydrate formation as a result of gas and water freezing in situ in profoundly cooled ground over a long period of time. Numerous gas liberation phenomena which may be directly attributable to dissociating intra-permafrost gas hydrates were reported as early as 1970s during development of numerous oil/gas fields in Western Siberia [Cherskiy et al., 1983; Ginsburg, Soloviev, 1990; Are, 1998; Yakushev, 2009].

Formation of permafrost-hosted gas hydrates (in gas-saturated sediments) under conditions allowing for pure methane hydrate to be stable, i.e. origination of gas hydrate stability zone (HSZ), takes place both at low positive and negative temperatures, when a gas accumulation that has not converted to gas hydrate becomes trapped within frozen sediments [Cherskiy et al., 1983; Ginsburg, Soloviev, 1990; Istomin, Yakushev, 1992; Romanovsky, 1993; Chuvilin et al., 2000]. In this situation, formation of gas hydrate is based on gas molecule entrapment by ice matrix.

Note that permanently frozen sediments may favor cryogenic concentration of gases and their subsequent accumulation in horizons with good reservoir properties [Yakushev, 1989, 2009; Chuvilin et al., 2000]. Further freezing of such “gas pockets” may create above equilibrium pressure, thereby leading to the gas phase change to its hydrate form. In permafrost regions, gas hydrates also form by freezing in closed talik (unfrozen ground) zones saturated with gas, usually localized beneath lakes [Istomin et al., 2018]. In addition to cryogenic concentration, the formation of permafrost-associated gas hydrate is favored by the pressure effect (the so called “baric factor”) which is associated either with the overlying ice sheets (continental glaciation) or with transgressions of the Arctic seas (when gas and water froze in place during ice-age cooling events) [Trofimuk et al., 1986; Romanovsky, 1993]. Thus, glacial ice aggradation atop thick permafrost promotes expansion of the zone of hydrate stability into permafrost, forcing the permafrost table to occur at shallow depths.

Gas hydrates in areas of permafrost distribution are therefore localized beneath permafrost at low positive temperatures, as well within permafrost at negative temperatures, and play a fairly critical role in stability of permafrost environments. The presence of gas hydrates in frozen sediments affects significantly their thermal and mechanical properties, as well as porosity and permeability.

The literature data analysis has revealed only few works investigating thermophysical, mechanical properties and permeability of frozen hydrate-saturated deposits [Ershov *et al.*, 1996; Chuvilin, Grebenkin, 2015; Li *et al.*, 2016; Chuvilin, Bukhanov, 2017; Chuvilin *et al.*, 2018]. Studies of porosity and permeability of hydrate-saturated rocks generally investigate these aspects at positive temperatures. However, some of them highlight porosity and permeability of rocks containing either pore ice or pore hydrate [Ananyan *et al.*, 1972; Starobinets, Murogova, 1985; Seyfried, Murdock, 1997; Jaiswal *et al.*, 2004; Minagawa *et al.*, 2005; Murray *et al.*, 2006; Kneafsey *et al.*, 2008; Kumar *et al.*, 2010; Johnson *et al.*, 2011; Chuvilin, Grebenkin, 2015; Chuvilin *et al.*, 2018], as well as ice formed during the freezing of hydrate-saturated sediment. Yet, the obtained research results provided extremely scant experimental data on changes in frozen sediment permeability to gas (henceforward, gas permeability) upon hydrate formation from pore ice.

With this in mind, special experiments have been designed and conducted to study gas permeability of frozen sediments during hydrate formation.

EXPERIMENTAL METHODS

Gas permeability variations in hydrate-bearing sands were studied using a method designed by the authors jointly with colleagues from Schlumberger Company [Chuvilin, Grebenkin, 2015] by means of gas flushing through a sample on a specially designed experimental setup which allows creating and maintaining pressure and temperature conditions suitable for artificial freezing and hydration of sand samples. The procedure involved: i) preconditioning of soil sample to provide a specified water content, its freezing and saturation of the frozen sample with a hydrate-forming gas in a special pressure cell, ii) hydrate accumulation, iii) testing the sample for permeability to gas at different gas pressures and temperatures, and iv) processing the experimental data.

The experimental study of gas permeability variations in ice- and hydrate-containing sediments employed a system specially designed by EcoGeosProm LLC (Fig. 1), which maintains sample temperatures and pressures widely ranging from -15 to $+30$ °C and up to 100 bar, respectively.

Preparation of soil sample with prespecified moisture content at the beginning of the experiment included the following steps: air-dried soil mass was thoroughly mixed with water and rested for half an hour for uniform moisture saturation. After that, the moisturized soil was placed in a rubber cuff 3 cm in diameter and compacted layer-by-layer (the length of soil of sample is 3–4 cm). Then the sample was placed into the pressure cell, to be exposed to compression (pressure: up to 60 bar) and freezing, with tempera-

ture and pressure being monitored in the pressure cell during the run. After that the sample was saturated with a hydrate-forming gas (CH_4 and CO_2) along with the gas permeability monitoring.

The levels of pore filling with hydrate and ice were found using the PVT (pressure–volume–temperature) analysis during the experiment [Chuvilin *et al.*, 2019]. The main calculated parameters are described below.

The hydration coefficient (K_h) is the proportion of pore water converted to hydrate relative to total amount of water in the sample, which was found using the formula

$$K_h = \frac{W_h}{W},$$

where W_h is the amount of moisture converted to hydrate (% relative to dry sample weight); W is the moisture content by weight, %.

Percentage of pore filled with hydrate or hydrate saturation (S_h , %):

$$S_h = \frac{H_v}{n},$$

where n is the sample porosity; H_v is the volume content of hydrate, %;

$$H_v = \frac{M_h \rho}{M_s \rho_h} \cdot 100 \%,$$

where M_h is the mass of pore hydrate, g; M_s is the mass of soil sample, g; ρ is the initial (before hydrate saturation) density of soil, g/cm^3 ; ρ_h is the density of empty crystalline lattice of methane hydrate equal to $0.794 \text{ g}/\text{cm}^3$ [Chuvilin, Bukhanov, 2017].

Percentage of pore space filled with ice, or ice saturation (S_i , %) was determined as

$$S_i = \frac{\rho_d W}{0.92n},$$

where ρ_d is density parameter of the soil skeleton.

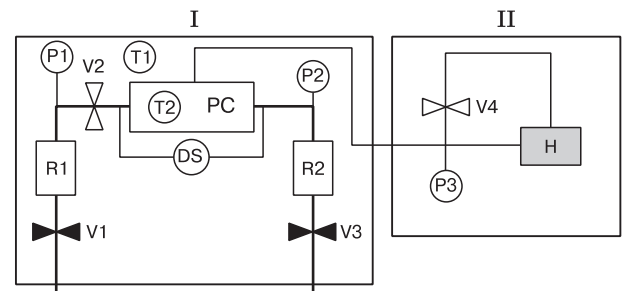


Fig. 1. Schematic map of the experimental setup for evaluating gas permeability in sand samples:

I – measuring system; II – triaxial compression system; V1–V3 = membrane valves for gas input; V4 = ball valve of the hydraulic system; R1, R2 = receivers of gas input; P1–P3 = pressure sensors; DS = differential pressure sensor; H = hydraulic pump with an oil tank; PC = pressure cell; T1, T2 = temperature sensors.

The hydrate content values in soils were calculated using the hydrate numbers 5.9 (for CH₄) and 6.1 (for CO₂).

The effective gas permeability (K_g , mD) of the frozen hydrate-containing sand sample was calculated by solving the differential equation of mass transfer through the sample under the pressure gradient [Chuvilin, Grebenkin, 2015]:

$$K_g = \frac{2\eta LV_1 p_1 (p_{10} - p_{1k})}{S p_{10} (p_1^2 - p_2^2) t_1}$$

where η is the dynamic viscosity of gas, Pa·s; L is the length of sample, cm; S is the cross-section area of sample, cm²; V_1 is the receiver volume, cm³; p_1 is the pressure at sensor 1 (before the sample) at the time t_1 (bar); p_2 is the pressure at sensor 2 (after the sample) at time t_1 (bar); p_{10} is the pressure before the sample at the start time, bar; p_{1k} is the pressure at sensor 1 at the end time, bar.

The relative permeability value (K_r , u.f.) also used in the calculations is determined as the ratio of the effective permeability of the hydrate-saturated sample to the frozen sample permeability at the start of the experiment.

The object of the experimental study were deformed natural sands of marine genesis (mQ₃) recovered while drilling into permafrost (sampling depth: 36–46 m) within the South Tambey gas condensate field (Yamal Peninsula). The particle size distribution of fine-grained sand (according to the E.M. Sergeev's classification) was determined according to GOST 12536-2014 [State Standard, 2014]:

Particle size distribution in mass fractions, %	0.2	29.1	62.3	8.4
Particle diameter range, mm	1–0.5	0.5–0.25	0.25–0.1	0.1–0.05

The mineral composition of soil was measured using x-ray diffractometry. Fine-grained sand consisted dominantly of quartz (93.7 %), other minerals contained in the sand were albite (5.1 %) and orthoclase (1.2 %). The density of solid grains of fine sand is 2.69 g/cm³, its salinity inferred from the chemical

Table 1. Characteristics of sand samples before hydrate saturation

Sample no.	Moisture content, %	Soil skeleton density, g/cm ³	Density, g/cm ³	Porosity, u.f.
1	8.5	1.69	1.84	0.37
2	9.5	1.72	1.88	0.36
3	10	1.73	1.91	0.35
4	11	1.69	1.87	0.37
5	10	1.57	1.73	0.41
6	10	1.68	1.83	0.39
7	12	1.54	1.73	0.42
8	14	1.63	1.86	0.39

analysis of water extract is 0.06 %. The physical characteristics of the test sample determined in accordance with standard procedures of GOST 5180-2015 [State Standard, 2015] and SNiP 2.02.04-88 [Building Code..., 1990] include: specific surface area of the sand (0.24 m²/g); prespecified moisture content 8.5–14 %; density of soil skeleton varying from 1.54 to 1.73 g/cm³ and sample density from 1.73 to 1.91 g/cm³, while porosity of the soil samples lay within the range of 0.35–0.42 u.f. (Table 1).

RESULTS AND DISCUSSION

Gas permeability of frozen sand samples before hydrate saturation. The initial gas permeability data of frozen sand samples non-containing hydrate are presented in Table 2. These data allow to infer that the highest gas permeability prior to hydrate saturation ($K_g = 23.3$ mD) is characteristic of sample 1 with ice saturation of 38 %, and the lowest ($K_g = 1.5$ mD) – of sample 8 with ice saturation of 62.8 %. It is shown that the gas permeability of frozen samples varies within 15–23 mD as ice saturation of pore space increased from 38 to 50 % in the preconditioned sand samples (Fig. 2).

With further increase in ice saturation (>50 %), gas permeability progressively decreases (because of higher occupancy of pore space by ice), and so does the effective porosity.

Variations in permeability of frozen sand samples during hydrate saturation. After determining the initial gas permeability of sand samples upon their freezing, they were saturated with a hydrate-forming gas (CH₄ or CO₂). The samples were saturated with hydrate at a constant negative temperature (–5 °C) and gas pressure higher than equilibrium pressure (50–60 bar for CH₄ and 25–30 bar for CO₂).

Analysis of the obtained data allowed an inference that when pore ice converts to hydrate, a reduction in the effective permeability of the test samples varies widely within a range of 1.5 to 30 times (Table 3).

The lowest reduction in permeability (less than twice) was shown in sample 2 with a low initial ice saturation (41.6 %). After the sample was saturated with CO₂ hydrate, its gas permeability decreased from 20.6 to 12.66 mD. As much as 32 % of the pore

Table 2. Initial gas permeability of frozen sand samples (before hydrate saturation)

Sample no.	S_i , %	K_g , mD
1	38.0	23.3
2	41.6	20.6
3	49.2	21.5
4	50.1	19.6
5	40.5	14.6
6	42.9	21.5
7	51.8	5.7

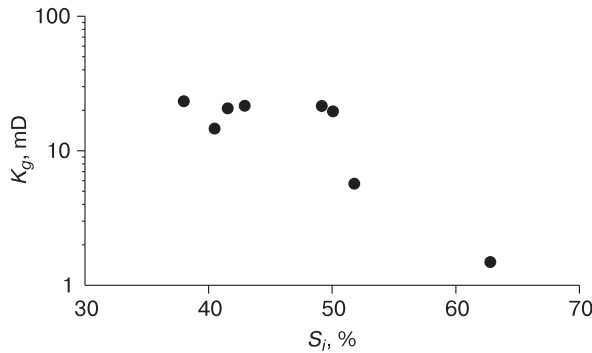


Fig. 2. Ice saturation (S_i) effect on gas permeability (K_g) of frozen sand samples before hydrate saturation at $T = -5\text{ }^\circ\text{C}$.

ice was converted to hydrate, with affiliated decrease from 58.8 to 44 % in the fraction of free void pore space ($1 - (S_i + S_h)$).

The permeability values showed the greatest decrease in sample 8 with the maximal (in the experiments) initial ice saturation (62.8 %). When only 21 % of the pore ice was converted to methane hydrate, the sample’s permeability decreased by almost 30 times (from 1.5 to 0.05 mD), while the void space changed slightly (from 37.2 to 30.8 %).

The greatest decrease in gas permeability of the frozen sands during hydration is thus observed in samples with a high percentage of pore space filled with ice, despite the fact that the fraction of pore ice changed to hydrate shows a decreasing trend for them.

Analysis of the hydrate formation kinetics revealed that permeability reduction during the pore transition ice to hydrate is marked by certain differentiation between CH_4 and CO_2 hydrate (Fig. 3).

In the test samples saturated with CO_2 hydrate, the ice to hydrate conversion was markedly accelerated. Thus, percentage of ice changed to hydrate over the first 5 hours of the run differed for CO_2 -saturated sample 4 (13.9 %) and for methane-saturated sam-

Table 3. Variation in effective gas permeability of sand samples before (numerator) and after (denominator) hydrate saturation at $T = -5\text{ }^\circ\text{C}$

Gas	Sample no.	S_i	S_h	$1 - (S_i + S_h)$	K_h	K_g
CO_2	1	38.0	0	62.0	0	23.3
		18.5	35.7	45.8	0.62	4.04
	2	41.6	0	58.8	0	20.6
		32.4	23.6	44.0	0.32	12.66
	3	49.2	0	50.8	0	21.5
		35.9	32.4	31.7	0.37	10.44
	4	50.1	0	49.9	0	19.6
		23.5	56.6	19.9	0.64	5.47
CH_4	5	40.5	0	59.5	0	14.6
		21.1	26.6	52.3	0.47	2.04
	6	42.9	0	57.1	0	21.5
		24.1	35.0	40.9	0.59	10.25
	7	51.8	0	48.2	0	5.7
		26.3	54.7	19.0	0.64	0.24
	8	62.8	0	37.2	0	1.5
		51.3	17.9	30.8	0.21	0.05

Note. S_i = ice saturation, %; S_h = hydrate saturation, %; K_h = coefficient of hydration, u.f.; K_g = coefficient of effective gas permeability, mD.

ple 6 (about 6 %). During the next day, the rate of ice to hydrate conversion also varied during the first 30 hours of the run: 35 % and 23 % for sample 4 and sample 6, respectively. When hydrate formation rates started to decrease, they became fairly equated: during 50 h after the start of the experiment the percentage of ice changed to hydrate amounted to 43.6 % and 31 % for CO_2 - and methane-laden samples, respectively. In later part of the experiment, the ice-to-hydrate conversion rate was lower for carbon dioxide than for methane. Thus, in 120 hours after the start of the experiments, the fractions ice of changed to hydrate accounted accordingly for 58 % in CO_2 -laden sample 4 and 52 % and in CH_4 -laden sample 6.

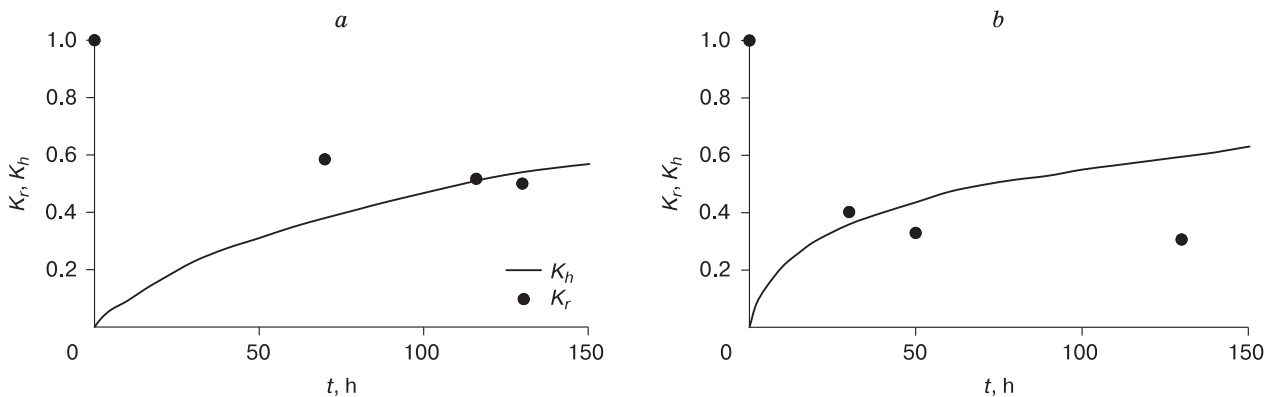


Fig. 3. Time (t)-dependent variations in the hydration coefficient (K_h) and relative gas permeability (K_r) during saturation of sample 6 with CH_4 hydrate (a) and sample 4 with CO_2 hydrate (b).

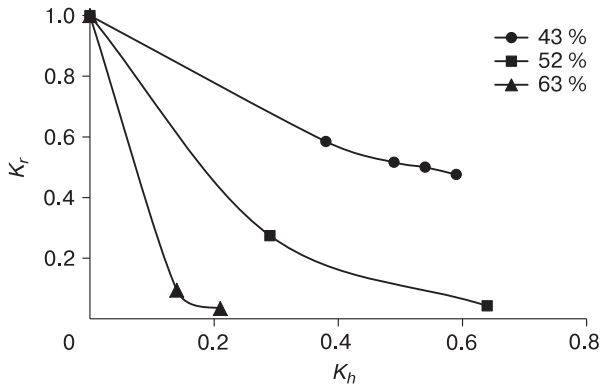


Fig. 4. Effect of the percentage of pore ice converted to methane hydrate (K_h) on the reduction in relative gas permeability (K_r) of frozen sand samples at $T = -5\text{ }^\circ\text{C}$ with different initial ice saturations.

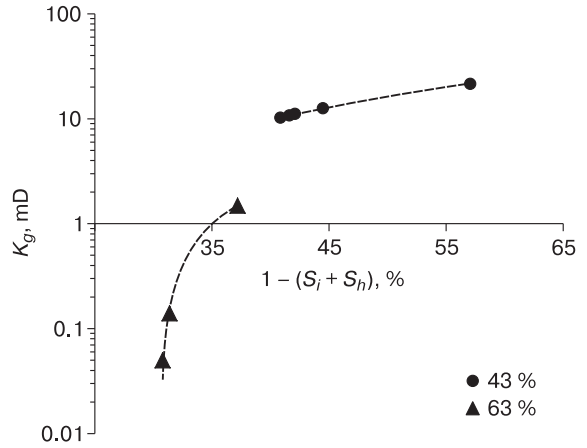


Fig. 5. A relationship between gas permeability (K_g) of frozen sand samples with different initial level of pore filling with ice (43 and 63 %), and variations in void space ($1 - (S_i + S_h)$) during hydrate formation.

All in all, the samples' permeabilities changed inversely proportional to the hydration coefficient throughout the experiment. Despite the greatest decrease in gas permeability was reported in first hours after the hydrate formation for both runs, the permeability behavior differed at a later stage: it changed only slightly with CO_2 , and decreased significantly with methane.

Thus, the process of CO_2 hydrate formation from ice occurred more intensely at the start of hydrate formation and slowed down considerably after 50 % of ice converted to hydrate. At this, ice converts to methane hydrate with a lower reduction in the hydrate formation rate over time.

The study enabled analysis of the hydration coefficient (K_h) effect on reduction in gas permeability at

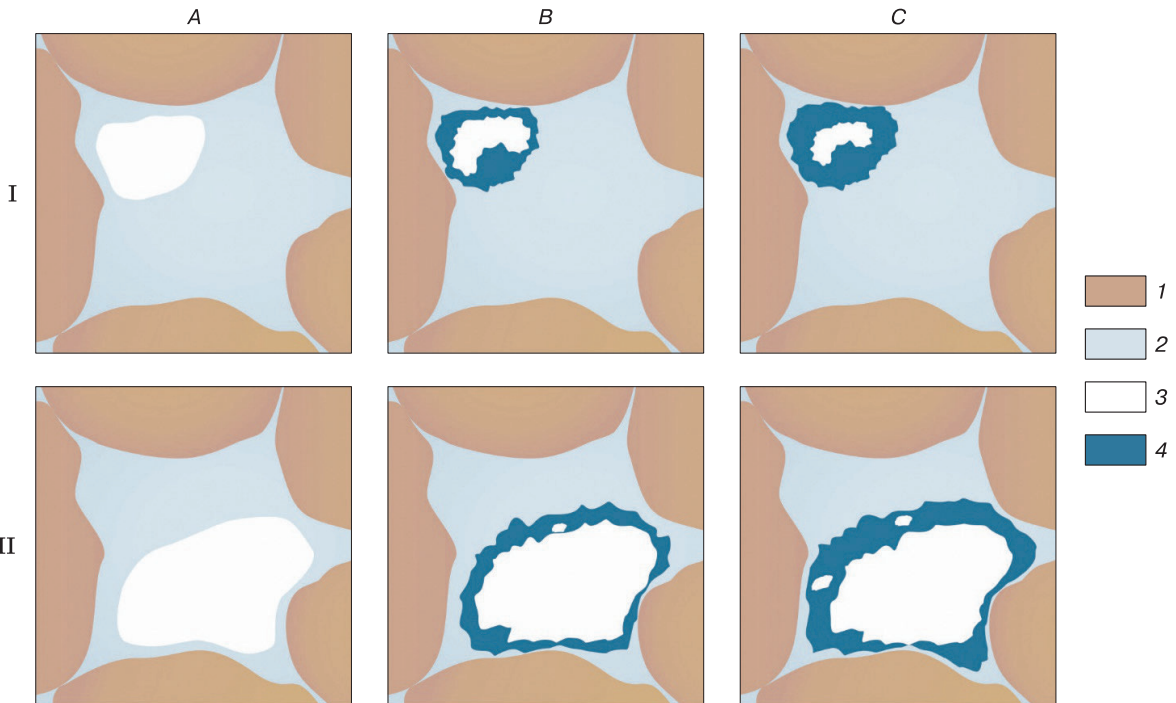


Fig. 6. Schematic diagram of variations in the level of void pore space of gas-saturated frozen sand at high (I) and low (II) percentage of pore space filled with ice during hydrate formation.

A, B, C – before (A), at the start (B) and after (C) hydrate formation; 1 – sand particles; 2 – ice; 3 – gas; 4 – gas hydrate.

a negative temperature ($-5\text{ }^{\circ}\text{C}$) for all the test samples (Fig. 4).

The results have demonstrated that the higher the initial ice saturation of test samples, the greater the influence of the hydration coefficient on gas permeability, while the maximum reduction in permeability is reported at early stage of the hydrate formation process. Given percentage of pore space filled with ice reduces, the behavior of change in permeability during the pore ice to hydrate conversion shows a smoother pattern.

The effect of hydrate formation process on variations in the void pore space of the sand samples considering their initial percentage of pore space filling with ice differ (43 and 63 %) is shown in Fig. 5.

The calculations demonstrate that during the pore ice to hydrate conversion, the cumulative percentage of pore space filled with ice and hydrate increases due to the difference in their specific volume (about 15 %). Hence, the void pore space will decrease. With higher occupancy of pore space with ice (63 %), even slight changes in void pore space cause a dramatic decrease in the sample's gas permeability, as compared to lower initial ice saturation (43 %) (Fig. 5). A schematic representation of the variations in void pore space of gas-saturated frozen sand at different levels of pore occupancy with ice is shown in Fig. 6.

Thus, changing void pore space during the pore ice to hydrate conversion is interpreted to be one of the major controls of variations in gas permeability of frozen sand samples during hydrate formation.

CONCLUSIONS

An experimental evaluation of the influence of the hydrate formation process on the effective gas permeability of frozen sand samples was carried out. This allowed to infer that hydrate formation at negative temperatures entails a decrease in the gas permeability of ice-containing sand samples. At this, the magnitude of the gas permeability reduction is dictated by the initial ice content. Thus, for a sample with a high cumulative occupancy of pore space with ice (about 63 %), the gas permeability showed a 30-fold decrease, while in the sample with a lower initial ice saturation (42 %), it decreased by less than twice. The experimental studies have highlighted the effect of the type of hydrate-forming gas (CH_4 , CO_2), which is primarily manifested through the hydrate formation kinetics and the intensity of gas permeability reduction over time. The gas permeability variation in frozen sand samples is shown to be inversely proportional to the coefficient of hydration.

The work was financially supported by the Russian Foundation for Basic Research (project No. 17-05-00995) and the Russian Science Foundation (grant No. 18-77-10063).

References

- Ananyan, A.A., Arutyunyan, N.A., Mazurov, V.A., Silvestrov, L.K., 1972. On permeability of permafrost. *Merzlotnue Issledovaniya (Permafrost Studies)*, No. 12, 205–209.
- Are, F.E., 1998. Problem of deep gas emission into the atmosphere. *Kriosfera Zemli (Earth's Cryosphere)*, II (4), 42–50.
- Building Codes and Regulations, 1990. SNiP 2.02.04-88. Foundation Beds and Foundations in Permafrost Soils. Gosstroy (USSR), Moscow, 52 pp. (in Russian).
- Cherskiy, N.V., Tsarev, V.P., Nikitin, S.P., 1983. Conditions for Gas Accumulation in Gas Hydrate Deposits: Investigation and Prediction. *Izd. Yakut. fil. SO AN SSSR, Yakutsk*, 156 pp. (in Russian).
- Chuvilin, E.M., Bukhanov, B.A., 2017. Effect of hydrate formation conditions on thermal conductivity of gas-saturated sediments. *Energy and Fuels*, No. 31, 5246–5254.
- Chuvilin, E.M., Bukhanov, B.A., Grebenkin, S.I., et al., 2018. Shear strength of frozen sand with dissociating pore methane hydrate: An experimental study. *Cold Regions Sci. and Technol.* 153, 101–105.
- Chuvilin, E.M., Davletshina, D.A., Lupachik, M.V., 2019. Hydrate formation in frozen and thawing methane-saturated sediments. *Earth's Cryosphere XXIII (2)*, 42–52.
- Chuvilin, E.M., Grebenkin, S.I., 2015. Gas permeability variations in gas-filled soils upon hydrate formation and freezing: an experimental study. *Earth's Cryosphere XIX (2)*, 59–64.
- Chuvilin, E.M., Yakushev, V.S., Perlova, E.V., 1998. Gas and gas hydrates in the permafrost of Bovanenkovo gas field, Yamal Peninsula, West Siberia. *Polarforschung (erschienen 2000)*, vol. 68, 215–219.
- Ershov, E.D., Yakushev, V.S., Chuvilin, E.M., 1996. Laboratory studies of frozen natural and artificial hydrate-containing rock samples. In: *Proc. 2nd Intern. Conf. on Natural Gas Hydrates (Toulouse, France, June 2–6, 1996)*, Toulouse, pp. 609–615.
- Istomin, V.A., Chuvilin, E.M., Sergeeva, D.V., et al., 2018. Thermodynamic calculation of freezing temperature of gas-saturated pore water in talik zones. In: *5th European Conf. on Permafrost (Chamonix, France, June 23–July 1, 2018)*, Chamonix, pp. 480–481.
- Istomin, V.A., Yakushev, V.S., 1992. *Naturally Occurring Gas Hydrates*. Nedra, Moscow, 235 pp. (in Russian).
- Ginsburg, G.D., Soloviev, V.A., 1990. Geological models of gas hydrate formation. *Litologiya i Poleznye Iskopaemye (Lithology and Mineral Resources)*, No. 2, 76–87.
- Jaiswal, N.J., Westervelt, J.V., Patil, S.L., et al., 2004. Phase behavior and relative permeability of gas-water-hydrate system. In: *Aapg, Hedberg. Conf. "Gas Hydrates: Energy Resource Potential and Associated Geologic Hazards"* (Vancouver, BC, Canada, Sept. 12–16, 2004), Vancouver, pp. 26–35.
- Johnson, A., Patil, S., Dandekar, A., 2011. Experimental investigation of gas-water relative permeability for gas-hydrate-bearing sediments from the Mount Elbert Gas Hydrate Stratigraphic Test Well, Alaska North Slope. *Marine and Petroleum Geol.*, No. 23, 419–426.
- Kneafsey, T.J., Gupta, A., Seol, Y., Tomutsa, L., 2008. Permeability of laboratory-formed methane hydrate-bearing sand, OTC19536-PP, SPE. In: *Offshore Technology Conf. (Houston, TX, USA, May 7, 2008)*, Houston, pp. 21–34.
- Kumar, A., Maini, B., Bishnoi, P.R., et al., 2010. Experimental determination of permeability in the presence of hydrates and its effect on the dissociation characteristics of gas hyd-

- rates in porous media. *J. Petroleum Sci. and Eng.*, No. 70, 114–122.
- Li, Y., Liu, W., Zhu, Y., et al., 2016. Mechanical behaviors of permafrost-associated methane hydrate-bearing sediments under different mining methods. *Appl. Energy* 162, 1627–1632.
- Minagawa, H., Ohmura, R., Takahashi, T., et al., 2005. Water permeability measurements of natural gas hydrate-bearing sediments obtained from Mallik 5L-38. In: *Abstr. of Mallik Intern. Symposium – from Mallik to the Future*. Technol. Res. Center Jap. National Oil Corporation, pp. 398–401.
- Murray, D., Fukuhara, M., Khong, C.K., et al., 2006. Permeability estimates in gas hydrate reservoirs of the Nankai trough. In: *SPWLA 47th Ann. Logging Symposium* (Veracruz, June 4–7, 2006), Veracruz, Mexico, pp. 1–6.
- Romanovsky, N.N., 1993. *Fundamentals of Cryogenesis in the Lithosphere*. Moscow University Press, Moscow, 336 pp. (in Russian).
- Seyfried, M.S., Murdock, M.D., 1997. Use of air permeability to estimate infiltrability of frozen soil. *J. Hydrology* 202, 95–107.
- Starobinets, I.S., Murogova, R.N., 1985. Screen and conductive role of permafrost in respect to migrating hydrocarbons. *Geologiya Nefti i Gaza (Oil and Gas Geology)*, No. 1, 24–27.
- State Standard, 2014. GOST 12536-2014. Soils. Methods of Laboratory Analysis of Granulometric (grain-size) and Microaggregate Distribution. Standards Publishing, Moscow, 24 pp. (in Russian).
- State Standard, 2015. GOST 5180-2015. Soils. Laboratory Methods for Determination of Physical Characteristics. Standartinform, Moscow, 23 pp. (in Russian).
- Trofimuk, A.A., Makogon, Yu.F., Yakushev, V.S., 1986. Influence of hydrate formation zones on the temperature regime of rocks in permafrost. *Geologiya i Geofizika (Soviet Geology and Geophysics)*, No. 11, 3–10.
- Yakushev, V.S., 1989. One possible cause of gas bursts in permafrost. *Geologiya Nefti i Gaza (Oil and Gas Geology)*, No. 14, 45–46.
- Yakushev, V.S., 2009. *Natural Gas and Gas Hydrates in Permafrost*. VNIIGAZ, Moscow, 192 pp. (in Russian).

Received July 4, 2019

Revised version received September 21, 2019

Accepted October 1, 2019

PERMAFROST ENGINEERING

DOI: 10.21782/EC2541-9994-2020-2(41-44)

ESTIMATING THE EFFICIENCY OF HET SYSTEMS USING CARBON DIOXIDE AND AMMONIA AS REFRIGERANTS

G.V. Anikin, D.V. Mochalov

Earth Cryosphere Institute, Tyumen Scientific Centre SB RAS,
86, Malygina str., Tyumen, 625026, Russia; anikin@ikz.ru, Dima_72m@mail.ru

Results of the comparison made between total capacities of horizontal evaporator tube (HET) systems (Russian brand name “GET” systems for thermosyphons) using dioxide and ammonia as the working fluids has revealed that the total capacity of HET systems charged with carbon dioxide is always higher, against the systems charged with ammonia.

Permafrost, HET, seasonal refrigeration system, refrigerant, ammonia, carbon dioxide

INTRODUCTION

Systems for ground temperature stabilization, or ground cooling systems, with horizontal evaporator tubes (for short HET systems) are used to maintain below freezing temperatures in permanently frozen soils of the structures' bases during the winter season. A schematic representation of the system is shown in Fig. 1. The mathematical model describing an HET system operation is provided in [Anikin, 2009]. The mathematical modeling for HET systems using ammonia as the working fluid (coolant) is discussed in [Anikin et al., 2011]. While different coolants can be used as the working fluid for such systems, not all coolants are capable to ensure the system's performance. The analysis provided in [Anikin, Spasennikova, 2014] concerns several coolants applicable in such systems, among them: carbon dioxide, ammonia, Freon 22, freon 12, freon 142, freon 21, freon 11, methylene chloride, acetone, freon 113, methanol. The coolants were analyzed in the context of the Vankor oil-gas field development, with the air temperatures measured at the Igarka weather station. According to the conclusions the authors have arrived thereat, such coolants as methylene chloride, acetone, freon 113 and methanol fail to ensure the system's operation during the winter season. Whereas carbon dioxide and ammonia have proven to be more effective.

The systems of this type – thermosyphons – which use ammonia as the working fluid (coolant) developed by *FundamentStroiArkos* have been widely used in Russia to preserve and cool permafrost. Establishing the upper and lower limits for thermal loads for an HET system working on ammonia was

discussed in [Melnikov et al., 2017]. The Institute of Earth's Cryosphere, Siberian Branch of the Russian Academy of Sciences has developed seasonal cooling systems working on carbon dioxide. These start working once the ground becomes a few tenths of a degree warmer than the overlying atmosphere (the temperature difference is almost zero), while systems charged with ammonia are shown to be less temperature-sensitive, inasmuch as they start working when the ground is a few degrees warmer than the atmosphere [Anikin, Spasennikova, 2014]. Thus, the operating time of the ground stabilization cooling system charged with carbon dioxide during the winter season is significantly longer than the operating time of the system using ammonia as the working fluid. Accordingly, the capacity of the system charged with carbon dioxide can be significantly greater than that of charged with ammonia.

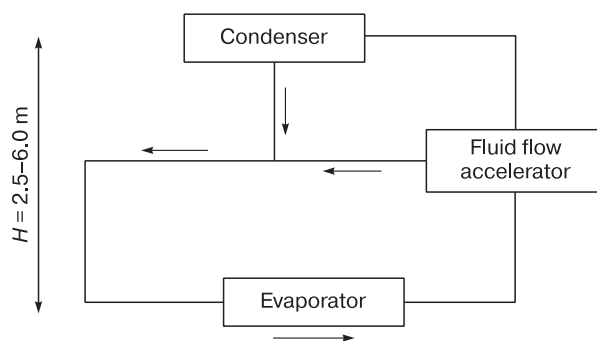


Fig. 1. A layout scheme of an HET system.

Table 1. The relationship between the system's cooling capacities for carbon dioxide and ammonia at a preset temperature

H, m	Δ_{CO_2}	Δ_{am}	$t_{gr} - t_{air}$									
			1	2	3	4	5	6	7	8	9	10
1	2	3	4	5	6	7	8	9	10	11	12	13
<i>Condenser temperature -30 °C</i>												
2.5	0.54	2.86	∞	∞	17.17	3.02	2.08	1.74	1.56	1.45	1.38	1.32
3.0	0.65	3.43	∞	∞	∞	5.85	2.77	2.08	1.78	1.61	1.50	1.42
3.5	0.76	4.00	∞	∞	∞	13526.82	4.24	2.62	2.08	1.81	1.65	1.54
4.0	0.87	4.57	∞	∞	∞	∞	9.63	3.59	2.52	2.08	1.84	1.68
4.5	0.98	5.14	∞	∞	∞	∞	∞	5.85	3.24	2.46	2.08	1.86
5.0	1.09	5.71	-	∞	∞	∞	∞	17.17	4.60	3.02	2.41	2.08
5.5	1.20	6.29	-	∞	∞	∞	∞	∞	8.12	3.97	2.87	2.37
6.0	1.31	6.86	-	∞	∞	∞	∞	∞	39.74	5.85	3.59	2.77
6.5	1.42	7.43	-	∞	∞	∞	∞	∞	∞	11.51	4.83	3.34
7.0	1.52	8.00	-	∞	∞	∞	∞	∞	∞	13526.82	7.47	4.24
7.5	1.63	8.57	-	∞	∞	∞	∞	∞	∞	∞	17.17	5.85
8.0	1.74	9.14	-	∞	∞	∞	∞	∞	∞	∞	∞	9.63
8.5	1.85	9.71	-	∞	∞	∞	∞	∞	∞	∞	∞	28.47
<i>Condenser temperature -20 °C</i>												
2.5	0.42	1.93	∞	22.43	2.41	1.73	1.49	1.37	1.30	1.25	1.21	1.19
3.0	0.50	2.32	∞	∞	3.65	2.08	1.68	1.49	1.39	1.32	1.27	1.24
3.5	0.58	2.70	∞	∞	8.09	2.63	1.92	1.64	1.49	1.40	1.34	1.29
4.0	0.67	3.09	∞	∞	∞	3.65	2.27	1.83	1.62	1.49	1.41	1.35
4.5	0.75	3.47	∞	∞	∞	6.17	2.78	2.08	1.77	1.60	1.49	1.42
5.0	0.83	3.86	∞	∞	∞	22.43	3.65	2.41	1.96	1.73	1.59	1.49
5.5	0.91	4.24	∞	∞	∞	∞	5.41	2.90	2.21	1.89	1.70	1.58
6.0	1.00	4.63	∞	∞	∞	∞	10.83	3.65	2.53	2.08	1.83	1.68
6.5	1.08	5.02	-	∞	∞	∞	∞	5.00	2.98	2.32	1.99	1.79
7.0	1.16	5.40	-	∞	∞	∞	∞	8.09	3.65	2.63	2.18	1.92
7.5	1.25	5.79	-	∞	∞	∞	∞	22.43	4.75	3.05	2.41	2.08
8.0	1.33	6.17	-	∞	∞	∞	∞	∞	6.86	3.65	2.71	2.27
8.5	1.41	6.56	-	∞	∞	∞	∞	∞	12.69	4.57	3.11	2.50
<i>Condenser temperature -10 °C</i>												
2.5	0.32	1.35	∞	2.58	1.62	1.39	1.28	1.22	1.18	1.15	1.13	1.12
3.0	0.38	1.62	∞	4.25	1.90	1.52	1.37	1.28	1.23	1.19	1.17	1.15
3.5	0.45	1.89	∞	14.01	2.30	1.68	1.46	1.35	1.28	1.24	1.20	1.18
4.0	0.51	2.16	∞	∞	2.96	1.90	1.58	1.43	1.34	1.28	1.24	1.21
4.5	0.57	2.43	∞	∞	4.25	2.18	1.72	1.52	1.41	1.33	1.28	1.25
5.0	0.64	2.70	∞	∞	7.84	2.58	1.90	1.62	1.48	1.39	1.33	1.28
5.5	0.70	2.97	∞	∞	73.20	3.20	2.12	1.75	1.56	1.45	1.38	1.32
6.0	0.77	3.24	∞	∞	∞	4.25	2.40	1.90	1.66	1.52	1.43	1.37
6.5	0.83	3.51	∞	∞	∞	6.45	2.80	2.08	1.77	1.60	1.49	1.41
7.0	0.89	3.78	∞	∞	∞	14.01	3.36	2.30	1.90	1.68	1.55	1.46
7.5	0.96	4.05	∞	∞	∞	∞	4.25	2.58	2.05	1.78	1.62	1.52
8.0	1.02	4.32	-	∞	∞	∞	5.84	2.96	2.23	1.90	1.70	1.58
8.5	1.08	4.59	-	∞	∞	∞	9.50	3.48	2.45	2.03	1.79	1.65
<i>Condenser temperature 0 °C</i>												
2.5	0.25	0.97	29.73	1.71	1.36	1.24	1.18	1.15	1.12	1.10	1.09	1.08
3.0	0.29	1.17	∞	2.05	1.48	1.31	1.23	1.18	1.15	1.13	1.11	1.10
3.5	0.34	1.36	∞	2.61	1.62	1.39	1.28	1.22	1.18	1.15	1.13	1.12

Table 1, continued

1	2	3	4	5	6	7	8	9	10	11	12	13
4.0	0.39	1.56	∞	3.65	1.81	1.48	1.34	1.26	1.21	1.18	1.16	1.14
4.5	0.44	1.75	∞	6.34	2.05	1.58	1.40	1.31	1.25	1.21	1.18	1.16
5.0	0.49	1.95	∞	29.73	2.39	1.71	1.48	1.36	1.29	1.24	1.21	1.18
5.5	0.54	2.14	∞	∞	2.87	1.86	1.56	1.42	1.33	1.27	1.23	1.20
6.0	0.59	2.34	∞	∞	3.65	2.05	1.66	1.48	1.38	1.31	1.26	1.23
6.5	0.64	2.53	∞	∞	5.07	2.29	1.77	1.55	1.42	1.35	1.29	1.25
7.0	0.69	2.73	∞	∞	8.53	2.61	1.90	1.62	1.48	1.39	1.33	1.28
7.5	0.74	2.92	∞	∞	29.73	3.03	2.05	1.71	1.54	1.43	1.36	1.31
8.0	0.79	3.12	∞	∞	∞	3.65	2.24	1.81	1.60	1.48	1.40	1.34
8.5	0.84	3.31	∞	∞	∞	4.61	2.47	1.92	1.67	1.53	1.44	1.37

Note. The symbol “∞” indicates that the system does not work on ammonia; the dash “-” means that the system uses neither carbon nor ammonia as the working fluid; H is the condenser height above the evaporator, m; Δ_{CO_2} and Δ_{am} are the differences in the condenser and ground temperatures for the system working on carbon dioxide and ammonia, respectively, °C; t_{gr} is the ground temperature, °C; t_{air} is the air temperature, °C. The values for H are usually in the range from 2.5 to 6.0 m ($H < 2.5$ m not occurred in practice); for the *Fundament.Sroi.Arkos* systems $H = 6$ m.

CALCULATIONS

The system’s capacity (heat output) is expressed by the following expression [Anikin, Spasennikova, 2014]:

$$W = (t_c - t_{\text{air}})S\eta\alpha = \left((t_c - t_{\text{gr}}) + (t_{\text{gr}} - t_{\text{air}}) \right) S\eta\alpha, \quad (1)$$

where t_c is the condenser temperature; t_{gr} is the ground temperature at the interface with the evaporator tube; t_{air} is the air temperature; S is the total area of the finned section; η is the coefficient of efficiency of the condenser fins; α is the heat transfer coefficient for the fins;

$$W_{\text{am}} = \left(-\Delta_{\text{am}} + (t_{\text{gr}} - t_{\text{air}}) \right) S\eta\alpha; \quad (2)$$

$$W_{\text{CO}_2} = \left(-\Delta_{\text{CO}_2} + (t_{\text{gr}} - t_{\text{air}}) \right) S\eta\alpha; \quad (3)$$

for ammonia $(t_c - t_{\text{gr}}) = -\Delta_{\text{am}}$, for carbon dioxide $(t_c - t_{\text{gr}}) = -\Delta_{\text{CO}_2}$.

The values for Δ_{CO_2} , Δ_{am} are calculated using the formula [Anikin, Spasennikova, 2014]

$$\Delta_{\text{CO}_2/\text{am}} = \frac{\rho_L g H}{dP_{\text{sat}}/dt},$$

where ρ_L is the liquid coolant density at a specified temperature; g is gravity; P_{sat} is the pressure of saturated vapors at a specified temperature; H is the condenser height above the evaporator.

By dividing (3) by (2), we obtain

$$\frac{W_{\text{CO}_2}}{W_{\text{am}}} = \left[1 - \frac{\Delta_{\text{CO}_2}}{t_{\text{gr}} - t_{\text{air}}} \right] \left[1 - \frac{\Delta_{\text{am}}}{t_{\text{gr}} - t_{\text{air}}} \right]^{-1}.$$

The condition to be fulfilled for the ground freezing is: $t_{\text{air}} < t_{\text{gr}}$.

Table 1 shows the ratios of heat outputs (i.e. the systems’ capacities) for carbon dioxide and ammonia at different condenser temperatures, taking into account difference in ground and air temperature temperatures, and the distance between the evaporator and the condenser.

It follows from Table 1 that if the system works both on carbon dioxide and ammonia, the capacity of this system charged with carbon dioxide is always greater as compared to its using ammonia as the working fluid.

CONCLUSIONS

It has been shown that the thermal capacity of an HET system working on carbon dioxide is always higher than the capacity of the same system using ammonia as the working fluid. This primarily is explained by the fact that the derivative of saturated vapor pressure with respect to temperature is always higher for carbon dioxide than for ammonia. As the distance between the evaporator and the condenser increases with affiliated increase in hydrostatic pressure, the ratio of hydrostatic pressure to the derivative of saturated vapor pressure with respect to temperature for carbon dioxide is therefore also always less than for ammonia.

With an increase in the condenser temperature, the region where the system works neither on carbon dioxide nor ammonia explicitly decreases. The system charged with carbon dioxide works at a greater distance between the condenser and the evaporator at a 1 °C difference between ground and air temperatures, while it fails to operate on ammonia.

The work was fulfilled within the state-commissioned R&D project (AAAA-17-117051850061-9).

References

- Anikin, G.V., 2009. Simulating the Operation of Cooling Systems with Horizontal Tubes. Moscow, Deposited at VINITI, 30.10.2009, No. 674-B2009 (in Russian).
- Anikin, G.V., Plotnikov, S.N., Spasennikova, K.A., 2011. Computer simulation of heat- mass exchange in the systems of horizontal ground cooling. *Kriosfera Zemli (Earth's Cryosphere)*, XV (1), 33–39.
- Anikin, G.V., Spasennikova, K.A., 2014. On the choice of refrigerating fluid type “GET” systems for seasonal cooling. *Earth's Cryosphere XVIII* (2), 26–28.
- Melnikov, V.P., Anikin, G.V., Ishkov, A.A., et al., 2017. Maximum and minimum critical thermal loads constraining the operation of thermosyphons with horizontal evaporator tubes (HET). *Earth's Cryosphere XXI* (3), 38–44.

Received July 24, 2019

Revised version received November 6, 2019

Accepted November 19, 2019

METHODS OF CRYOSPHERIC RESEARCH

DOI: 10.21782/EC2541-9994-2020-2(45-59)

THE STRUCTURE OF PERMAFROST WITHIN PARISENTO STATION
(GYDAN PENINSULA) FROM GEOPHYSICAL DATAD.S. Pankova^{1,2}, V.V. Olenchenko^{1,3}, L.V. Tsibizov^{1,3}, Y.K. Kamnev⁴, A.N. Shein³, A.I. Sinitskiy⁴¹ Novosibirsk State University, 2, Pirogova str., Novosibirsk, 630090, Russia; Pankova.geo@gmail.com² St. Petersburg State University, Institute of Earth Sciences, 33-35, 10th Line V.O., St. Petersburg, 199178, Russia³ Trofimuk Institute of Petroleum Geology and Geophysics, SB RAS,

3, Acad. Koptuyug ave., Novosibirsk, 630090, Russia; OlenchenkoVV@ipgg.sbras.ru

⁴ Arctic Research Center of the Yamal-Nenets autonomous district, 73, Respublika str., Salekhard, 629008, Russia

In this article the results of geoelectric survey investigations of permafrost in the area of Parisento station (Gydan Peninsula) are presented. According to the electromagnetic sounding data, the permafrost thickness is 210–300 m. Application of electrical resistivity tomography (ERT) has revealed, that massive ice stratum is characterized by extremely high electrical resistivity, exceeding million Ohm·m. It confines method's sensitivity below depths of 50–75 m. Fixing the depths of deep-lying conducting layers, determined by electromagnetic sounding, has insignificant effect on error of ERT inversion. However, the input of the layers with a fixed-by-depth electrical resistivity has lead to an improvement of the model for geological interpretation. It has been determined, that the massive ice between the Krugloye and Parisento Lakes does not have continuous distribution, as it was previously appeared according to drilling data. A linear area of low electrical resistivity has been identified, which is probably due to paleo-channel connecting the lakes in the past. By numerical simulation of thermal fields, a closed talik (up to the depth of 140 m) has been identified under Krugloye Lake, and an open one has been revealed under Parisento Lake. The influence of three-dimensional conductive heterogeneities, as a lake talik and a lake, on the electrical resistivity distribution in the two-dimensional and three-dimensional geoelectrical models has been considered.

Parisento station, permafrost, electrical resistivity tomography, transient electromagnetic sounding, resistivity, massive ice, lake, talik

INTRODUCTION

The Gydan Peninsula is one of the least developed and poorly explored areas. In order to realize the plans of environmentally safe industrial development of Tazovskiy District of Yamalo-Nenets Autonomous Okrug (YaNAO), it is necessary to assess the current state of permafrost, and to organize the monitoring of its transformation under the influence of climatic changes, as well as the human impact in all geographical subzones of the peninsula. That will allow to improve the design technology of field facilities and the systems of raw hydrocarbon transportation, situated in harsh engineering-geocryological conditions, to ensure their mechanical safety and reduce geotechnical risks by improving the efficiency of design decisions in the field of development of measures for the implementation of technologies for temperature stabilization of the foundation soils, geotechnical monitoring and other innovative technologies.

In 1970–1990s geocryological structure of the Yamal and the Gydan peninsulas was studied by the

researchers from the Moscow State University (MSU) [Badu, Trofimov, 1974], the Production Scientific and Research Institute of Engineering Surveying in Construction (PNIIS) [Baulin, 1985], the All-Russian Research Institute of Hydrogeology and Engineering Geology (VSEGINGEO) [Anisimova, Kritsuk, 1983; Kritsuk, Polyakov, 1989]. The overview and small-scale maps have been compiled. Geotechnical conditions of the Gydan Peninsula, including exogenous and geological processes and phenomena, have been described [Trofimov et al., 1986].

The comprehensive study at the Gydan Peninsula has been carried out in the vicinity of the Parisento station of VSEGINGEO, near the eponymous lake in the middle reaches of Yuribey River. The station was founded by V.A. Dubrovin in 1982 in order to organize monitoring of the cryogenic processes and phenomena dynamics in the undeveloped but prospective area. It represented a scientific station along with the landfills within which a stationary network

The English text is published as edited by the authors.

of reference plots had been deployed. During the operation of the station, the geocryological features of the region have been studied in detail, and such the climatic characteristics of the territory as air temperature, wind speed, snow depth and average insolation have been monitored. According to measurements carried out in three boreholes, the temperature regime of the upper part of the permafrost section have been determined up to the depth of 73.5 m, and the beds of massive ice, having thickness up to 32 m, have been drilled-in. The permafrost was studied by using such geophysical methods as vertical electrical sounding, high-frequency electric profiling and electrical well-logging.

In 1995, due to the termination of funding, research works within the station had been stopped, and the station itself had been mothballed. 20 years later, the government of Yamalo-Nenets Autonomous Okrug raised a question of the necessity to resume environmental monitoring of the permafrost zone before the intensive development of the North regions by the oil and gas producing companies. In August 2016 and in August 2017, the Arctic Research Center (Salekhard) organized comprehensive scientific expeditions to the Parisento station with the participation of specialists from the Trofimuk Institute of Petroleum Geology and Geophysics SB RAS (Novosibirsk).

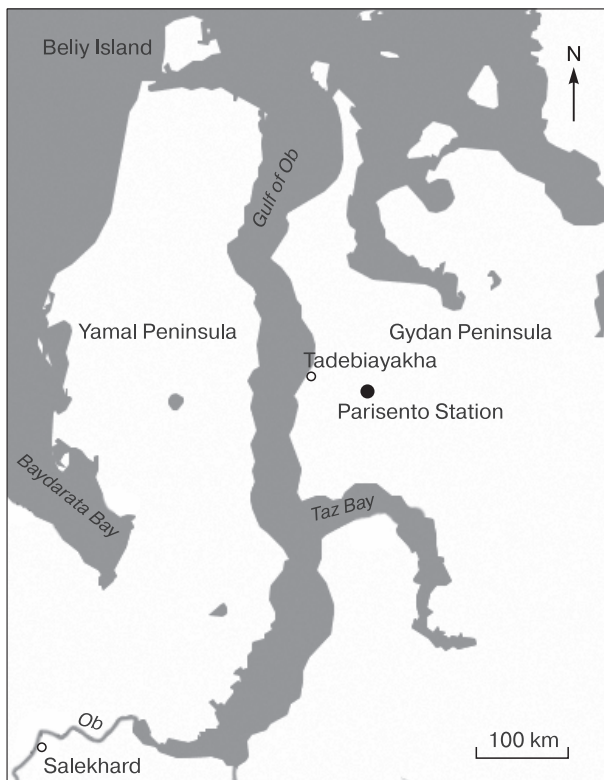


Fig. 1. Location map of the Parisento Station.

The main aim of the expeditions was to assess the current state of permafrost within the station according to geological, geomorphological and geocryological studies, as well as to obtain new information on the permafrost structure using modern geophysical technologies, which have been developed significantly over the past 20 years. Such geoelectrical methods as vertical electrical sounding in the modification of electrical resistivity tomography (ERT) and near-field time-domain electromagnetic (TDEM) sounding were applied in the research. Those methods are widely used in permafrost research, for instance, for detecting of massive ice beds [Everest, Bradwell, 2003; Hauck et al., 2003], delineation of the permafrost distribution area and determination of its thickness [Hauck, Mühlh, 2003; Olenchenko et al., 2011; You et al., 2013], determination of active layer depths and talik thickness [McClymont et al., 2013; Kozhevnikov et al., 2014; Fague et al., 2016].

The main objectives of geophysical research carried out in the area of the Parisento station were to determine the permafrost thickness, and to define its structural features.

STUDY AREA

The Parisento station is located in the Tazovsky District of Yamalo-Nenets Autonomous Okrug, in the central part of the Gydan Peninsula, at the latitude of 70.1° N (Fig. 1). The nearest settlement is Tadebiayakha, which is situated in 64 km to the north-west of the station, on the coast of the Gulf of Ob.

The mean annual air temperature is -11.2°C , according to the results of the regime observations of the VSEGINGEO in 1985–1990. The research area belongs to the zone of continuous permafrost distribution. Its thickness varies from 200 to 300 m, and the temperatures of frozen ground is up to -8°C . The thickness of active layer varies significantly: from 55–65 cm (on polygonal peatlands) up to 170–180 cm (on bare-of-vegetation sandy deflation-flats). Ice content of the frozen ground can reach 90 %.

The surface of the Late Quaternary coastal plain with altitudes of 10–46 m occupies a dominant position in the topography around the Parisento station. The areas with high lake percentage (up to 40 %) are developed within the plain. Drained lakes basins (khasyreys) are usually confined to gently undulating landforms. Parisento Lake is the largest water body in the vicinity of the Parisento station. Its water surface size is 6×4 km and the maximum depth is 35 m. Krugloye Lake, smaller by the size, is located to the north of Parisento Lake, and Geofizicheskoye Lake is situated even more to the north of it. Massive ice bed, which has been drilled-in by boreholes, is the unique object within the Parisento station (Fig. 2). Its thickness according to the boreholes data is up to 32 m and the minimum temperature is -8°C at a depth of

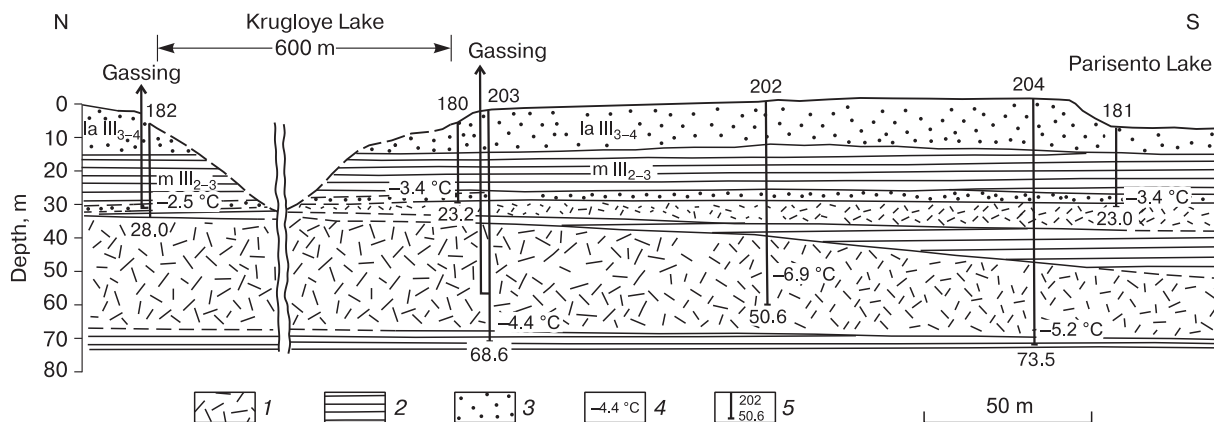


Fig. 2. Geological section of study site according to the VSEINGEO data.

1 – ice; 2 – clay with inclusions of ice; 3 – frozen sand; 4 – permafrost temperature (°C); 5 – borehole, its number and depth (m).

10 m. Taking into account the fact that massive ice bed has been stripped by a limited number of boreholes, the boundaries of its distribution remain to be uncertain. A description of the sediments at the borehole 204, located at a distance of 15 m from the edge of the Parisento Lake scarp is presented below:

0.0–15.9 m – light-gray sand, obscurely-layered, the bedding is due to the presence of plant residues, interlayers of clay, ice, peat, sandy loam; the ground is frozen from a depth of 0.6 m; there are sections (up to 1 m in thickness) of pure ice;

15.9–27.8 m – obscurely-layered and varved, icy clay (loam); there is pure ice in some intervals;

27.8–30.3 m – fine sand to silty sand with isometric inclusions of ice and bands of sandy loam and clay;

30.3–36.7 m – mostly pure and transparent ice, with sparse inclusions of dark gray clay and sandy loam;

36.7–48.05 m – dark gray to black clay, mostly homogeneous, cross-bedded due to interlayers of lighter clay and silty loam, sometimes with separate ice lenses; from a depth of 42.2 m, the ice content increases sharply;

48.05–70.2 m – mostly clear and transparent ice, with a lot of air bubbles and the inclusions of clay;

70.2–73.5 m – icy dark gray clay; deeper than 72.0 m, the ice content decreases, the clay acquires a greenish tint and some plasticity (probably due to increased salinity).

METHODS

Such geophysical methods as near-field time-domain electromagnetic sounding (TDEM) and vertical electrical sounding in the modification of electrical resistivity tomography (ERT) have been applied in two study sites (Fig. 3).

The Site I is located between the Krugloye and Geofizicheskoye lakes. The TDEM method measurements have been performed on a 65 × 65 m network inside ten transmitter loops 200 × 200 meters in size, using Fast-Snap equipment (NPK Sibgeosystems LLC, Russia). The PDI-50 induction sensor with an effective moment, which is equivalent to a loop of 50 × 50 m in size, has been used as a receiver. It was installed inside each transmitter loop with a uniform

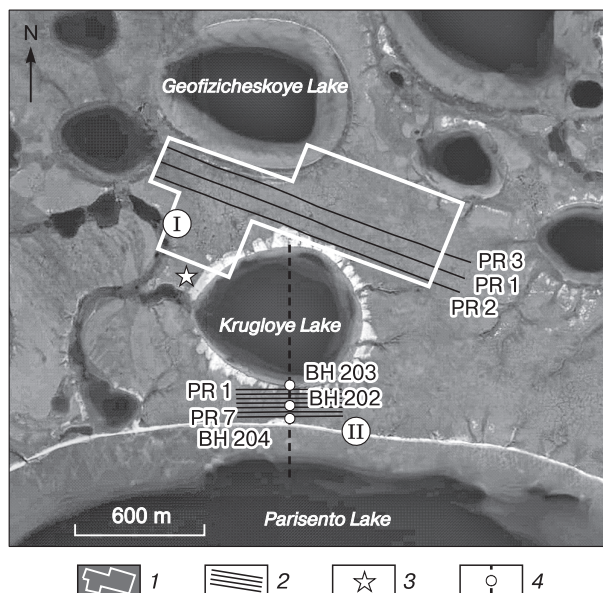


Fig. 3. Layout of the geophysical prospecting profiles:

1 – contour of the near-field time-domain electromagnetic sounding area; 2 – profiles of the electrical resistivity tomography method; 3 – Parisento Station; 4 – the line of geological section through boreholes and position of boreholes 202, 203, 204; I, II – number of study site.

mesh. A similar technique of electromagnetic sounding is effective in area studies. Furthermore, when the size of the generator loop is 200×200 m, the effect of the induced polarization of the upper part of the section on the transient process is minimized. The contour of the study area by means of the TDEM sounding method is displayed in Fig. 3. The subsequent quantitative interpretation of the TDEM sounding data has been carried out using the TEM-IP program, developed at the Trofimuk Institute of Petroleum Geology and Geophysics, Siberian Branch of the Russian Academy of Sciences (IPGG SB RAS) [Antonov *et al.*, 2014]. The inverse problem of electromagnetic sounding has been solved within the framework of a one-dimensional horizontally-layered model without taking into account the induced polarization of the upper part of the section with high ice content. The weak influence of the upper layers on the process of electromagnetic field formation was noted already at 0.04 ms as a low-amplitude minimum on the electromotive force (EMF) curve (or a small maximum on the apparent resistivity curve). Therefore, before interpretation, the field formation curve had been cut off to the EMF values for a time of 0.1 ms, as well as in the noise areas at the “tails” of the curves after a time cutoff of 50 ms. The error in approximating of the experimental curve to the theoretical dependence for the upper icy part of the section was 1–3 %. The multi-electrode electrical prospecting station Skala-48, developed at IPGG SB RAS, was used for measurements by the ERT method. Further data processing was performed with using the programs Res2D-inv and Res3Dinv (Geotomo Software) [Loke, 2009].

In the Site I, the ERT method soundings have been implemented on three profiles of 1425 meters

long with the measurement spacing along the profile of 10 m. The distance between the ERT profiles was 65 m. The sequence of the electrode connecting corresponded to the pole-dipole arrays with a maximum span between the current electrodes A or B and the center of the receiving line MN equal to 430 m.

The Site II was located between the Krugloye and Parisento lakes, where in the 1990s a borehole-profile had been driven, and the thick massive ice bed had been drilled-in. In that site, the ERT soundings have been carried out on 7 profiles of 470 m long each, the distance between profiles was 25 m, the measurement spacing was 10 m, and the pole-dipole array was applied.

The wet surface of the tundra provided a low level of grounding resistance, and the absence of industrial electromagnetic interference made it possible to obtain high-quality data. The current strength in the AB circuit was 10–40 mA, and the voltage at the receiving electrodes varied from 4 to 5000 mV. The instrumental error of one measurement of the apparent resistivity at maximum electrode spacing, calculated by the Skala-48, did not exceed 0.2 %. The scheme of the electrotomography profiles arrangement is demonstrated in Fig. 3.

RESULTS

The solution of the inverse problem for the TDEM method data has been carried out in the framework of the three-layer, four-layer, five-layer, and six-layer models. As a result, it has been determined that the four-layer model of a medium, combining the equivalent layers of more complex models, is optimal. Figure 4 shows an example of the experimental and theoretical curves of apparent electrical resistivity (ρ_a) and the one-dimensional geoelectric model corresponding to the theoretical curve, including the resistivity of each layer (ρ), thickness (h), and roof depth (z). The mean-square error of selection, in that case, was 3 %.

In the model, layer No. 1 of high resistivity includes the sediments represented by sands and massive ice. Its thickness is estimated at 64 m, which is consistent with the drilling data (Fig. 2). Layer No. 2 with a resistivity of 51.8 Ohm·m is interpreted as frozen loam. At a depth of 133 m, the resistivity of the sediments decreases to 10.4 Ohm·m, which the authors attribute to an increase in the salinity of loams. In the base of the section, at a depth of 249.5 m, layer No. 4 stands out with a very low resistivity of 4.2 Ohm·m. It is assumed that the boundary between layer No. 3 and No. 4 is the boundary of the water-ice phase transitions.

Figure 5 demonstrates the geoelectric section compiled according to the TDEM method results obtained on Site I along the line coinciding with the

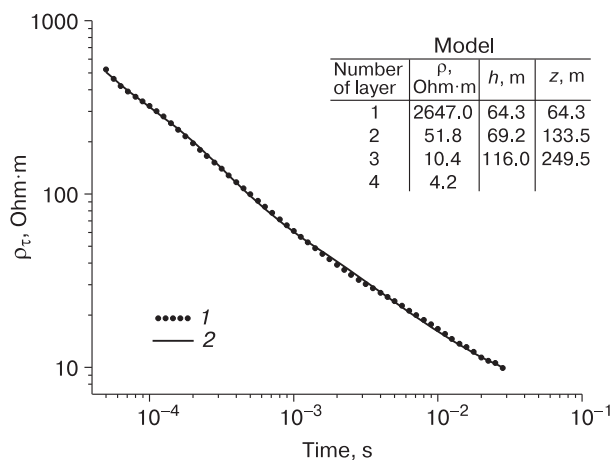


Fig. 4. Experimental (1) and theoretical (2) curves of apparent resistivity at the near-field time-domain electromagnetic sounding point No. 501, and corresponding one-dimensional models of section.

See explanations in the text.

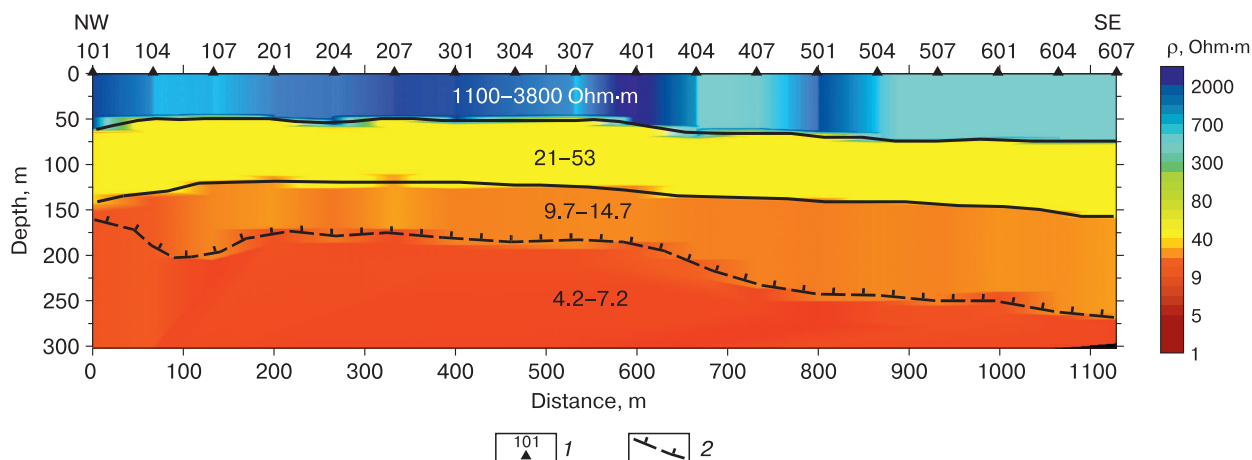


Fig. 5. Geoelectric section according to the near-field time-domain electromagnetic sounding:

1 – point of electromagnetic sounding; 2 – supposed boundary of the water–ice phase transitions.

profile line No. 3 in the ERT method. In the upper part of the section, up to the depth of 50–75 m, a highly-resistive layer (with the electrical resistivity varying from 1100 to 3800 Ohm·m) is distinguished. Those highly-resistive deposits are represented by frozen sand and loam with interlayers of massive ice.

At depths below than 50–75 m, a layer with reduced resistivity of 21–53 Ohm·m – probably due to an increase in the salinity of the section in the Upper Quaternary coastal-marine sediments of the Kazantsevo Formation – has been identified. Below the depth of 120–150 m, the resistivity of the sediments decreases up to 9.7–14.7 Ohm·m, which caused by an increase in the mineralization of porous water in Mid-Quaternary marine sediments of the Salekhard Formation. At the depth 160–260 m the upper border of the underlying layer with very low resistivity (4.2–7.2 Ohm·m) has been noted. It is assumed that the layer is the lower border of permafrost, which is consistent with other studies [Trofimov, Baulin, 1984]. Similar resistivity values of saline loam at the phase transition boundary have been mentioned in the papers [Krylov, Bobrov, 1995; Zykov, 2007].

The section in the Figure 5 illustrates horizontally-stratified structure of the medium with decrease of sediments resistivity by depth from several thousands to several Ohm·m. The upper part of the section is represented by high-resistive frozen medium with interlayers of massive ice. Reduced resistivity of underlying frozen ground is explained by their salinity. According to the near-field time-domain electromagnetic sounding, the bottom of permafrost is supposed to be at the depths of 200–300 m.

A feature of the section is the plunge of permafrost bottom along the profile to the southeast. Using the data of areal soundings, the map of the permafrost bottom depth has been compiled (Fig. 6). On the

isthmus between the lakes, permafrost thickness reduced up to 150 m. That may be associated both with the warming effect of lake taliks, and with the influence of three-dimensional conductive heterogeneity on the result of one-dimensional inversion of the TDEM sounding data.

Geoelectric sections of the Site I (according to the ERT data) are presented in Fig. 7. The number of iterations of model selection for each profile was 5, while the standard deviation (SD), characterizing the selection error, varied from 4 % (profile 1) and 4.8 % (profile 2), to 9.3 % (profile 3) depending on quality of the input data.

An analysis of geoelectrical sections reveals that the layer of very high-resistive deposits is traced at depths of 10–90 m. That part of the medium consists of sand and loam with high contents of frozen porous

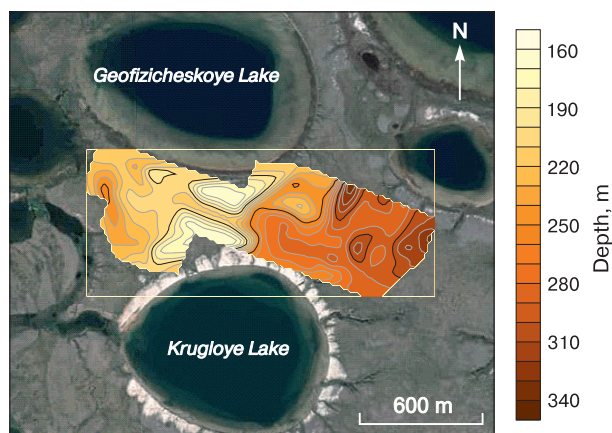


Fig. 6. Map of the permafrost base according to the near-field time-domain electromagnetic sounding data.

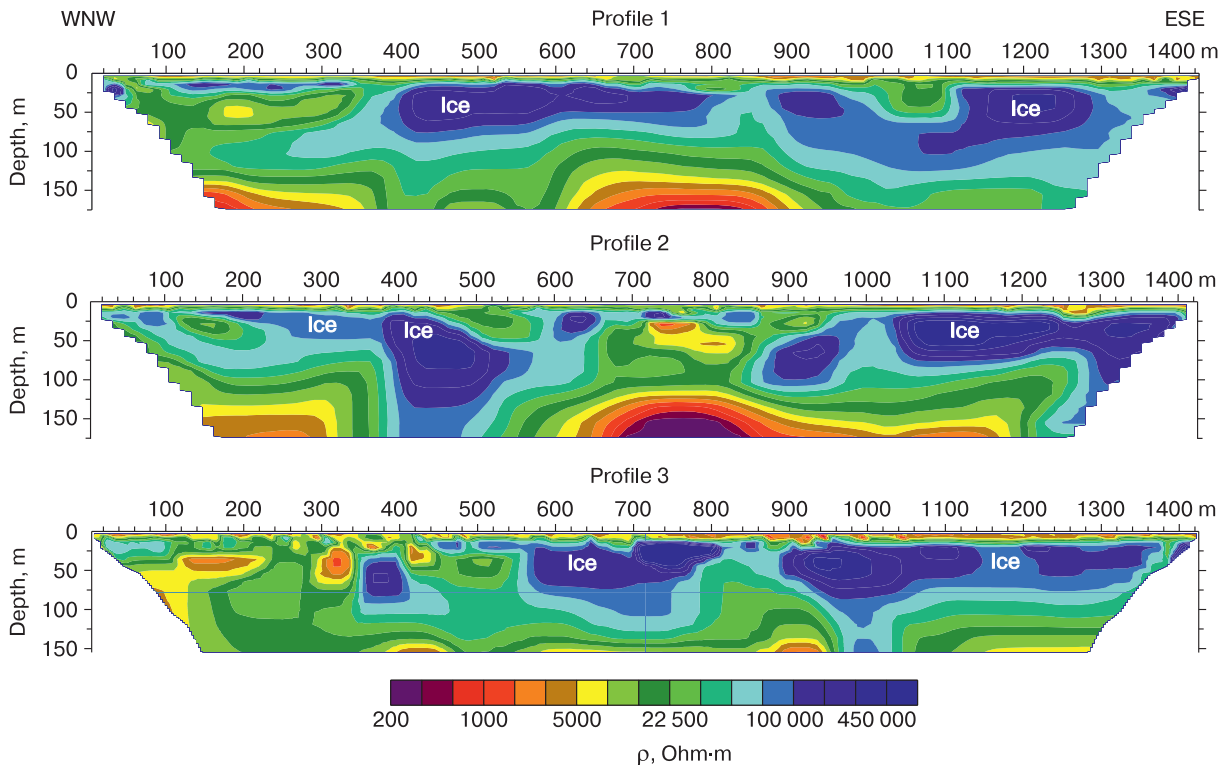


Fig. 7. Geoelectric sections according to the electrical resistivity tomography data.

low-mineralized water. It should be noted that the deposits resistivity, measured at quasi-direct current applying in the course of the electrical resistivity tomography, is significantly higher than the resistivity determined according to the near-field time-domain electromagnetic sounding data. So, for example, the upper part of the section has an electrical resistivity of hundreds of thousands Ohm·m and in some cases it exceeds a million Ohm·m. The deposits having resistivity of 10^5 – 10^6 Ohm·m are interpreted as massive ice.

The electrical resistivity of the frozen sediments is affected by their temperature, lithological composition, ice content and salinity. In addition, the distribution of resistivity in the geoelectric sections, constructed by two-dimensional inversion, depends on the influence of three-dimensional heterogeneities of the geological medium, situated aside from the profile. Therefore, during the interpretation of geoelectrical sections it is necessary to take into account the profile location with respect to such three-dimensional heterogeneities as lakes. At the same time, the nearness of the lakes also determines the geocryological conditions. For example, the north-western part of profile 3 in the interval of 100–500 m runs along the shore of Krugloye Lake (Fig. 3). Sediments of very high resistivity haven't been detected in that section of the profile (with the exception of the local anomaly at a depth of 380 m), which indicates the absence of massive ice. A reduced resistivity (up to

250–300 Ohm·m) has been observed along the intervals of 650–900 m on profile 1 (deeper than 25 m) and profile 2 (deeper than 100 m). Profile No. 2 in the intervals of 700–850 m runs 45 m aside from Krugloye Lake. We believe that abnormally low values of resistivity at depths on profiles 1 and 2 are due to the lateral influence of the Krugloye Lake talik, and the anomalies do not reflect the real geologic section.

Despite the fact that the two-dimensional geoelectrical model has been obtained up to a depth of 175 m as a result of inversion, and the standard deviation during solving the inverse problem was 4–9.3 %, one should be careful to trust the data obtained from depths over 60 meters. By means of the Res2Dinv program (version 3.55), using as an example the data of profile 1, the sensitivity of the blocks used in the inversion model has been estimated (Fig. 8). The value of normalized sensitivity (S_n) determines the amount of information about the resistivity of the model block, which is contained in the measured data, and varies from 0 to 1. The higher the value of normalized sensitivity, the more well-grounded is the model resistivity. Near-surface blocks usually have higher sensitivity than deeper ones, since the normalized sensitivity function takes on very high values near the electrodes [Loke, 2009].

As it is demonstrated in Fig. 8, the sensitivity of ERT method decreases sharply with depth if there is massive ice bed in a section. For example, in the pro-

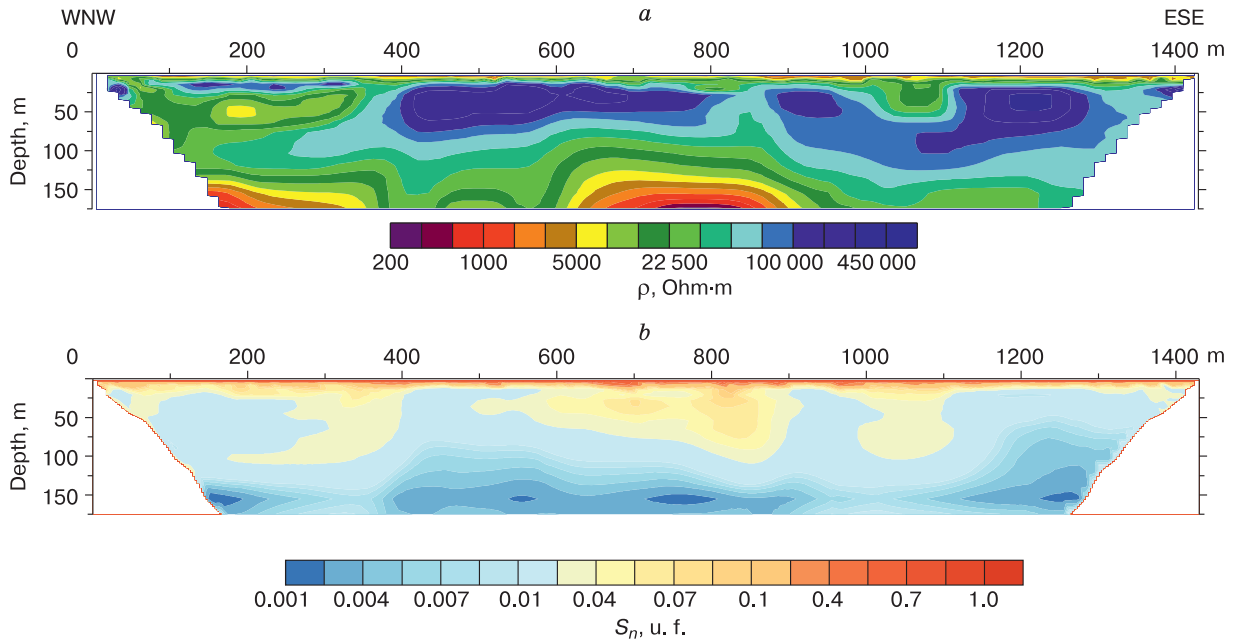


Fig. 8. Geoelectric section (a) and section of normalized sensitivity (S_n) of model blocks (b) along profile 1.

file intervals at the distances of 400–500 m and 1100–1300 m from the beginning of the profile, electrical current does not penetrate under objects of very high (more than 100 kOhm·m) resistivity, and the sensitivity of the method is limited to the first meters. The sensitivity increases to the depth of 50–75 m in areas where the resistivity of the medium decreases up to values of less than 100 kOhm·m.

According to the results of the TDEM method, in the section along profile 1, at the depth of 60–90 m, the roof of the low resistivity layer (about 30 Ohm·m) has been identified, as well at a depth of 140–220 m, the top of layer with resistivity on the order of 8 Ohm·m has been detected. Those layers have been inserted, as layers with fixed resistance, in the electrotomography data by profile 1. After that, the inverse problem has been solved. As a result, the section

(shown in Fig. 9) has been compiled. After completing 5 iterations, standard deviation was 4 %, i.e. the insertion of two layers with fixed resistivity has not affected the model selection error. That confirms the weak sensitivity of the ERT method to changes in resistivity of soils lying deeper than 50–75 m. At the same time, the introduction of layers with fixed resistivity at certain depths lead to a change in the geoelectrical structure of the upper part of the section within the depth range of 0–90 m. For example, such structural features of the section as a thin layer of high resistivity has become more pronounced in the profile interval of 0–400 m, and the anomalies caused by massive ice have acquired an elongated shape.

Two-dimensional data of the ERT soundings have been combined into the three-dimensional data set. After completing that, the thickness and electrical

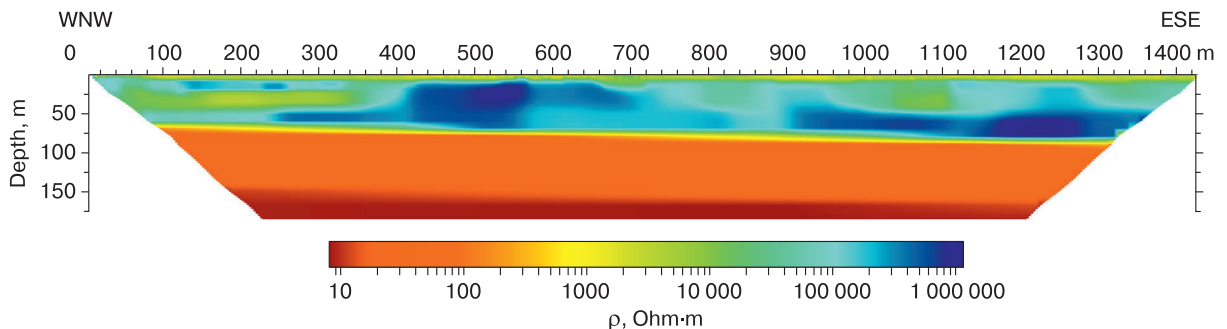


Fig. 9. Geoelectric section along profile 1, constructed as a result of two-dimensional inversion of electric tomography data with fixed layers, with a known position of the layer roof and electrical resistivity according to the TDEM data.

resistivity of the low-resistive layers selected according to the TDEM sounding data have been affixed in that data set, after which three-dimensional inversion has been carried out using Res3Dinv software.

Figure 10 displays a three-dimensional model of the resistivity distribution in the Site I according to the ERT data, on which an anomaly of high electric resistivity caused by massive ice is displayed by means of the isosurface corresponding to 100 kOhm·m. In the northwestern part of the site the anomaly decreases in size and wedges out as massive ice bed approaches Krugloye Lake. Influence of Krugloye Lake on the geoelectric model is also expressed in the wedging out of a high-resistive layer, located near the lake (Fig. 10). That may be due to both local lithologic heterogeneity, which can be seen on the satellite image at the shoreline of the lake near the profile, and the lateral effect of the lake on distribution of electrical current in the medium. A three-dimensional model of the resistivity distribution in the medium allows us to visualize the structure of the study site and to outline the wedging out of massive ice bed in the vicinity of Geofizicheskoye Lake.

As a result of the ERT sounding method at the Site I, the following has been established. The deposits of the upper part of the section up to the depth of 75 m have a very high resistivity, reaching hundreds of thousands of Ohm·m, and in some cases exceeding one million Ohm·m. High resistivity of the sediments can be explained by their lithological composition

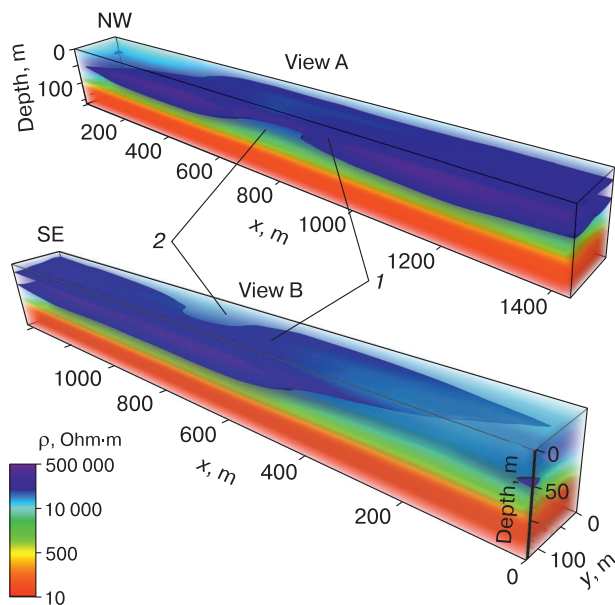


Fig. 10. Three-dimensional geoelectric model according to the electrotomography data:

1 – electrical-resistivity isosurface of 100 kOhm·m; 2 – wedging-out of high-resistive layer nearby Krugloye Lake. View of the geoelectric model from the southern (A) and northern (B) sides.

(sands and loams) and low mineralization of the frozen porous water. The highest resistivity values are characteristic for massive ice beds. Such a high level of electrical resistivity prevents the penetration of electrical current into the depths, as a result of which the sensitivity of the method is limited to a depth of 50–75 m. Under the layers with a resistivity of more than 100 kOhm·m, the sensitivity of the method is confined by the depth of the top of those layers.

The introduction of layers with a fixed resistivity and a depth, established according to the TDEM sounding data, into the two-dimensional ERT model does not lead to a change in selection error when solving the inverse problem. That confirms the insensitivity of the ERT method to properties of the sediments occurring deeper than 60 m.

In the three-dimensional model of the resistivity distribution in the medium, nearby the Krugloye and Geofizicheskoye lakes, the regular wedging-out of an abnormally-high-resistivity layer has been noted. That may be due either to thawing out of massive ice in the vicinity of the lakes, or to the lateral influence of three-dimensional conductive heterogeneity on the distribution of electrical current in the medium. In the Site II, situated between the Parisento and Krugloye lakes, profile 3 runs through the borehole 202. A geoelectrical section along the profile 3 is demonstrated in Fig. 11. The inversion of data has been performed with the fixation of resistivity and border of loam from the depth of 57 m, determined according to the drilling data (Fig. 2).

The level of electrical resistivity of the deposits, established by the ERT method, is in good agreement with the archival data of lateral logging sounding. Out of comparison of the geoelectrical section with the drilling data, it follows that the layers of anomalously high resistivity correspond to massive ice, as well as to the sediments with high ice content. However, in the

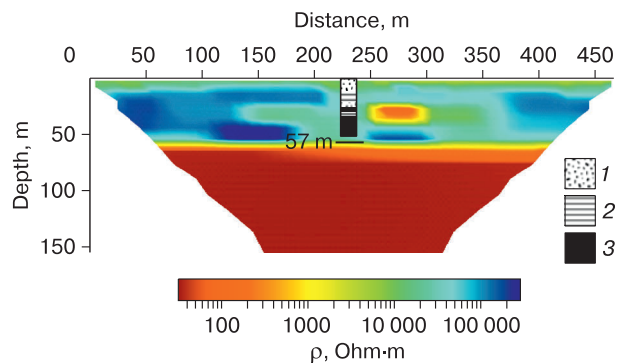


Fig. 11. Geoelectric section along profile 3 through borehole 202.

Two-dimensional inversion with fixed layers: 1 – sand; 2 – clay with ice inclusions; 3 – ice. Number of iterations – 5; standard deviation – 5.9 %.

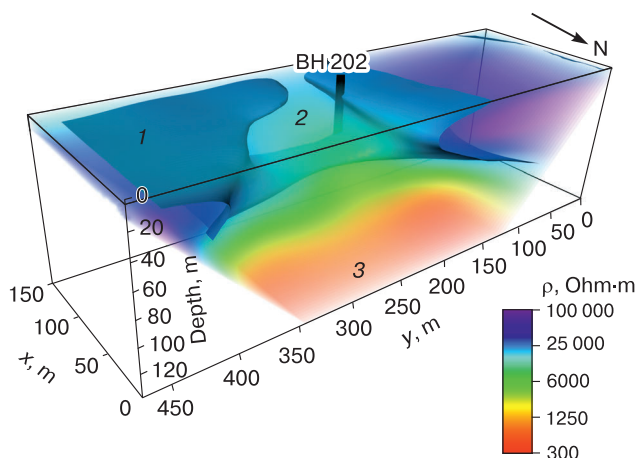


Fig. 12. Volumetric distribution of resistivity in Site II according to the results of three-dimensional inversion.

1 – electrical-resistivity isosurface of 20 kOhm-m, showing the distribution pattern of massive ice; 2 – area of low resistivity; 3 – low resistivity of the model associated with saline loams of marine origin. Number of iterations – 6; standard deviation – 8.3 %.

central part of the profile, within the range of 250–300 m, at the depth of 25–40 m, a general tendency for decrease in the resistivity of deposits with a locally anomalous resistivity (less than 1000 Ohm-m) has been observed. The geoelectrical section in Fig. 11 demonstrates that massive ice has a heterogeneous structure.

In order to give a complete idea about massive ice distribution between the Krugloye and Parisento lakes, a three-dimensional inversion of the ERT areal data has been carried out. The inversion has been performed both with fixation of layers with a known resistivity and a roof depth, and without any *a priori* information. After completing of 6 iterations, fixation of layers at a depth leads to an increase in the selection error from 8.3 % (without fixing of parameters) up to 10.4 % (with fixed parameters). So the structure of the upper part of the section up to a depth of 75 m does not change significantly. Figure 12 shows the result of three-dimensional inversion without fixed parameters of the model.

The isosurface of the resistivity, corresponding to 20 kOhm-m, displays the distribution of the high-resistive sediments including massive ice. It is easy to see that high-resistive layers have a discontinuous distribution pattern. An area of reduced resistivity is identified in the central part of the section, which means the absence of massive ice beds. Starting from a depth of 80 m, the resistivity of the model decreases down the section to the first thousand Ohm-m, which we attribute to the influence of saline loams of marine origin. Although resistivity of frozen loams in that

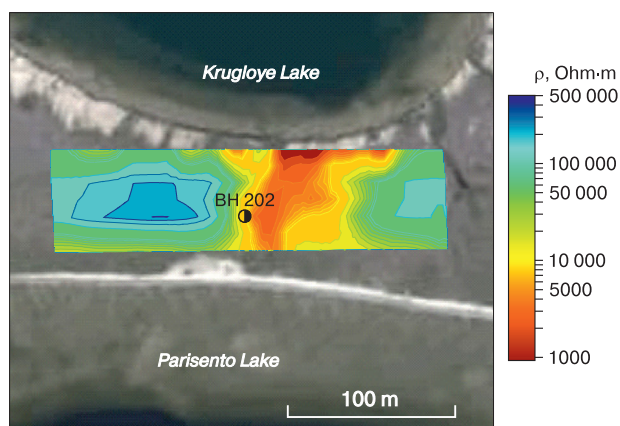


Fig. 13. Resistivity at depth of 30 m according to the results of three-dimensional inversion on a satellite image of the Site II.

model is 100 times higher than that of other sediments at the same depth, determined according to the TDEM data within the Site I, the general trend to the increasing of electrical conductivity of deposits at depths of more than 60–70 m has been noted in both methods. A scheme of the resistivity distribution at the depth of 30 m is displayed at a satellite image of the Site II (Fig. 13). The pattern of resistivity distribution demonstrates that there is no massive ice between the lakes, and borehole 202 having drilled in that ice, is located in the selvedge of the high resistivity anomaly. Spatially the low resistivity anomaly is associated with a linear lowered landform, disposed between the lakes. That may mean the existence of a paleochannel, i.e., it is possible that in the past the lakes were connected by a watercourse.

Cross-section of the three-dimensional model of resistivity along the boreholes line between Krugloye and Parisento lakes is shown in Fig. 14. As can be seen in Fig. 14, the part of the section containing massive ice stands out by the resistivity more than 100 kOhm-m. It should be noted that an icy clay layer within the depth interval of 20–30 m in no way stands out in the resistivity section. In a first approximation, the thickness of the high resistivity layer is consistent with thickness of the strata containing massive ice. However, the resistivity of the sediments underlying the ice bed is greatly overstated in comparison with the model obtained according to the TDEM sounding data in the Site I.

Thus, an analysis of the electrotomography data in the Site II has demonstrated that massive ice has a discontinuous distribution, as it was previously assumed according to the drilling results. A zone of low resistivity that does not contain massive ice has been revealed between the Krugloye and Parisento lakes. Obviously, that zone is associated with an old channel connecting the lakes in the past.

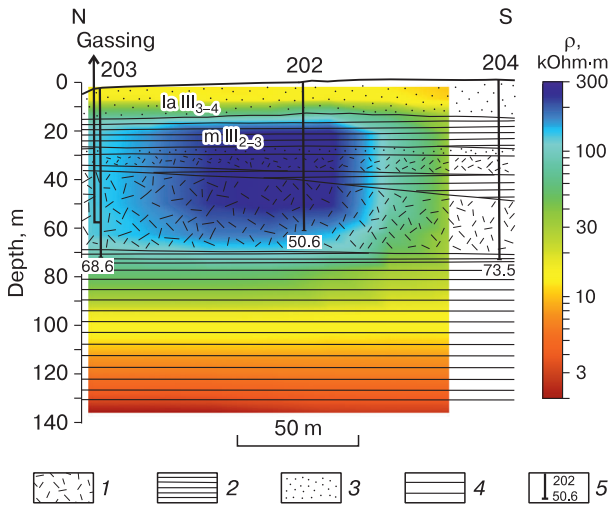


Fig. 14. Geoelectric section along the borehole line between the Krugloye and Parisento lakes according to three-dimensional inversion.

1 – ice; 2 – clay with inclusions of ice; 3 – frozen sand; 4 – loam; 5 – borehole, its number and depth (m).

MODELING OF THERMAL AND ELECTRICAL FIELDS

A decrease in the electrical resistivity of the sediments occurring near the lakes is traced in the resistivity distribution plan (Fig. 13), as well as that is observed in the section along the borehole line (Fig. 14). Such an effect can be caused by the warming of frozen sediments due to contact with water. To assess the warming effect of the water bodies, a two-dimensional model of the temperature distribution in the medium has been constructed according to the

thermometry logging data of the boreholes 202, 203, 204. Figure 15 displays that the warming effect of water bodies is clearly revealed, since the temperature in the boreholes located closer to the lake is higher (by 2–4 °C) than in a borehole located 100 meters from it. However, due to the limited number of boreholes, the temperature distribution model has turned out to be very approximate. An increase in the temperature of the frozen sediments, occurring near the lake, from –8 to –4 °C leads to a decrease in their resistivity. For instance, the resistivity of sands will decrease from 10⁵ to 10⁴ Ohm·m according to an approximate dependence from [Bogolyubov et al., 1984]. Figure 13 demonstrates that the resistivity of sediments near the lakes decreases by about an order of magnitude, which can be interpreted as the thermal effect on the electrical conductivity of the frozen stratum.

Since the temperature of the medium is an important factor determining the resistivity of frozen ground, it is necessary to represent the pattern of its distribution near the lakes. The Comsol Multiphysics v. 4.0 software package [Multiphysics..., 1998] has been used to calculate the temperature field model between the lakes and determine the configuration of the lake taliks. The program allows to set the geometry and properties of the medium model and the boundary conditions and, using the Heat Transfer module, to solve the heat transfer equation by means of the finite element method.

Based on the drilling data (Fig. 2), a horizontally layered model of the medium has been set: at depths of 0–12.5 m – a layer of sand, 13–26 m – a layer of clay, 27–37 m – a layer of sands with high ice content, 38–66 m – massive ice bed, 67–300 m – a layer of marine loam. There is a linear change in all physical properties into the intervals between the layers. Average values of thermal conductivity, specific heat ca-

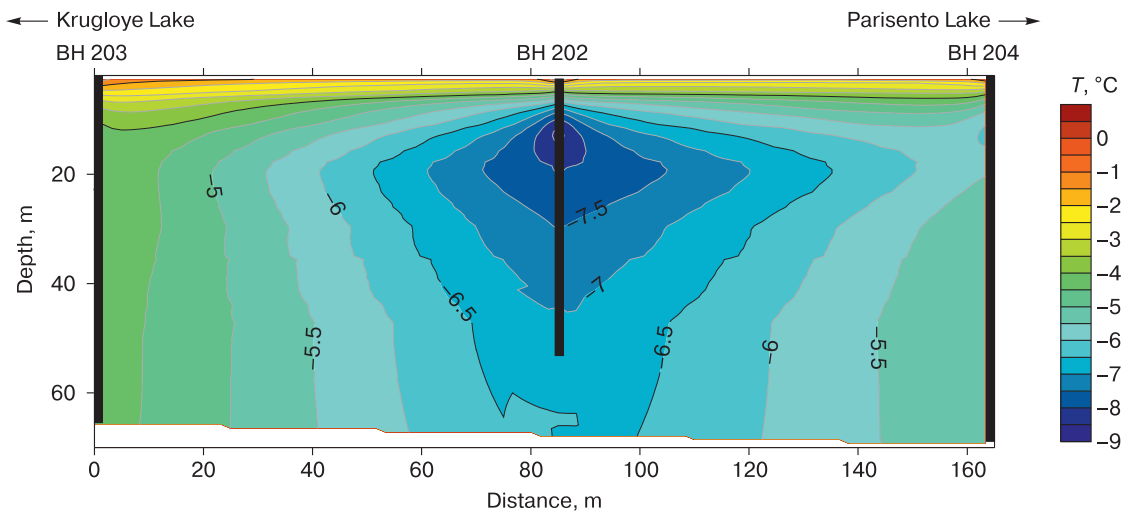


Fig. 15. Permafrost temperature in the section between the Krugloye and Parisento lakes according to thermometry at boreholes 202, 203, 204 in 1992–1993.

Table 1. The values of physical parameters of medium

Type of deposits	Thermal conductivity, W/(m·K)		Specific heat, J/(kg·K)		Density, kg/m ³		Freezing point, °C
	frozen state	thawed state	frozen state	thawed state	frozen state	thawed state	
Sand	1.80	1.65	1600	1200	1750	1750	-0.4
Clay	1.55	1.45	1200	1500	1500	1500	-0.6
Icy sediments (water-saturated)	2.0	1.10	1800	2900	1350	1400	-0.1
Ice (water)	2.25	0.65	2000	4212	917	1000	0
Loam (marine)	1.65	1.50	1225	1450	1500	1500	-1.8

capacity and density have been taken for each type of the sediments in two states: the frozen and thawed ones [Gavriliev et al., 2013; Aleksyutina, Motenko, 2017]. Those physical parameters are given in Table 1.

The shape of the lakes in the model has been assumed as cylindrical (i.e. with a flat bottom and vertical walls). That is justified by the fact that the radii of the lakes much exceed their depths. The radius and depth of the Parisenito and Krugloye lakes are 2500 m and 35 m, 300 m and 25 m, respectively (Fig. 16). The heat flux at the modeling site has been chosen equal to 0.05 W/m², since that value is consistent with numerous studies on the heat flux in that region [Kurchikov, 2001; Duchkov, Sokolova, 2014; Iskorkina et al., 2018].

The day surface temperature has been assumed to be -10 °C, which corresponds to the mean annual air temperature in that area. As the initial conditions throughout the medium, a temperature plot has been taken, corresponding to the equilibrium state under given boundary conditions (heat flux at the lower boundary and surface temperature at the top layer). The temperatures of +1, +2, +3 °C have been at the bottom of the lakes at the initial time, on the circles with a radius of 300, 200 and 50 m, and 2500, 1500, 500 m for the Krugloye and Parisenito lakes, respectively. That is justified by experimental data on tem-

peratures at the bottom of the lakes. After that, the medium has been presented as a finite element grid, and the heat transfer equation has been solved. The formation of thermokarst lakes on the Yamal Peninsula occurred in the first half of the Holocene Climatic Optimum [Slagoda et al., 2016]. Due to the lack of information about exact time of formation of Parisenito and Krugloye lakes, the time interval of 6000 years has been taken for the calculation. During that time interval, the heating of the under-the-lake medium has been simulated, while the phase transition has been taken into account.

The calculated temperature field of the section is displayed in Fig. 17. The layers lying deeper than 70 m are presented by marine saline loams, in which the mineralization of solutions increases by depth and can significantly exceed 1 g/L [Badu, 2015; Trofimov, Krasilova, 2017]. As a result, the authors suggest that the sediment transition from the frozen to cooled state occurs at a temperature of -1.8 °C [Roman, 2007]. That had been taken into account when determining the boundaries of the taliks.

Between the lakes, the isotherm of -1.8 °C runs at a depth of 220 m. Beyond the zone of influence of the lakes, the permafrost bottom lies at a depth of 240 m, which is consistent with the data of electromagnetic soundings, obtained by means the TDEM method. As can be seen out of the presented picture,

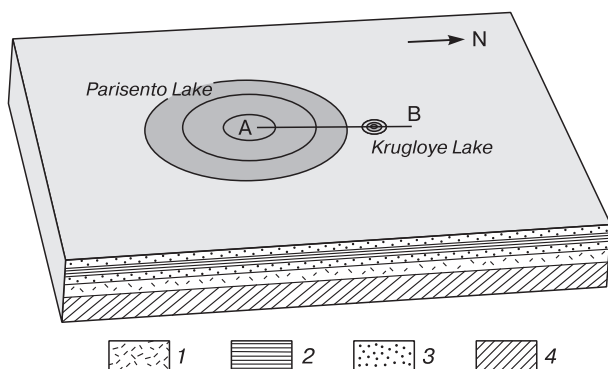


Fig. 16. The model scheme for calculating a thermal field.

1 – ice; 2 – clay with ice inclusions; 3 – frozen sand; 4 – marine loam; AB – line of cross-section.

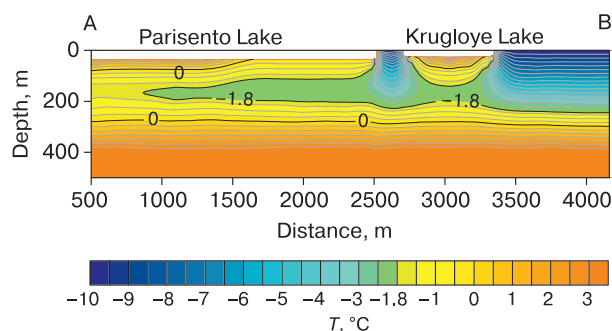


Fig. 17. Temperature distribution in a cross-section along the AB line (see Fig. 16) under the lakes according to numerical modeling results.

the taliks situated under the Krugloye and Parisento lakes are not connected. Calculations have shown that there is an open talik (presumably with a radius of 800 m) under Parisento Lake, closer to its central part. The calculated thickness of the talik situated under Krugloye Lake has been estimated as 140 m. In 1986, the VSEGINGEO employees carried out electrical-resistivity prospecting and seismic survey in the water area of Krugloye Lake. The electrical exploration methods included the vertical electric sounding of the lake bottom, using a three-electrode array, and the seismic prospecting was performed by the method of refracted waves. The research results have demonstrated that the thickness of the talik in the central part of the lake was about 140 m. Thus, the calculated value of the talik depth by the mathematical modeling of the thermal field does not contradict the results of geophysical studies of the past years [Pugach *et al.*, 1990].

Based on the obtained results, it can be concluded that the lakes significantly (by 4–6 °C) change the temperature in the inter-lake space at the depths of 20–40 m, which is consistent with the data of borehole thermometry. Thus, the influence of lakes can be one of the main factors in the reduction of resistivity in geoelectric sections. However, a conductive three-dimensional heterogeneity in the form of a water body, located away from the profile, can also produce a similar effect on the results of the ERT data inversion.

To simulate the effect of three-dimensional conductive heterogeneity on water bodies, a simple two-layer medium with a boundary at a depth of 70 m has been set. The model included two lakes and taliks below them (Fig. 18). The talik configuration has been taken by the temperature modeling results. The resistivity of 100 kOhm·m has been established for frozen sediments in the upper part of the medium, that of 30 Ohm·m has been assumed for a frozen loamy base. The resistivity of water in the lakes has been taken

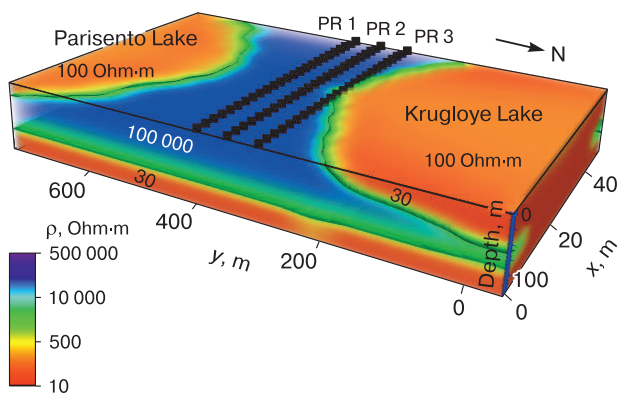


Fig. 18. Physical-geologic (geoelectric) model used in simulation of three-dimensional heterogeneity.

equal to 100 Ohm·m, that of thawed sediments has been assumed to be 30 Ohm·m. The order of the selected resistivity values are consistent with the data of geophysical surveys given above, as well as with the results of the application of vertical electric sounding in the water area of Krugloye Lake [Pugach *et al.*, 1990]. The ZondRes3d program has been used to solve the direct problem in the medium, defined as a three-dimensional one [Kaminsky, 2001–2010].

For three profiles located at different distances from the lakes (Fig. 18), the apparent resistance values has been calculated for an array similar to that used in field measurements. After that, for each profile, the inverse two-dimensional problem was solved in the Res2dInv program. As a result, geoelectric sections have been obtained along three profiles located at distances of 5, 50, and 100 m away from the lake (Fig. 19).

False anomalies of reduced resistivity are most distinct in the profile located near the lake (exactly, 5 m away from it). As they move away from the lake, the anomalies of the reduced resistivity become less pronounced.

To quantify the effect of three-dimensional heterogeneity on the distribution of resistivity in a two-dimensional model, the relative deviation of the section resistivity (in comparison with a simple two-layer model without lakes) has been calculated (Fig. 20) using the formula:

$$\Delta\rho = \frac{\rho_{3D} - \rho_s}{\rho_{3D}} \cdot 100\%,$$

where $\Delta\rho$ is the relative deviation of the resistivity of the three-dimensional model with lakes as compared to the simple model, ρ_{3D} is the resistivity calculated according to the model containing three-dimensional heterogeneity, ρ_s is the resistivity calculated in the simple three-dimensional model without heterogeneities.

Figure 20 demonstrates the profile located 5 m away from the lake that shows the most severe distortion in the resistivity over the entire section by up to 100 %. That is due to the fact that the electrical current flows through a nearby highly-conductive medium represented by a lake and a talik under it.

At 50 m away from the lake the relative deviation of the resistivity up to a depth of 25 m is close to 0 %. Below a depth of 25 m, when the size of the AB current line is commensurate with the distance to the lake, the resistivity distortion reaches 70 %. The highest values of that for the section (80 %) are revealed at depths of 75–90 m, which are associated with the overlapping influence of two water bodies. Relative deviations on the profile located 100 m away from the water body are the lowest. Understatement of resistivity relative to the reference two-layer model by up to 60 % is manifested in the depth interval of 50–100 m.

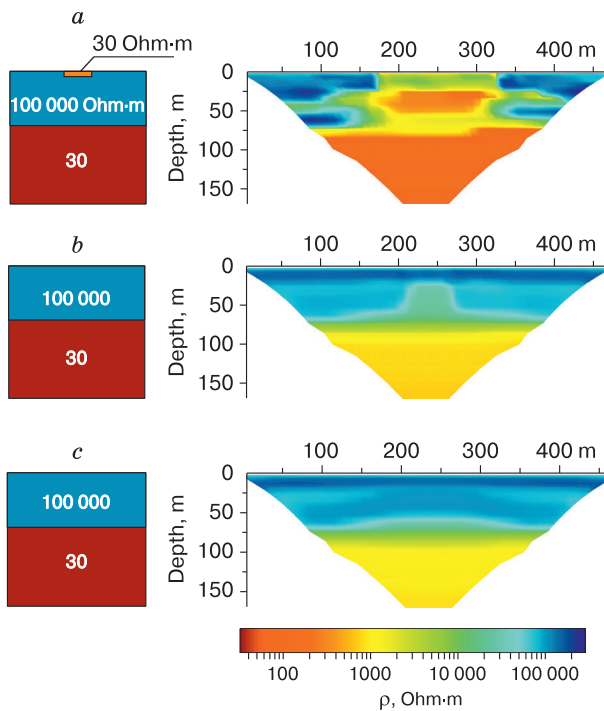


Fig. 19. Effect of three-dimensional heterogeneity caused by water bodies on the distribution of resistivity according to the results of two-dimensional inversion.

Distance of profiles from the lake: *a* – 5 m; *b* – 50 m; *c* – 100 m.

Thus, the results of numerical mathematical modeling have demonstrated that the presence of three-dimensional conductive heterogeneities in the form of lakes away from the sounding profile leads to an understatement of the model resistivity which begins to appear at depths equal to half the distance to the conductive heterogeneity. At 5 m away from the coast the relative decrease in the resistivity of the two-dimensional model reaches 100 %. At a distance from the coast the effect of conductive heterogeneity begins to appear at the pseudo-depth of the section, equal to half the distance to the lake.

Along with the influence of three-dimensional heterogeneity on the inversion results, a certain contribution to the final model of resistivity is made by the area of warmed permafrost near the lake. The only way to obtain a realistic geoelectric model that reflects the geocryological structure of a section near a water body is to locate sounding profiles across the coastline.

CONCLUSIONS

A horizontally layered structure of the medium has been established, according to the TDEM data. The upper part of the section up to the depths of 50–

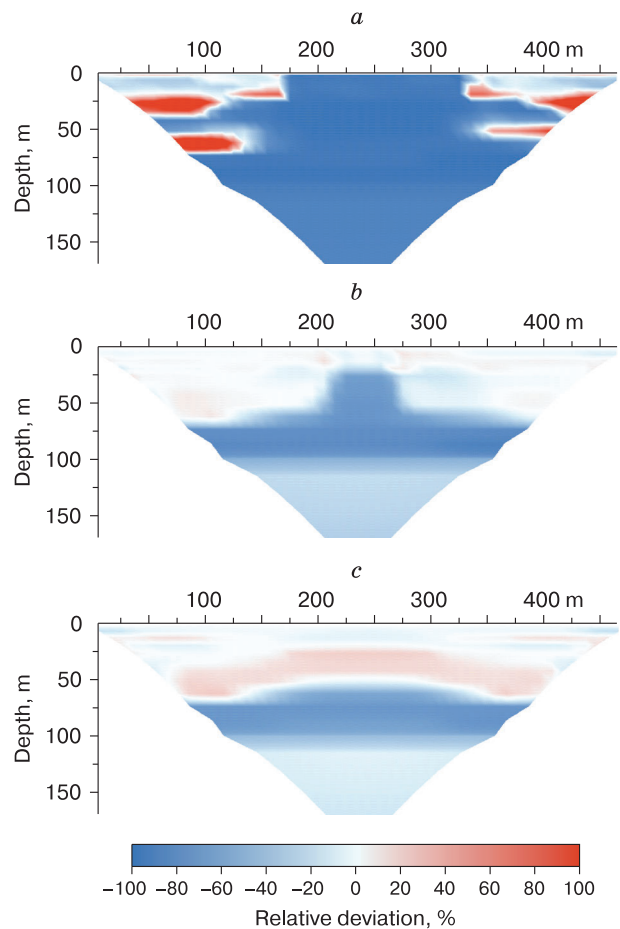


Fig. 20. Relative deviation of resistivity as compared with a simple model without heterogeneities.

Distance of profiles from the lake: *a* – 5 m; *b* – 50 m; *c* – 100 m.

75 m is represented by high-resistive frozen sediments with the inclusion of massive ice. The decrease in resistivity down the section is associated with marine saline loams. The thickness of permafrost is 210–300 m, according to the TDEM data.

According to the ERT data, the sediments of the upper part of the section up to the depths of 50–75 m have a very high resistivity, reaching hundreds of thousands Ohm-m and in some cases exceeding one million Ohm-m. High resistivity of the sediments is due to their lithologic composition (sands) and low salinity of the porous and massive ice. The highest resistivity values are characteristic of massive ice beds. Such a high electrical resistance prevents the penetration of electrical current into the depth as a result of which the sensitivity of the method is limited to the depth of 50–75 m. Under the layers having resistivity of more than 100 kOhm-m, the sensitivity of the method is limited by the depth of the roof of those layers.

When solving the inverse problem of electro-tomography, the introduction of deep layers with a known resistivity in the geoelectric model practically does not affect the selection error but makes the structure of the upper section more realistic, emphasizing the horizontally layered pattern of the high resistivity anomalies caused by massive ice.

According to the data of on-site studies by the ERT method, it has been found that the massive ice bed between the Krugloye and Parisento lakes is not of continuous distribution as it seemed earlier according to the drilling data. An anomaly of the low resistivity of deposits has been revealed, presumably related to the old channel connecting those lakes in the past.

Such geological heterogeneities as a lake and a lake talik cause anomalies of low resistivity in the electrical tomography sections. Moreover, the anomalies are associated both with the influence of a three-dimensional conductive heterogeneity located away from the profile, and with an increase in the temperature of permafrost near the lake.

Calculation of the thermal field has demonstrated that there is a closed talik under Krugloye Lake up to a depth of 140 m, and an open talik has formed under Parisento Lake. Those taliks, despite the relatively small distance between the lakes, are not connected. The permafrost temperature rises by 4–6 °C between the lakes, what also affects its electrical resistivity.

Modeling of the three-dimensional heterogeneity effect on the electric field has revealed that when solving the two-dimensional inverse problem for the profiles located near water bodies, a false anomaly of reduced resistivity (reaching 100 %) arises in geoelectric sections. Such high values are typical for the profiles located in the immediate vicinity of the lakes. The farther the profile is located from the lake, the less is that influence. Moreover, a decrease in resistivity begins to appear at the depth equal to half the distance to the lake. Thus, a decrease in the resistivity is associated both with an inhomogeneous temperature field and with the influence of three-dimensional heterogeneity, which is currently not possible to separate.

The authors thank V.A. Dubrovin for the provided geocryological information, as well as they thank the Information and Computing Center of Novosibirsk State University for the possibility of using computing resources.

That work has been supported by the FNI project No. 0331-2019-0007 “Geoelectrics in geological environment research: technologies, field experiment, and numerical models”.

References

Aleksyutina, D.M., Motenko, R.G., 2017. The composition, structure and properties of frozen and thawed rocks on the

Baydaratskaya Bay coast, Kara Sea. *Earth's Cryosphere XXI* (1), 11–22.

Anisimova, N.P., Kritsuk, L.N., 1983. Using of cryochemical data for studying of subsurface ice genesis. In: *Problems of Geocryology*. Nauka, Moscow, pp. 230–239 (in Russian).

Antonov, E.Y., Kozhevnikov, N.O., Korsakov, M.A., 2014. Software for inversion of TEM data affected by fast-decaying induced polarization. *Russian Geology and Geophysics* 55 (8), 1019–1027.

Badu, Yu.B., 2015. Ice content of cryogenic strata (permafrost interval) gas-bearing structures, Northern Yamal. *Earth's Cryosphere XIX* (3), 9–18.

Badu, Yu.B., Trofimov, V.T., 1974. Main trends of permafrost cryogenic structure in Yamal Peninsula. In: *Problems of Cryolithology*. Moscow University Press, Moscow, 24 pp. (in Russian).

Baulin, V.V., 1985. *Permafrost Soils of Petroleum-bearing Areas of USSR*. Nedra, Moscow, 176 pp. (in Russian).

Bogolyubov, A.N., Bogolyubova, N.P., Lisitsyn, V.V., Kurandin, N.P., 1984. Recommendations for geophysical exploration while engineering site investigations for construction (electrical survey). Stroyizdat, Moscow, 104 pp. (in Russian).

Duchkov, A.D., Sokolova, L.S., 2014. Heat flow in Siberia. In: *All-Russian Conference “Geophysical methods of investigation of the Earth crust”*. IPGG SB RAS, Novosibirsk, pp. 211–216.

Everest, J., Bradwell, T., 2003. Buried glacier ice in southern Iceland and its wider significance. *Geomorphology* 52 (3–4), 347–358.

Fague, A.N., Surodina, I.V., Yeltsov, I.N., 2016. Electrical resistivity tomography investigation of talik zones beneath thermokarst lakes (based on field measurements and 3D computer modeling). In: *Interexpo Geo-Siberia Conference*, vol. II (2), pp. 250–254 (in Russian).

Gavriliev, R.I., Zheleznyak, M.N., Zhizhin, V.I., et al., 2013. Thermophysical properties of the main rock types in the Elkon Mountain massif. *Kriosfera Zemli (Earth's Cryosphere)*, XVII (3), 76–82.

Hauck, C., Mühlh, D.V., 2003. Inversion and interpretation of two-dimensional geoelectrical measurements for detecting permafrost in mountainous regions. *Permafrost and Periglacial Processes XIV* (4), 305–318.

Hauck, C., Mühlh, D.V., Maurer, H., 2003. Using DC resistivity tomography to detect and characterize mountain permafrost. *Geophysical Prospecting LI* (4), 273–284.

Iskorkina, A.A., Prokhorova, P.N., Stotsky, V.V., et al., 2018. Reconstructions of geothermal mode of the petromaternal Kiterbutsk suite of the Arctic region in Western Siberia taking into account the influence of paleoclimate. In: *Proceedings of Tomsk Polytechnic University. Engineering of Georesources* 329 (2), 49–64.

Kaminsky, A.E., 2001–2010. Program for 3-dimensional data interpretation of resistivity method and induced polarization method (ground, borehole and off shore variants) ZondRes3D. 2001–2010, Zond Geophysical software, 75 pp. – URL: <http://zond-geo.ru> (last visited: 10.02.2018).

Kozhevnikov, N.O., Antonov, E.Y., Zakharkin, A.K., et al., 2014. TEM surveys for search of taliks in areas of strong fast-decaying IP effects. *Russian Geology and Geophysics* 55 (12), 1452–1460.

Kritsuk, L.N., Polyakov, V.A., 1989. Isotopic research of natural water and ice in West Siberia. *Engineering Geology*, No. 4, 76–94.

- Krylov, S.S., Bobrov, N.Y., 1995. Electromagnetic methods for exploration within permafrost. In: Geophysical Investigations of Cryolithozone / The Russian Academy of Sciences. Research Board of the Earth's Cryology. Moscow, No. 1, 208 pp. (in Russian).
- Kurchikov, A.R., 2001. The geothermal regime of hydrocarbon pools in West Siberia. *Geology and Geophysics* 42 (11–12), 1846–1853.
- Loke, M.H., 2009. Electrical imaging surveys for environmental and engineering studies. A practical guide to 2-D and 3-D surveys, RES2DINV Manual, 2009. – URL: <http://www.abem.se/fi/les/res/2dnotes.pdf> (last visited: 22.12.2015).
- McClymont, A.F., Hayashi, M., Bentley, L.R., et al., 2013. Geophysical imaging and thermal modeling of subsurface morphology and thaw evolution of discontinuous permafrost. *J. Geophys. Res.: Earth Surface* 118 (3), 1826–1837.
- Multiphysics, 1998. Introduction to COMSOL Multiphysics®. In: COMSOL Multiphysics, Burlington, MA, vol. 9, 2018 pp.
- Olenchenko, V.V., Kozhevnikov, N.O., Antonov, E.Yu., et al., 2011. Distribution of permafrost in Chuiskaya basin (Gorny Altai) according to transient electromagnetic soundings data. *Kriosfera Zemli (Earth's Cryosphere)*, XV (1), 15–22.
- Pugach, V.B., Skvortsov, A.G., Timofeev, V.M., Tsarev, A.M., 1990. Research of sub-lake taliks in the transpolar region of the West Siberia using geophysical methods. In: *Methods for Engineering Geocryological Survey: Collection of scientific papers / E.S. Melnikov (Ed.)*. VSEGINGEO, Moscow, pp. 139–143 (in Russian).
- Roman, L.T., 2007. The influence of salinity on the strength and deformability of permafrost soils. *Problems of construction on the salty permafrost soils*. Epoha, Moscow, 224 pp. (in Russian).
- Slagoda, E.A., Narushko, M.V., Preis, Y.I., et al., 2016. Reconstruction of thermokarst in the Late Pleistocene-Holocene from geocryological and botanical data (area of lake Sokhonto, Central Yamal). *Earth's Cryosphere* XX (4), 53–61.
- Trofimov, V.T., Badu, Yu.B., Vasilchuk, Yu.K., et al., 1986. Exogeodynamics of Western Siberian Plate (spatiotemporal trends). Moscow University Press, Moscow, 245 pp. (in Russian).
- Trofimov, V.T., Baulin, V.V. (Eds.), 1984. Map of the thickness and structure of permafrost in West Siberian plate. *GlavTyu-mengeologiya; MGU; PNIIS*, Moscow, 1 sh.
- Trofimov, V.T., Krasilova, N.S., 2017. Patterns of changes in the degree and spatial distribution of the soil salinity in the permafrost soil strata of the Arctic coast of Russia. In: *Engineering-Geological Problems of Modernity and Methods for Their Solution*. Geomarketing, Moscow, pp. 8–16 (in Russian).
- You, Y., Yu, Q., Pan, X., et al., 2013. Application of electrical resistivity tomography in investigating depth of permafrost base and permafrost structure in Tibetan Plateau. *Cold Regions Science and Technology* 87, 19–26.
- Zykov, Y.D., 2007. *Geophysical Methods for Investigation of Cryolithozone*. Moscow University Press, Moscow, 272 pp. (in Russian).

Received November 8, 2018

Revised version received November 19, 2019

Accepted November 29, 2019

CHRONICLE

DOI: 10.21782/EC2541-9994-2020-2(60-61)

LUDMILA SEMENOVNA GARAGULYA**(10.12.1934–30.06.2019)****E.N. Ospennikov, G.I. Gordeeva***Lomonosov Moscow State University, Faculty of Geology,
1, Leninskie Gory, Moscow, 119991, Russia; geocry@geol.msu.ru*

On June 30, 2019, at the age of 84, after a long grave illness, Ludmila Semenovna Garagulya died. She was a prominent scientist, professor of the geocryology chair of the geology department of the Moscow State University, doctor of geological and mineralogical sciences, laureate of the State Prize of the Russian Federation in Science and Technology, and Honored Scientist of RF.

Geocryology, geocryological processes, educatory activities



On June 30, 2019, at the age of 84, after a long grave illness, Ludmila Semenovna Garagulya passed away. She was a prominent scientist, professor of the geocryology chair of the geology department of the Moscow State University, doctor of geological and mineralogical sciences, laureate of the State Prize of the Russian Federation in Science and Technology (1993), and holder of the title of the Honored Scientist of RF (1995).

Ludmila Garagulya was born on December 10, 1934 in Zaporozhe. In 1953, after finishing secondary school with a gold medal, she entered the geology department of the Moscow State University, from which she graduated in 1957 with qualifications of a geologist-hydrologist. After graduation from the MSU, in 1957–1958 she worked as a senior laboratory technician of the Geography Institute of the Academy of Sciences of the USSR in Polar Urals. Further on, the scientific and educatory work of Ludmila Garagulya (except for the period of 1972–1977,

when she worked as the head of a sector in the All-Union Research Institute for Construction of Trunk Pipelines), was connected with the geocryology chair of the geology department of the Moscow State University. Here she passed a long road from the head of a geological field party to the senior researcher in the chair expeditions which worked in the northern and north-eastern regions of the country. In 1965, Ludmila Garagulya defended a candidate's thesis, in 1977 she became an associate professor, and, after defense of the doctorate in 1984, she headed the laboratory of mathematical methods and geocryological prediction (1984–2000). In 2000, Ludmila Semenovna became a professor of the geocryology chair.

Ludmila Garagulya was known for the broadness of her scientific interests, including geocryological survey, forecasting the behavior of geocryological processes, evaluative mapping of the permafrost zone, geological processes in the permafrost zone, and issues of environmental geocryology. To solve the tasks of

geocryological survey and mapping, she developed a geocryological engineering classification of Quaternary permafrost formations, reflecting the genetic connection between permafrost and engineering geological characteristics and the geomorphological structure of a territory, the origin and composition of the sediments and the specific features of their cryogenic transformations. She developed a classification of the geological permafrost processes based on the energetic and geological conditions of their development, which determine their specific manifestation on the terrain. Based on this classification, Garagulya developed an approach to evaluative mapping of the geological permafrost processes. To predict resistance of frozen soils to anthropogenic impact and load, she developed a special classification of disperse rocks underlying plains. Ludmila Garagulya had more than 150 works published, including 7 monographs, 8 textbooks and manuals. During dozens of years, Ludmila Garagulya led the geocryological research carried out in Central, Western and Eastern Siberia, in the north-east of Russia, in Pribaikalye and Amur region.

Beginning with 1977, Ludmila Garagulya worked as an educator, too. She developed and delivered such courses as the methodology of geocryological research, geocryological survey and mapping, dynamic geocryology, geocryology, environmental aspects of geocryology, geocryological hazards in Russia, and geocryological monitoring. She was the supervisor for 11 candidate's theses, which were successfully defended.

Apart from extensive research and educatory activities, Ludmila Garagulya carried out a large volume of organizational work in science, performing at different times the duties of a learned secretary of the specialized dissertation council in the Moscow State University and of a member of the editorial board of the *Geoecology* journal.

Colleagues, friends and students appreciated Ludmila Semenovna's high professionalism, honesty and integrity, reliability, responsibility, and devotion to science.

Ludmila Semenovna Garagulya will be always remembered as an outstanding researcher, a talented teacher, a faithful friend and a helpful colleague.

Received November 21, 2019